UNIVERSITY OF CALIFORNIA SAN DIEGO

Numerical Study of Shock Focusing Phenomena Using Geometrical Shock Dynamics

A dissertation submitted in partial satisfaction of the
requirements for the degree
Doctor of Philosophy

in

Structural Engineering

by

Heng Liu

Committee in charge:

Professor Veronica Eliasson, Chair
Professor Jiun-Shyan Chen
Professor Hyonny Kim
Professor David Saintillan
Professor Chia-Ming Uang

2021

The dissertation of Heng Liu is approved, and it is acceptable in quality and form for publication on microfilm and electronically.

University of California San Diego

2021

TABLE OF CONTENTS

LIST OF FIGURES

ACKNOWLEDGEMENTS

At such a milestone in my life, there are may people I want to say a big thank you. First I would like to express my sincere gratitude to my Ph.D. advior, Professor Veronica Eliasson. I first met her back in 2014 when she was instructing my Compressible Gas Dynamics class. I was soon inspired by her intellectual research ideas and passion for teaching, so worked really hard to get the opportunity to work in her Shock Wave Lab in the same summer. Since then she led by example guiding me to become a professional researcher and helped me overcome obstacles one another. I am always appreciating her consideration and support throughout my master and Ph.D career, especially during the pandemic. Without her continuous encouragement, I could not make any achievement under heavy mental and intellectual load at the time. I feel truly fortunate to have her as my academic mentor as well as a friend.

I also really appreciate to have the privilege to work with knowledgeable professors, brilliant colleagues and supportive friends at UCSD. First, I would like to thank all my Ph.D. committee members, including Professor Jiun-Shyan Chen, Professor Hyonny Kim, Professor David Saintillan, and Professor Chia-Ming Uang. Their constructive suggestions and extensive experiences had helped me improve my research work.I would also like to thank Professor Oliver Schmidt, who administered my comprehensive exam and shared with me his inspiring perspectives in particle methods. Furthermore, I am grateful to have Rodrigo Chavez Morales and Benjamin Joseph Katko as my lab colleagues and friends. Rodrigo has always been willing to answer my questions and helped me know better about shock experiments. Daily conversations with Ben highlight my days on and off work, full of fun, sincerity and vivid exchange of ideas. Working in the same office and playing soccer together linked Xiaolong He to me. He is one of the smartest people I have ever met but has been patiently listening to me everytime I tried to explain my work then provided useful feedbacks. Special thanks to Shi Qiu, who assisted me in setting up my first Ph.D.

project even after he left the lab starting his job. Also, credits go to all other my friends and staff at the UCSD structural engineering department for all your support during four years.

I owe my foremost appreciation to my parents back in China for their unconditional love. Their diligent work ethics and courage for life have laid foundations for me to become who I am today and will continue. Not being able to accompany them when needed constantly reminds myself of the meaning of this journey and my given name always empowers me in the face of setbacks. Last but not least, thank you to my amazing wife. You have been with me going through ups and downs in all these years but never stopped supporting me even one day.

Chapter 2, in part is currently being prepared for submission for publication of the material. Heng, Liu; Veronica, Eliasson. The dissertation author was the primary investigator and author of this material.

The work presented in Chapters 2 and 3 was done thanks to the support of the Air Force Research Laboratory under award number FA8651-17-1-0004, the Office of Naval Research under grant number CBET-1803592, and Colorado School of Mines.

VITA

2010	B.S. in Thermal Energy and Power Engineering, South China University of Technology, China
2015	M.S. in Mechanical Engineering, University of Southern California, Los Angeles, CA.
2021	Ph.D. in Structural Engineering, University of California San Diego, San Diego, CA.

PUBLICATIONS

J. Dela Cueva, L. Zheng, B. Lawlor, K. Nguyen, A. Westra, J. Nunez, J. Zanteson, C. McGuire, R. Chavez Morales, B. Katko, H. Liu and V. Eliasson, "Blast wave interaction with structures – an application of exploding wire experiments," *Multiscale and Multidisciplinary Modelling*, Experiments and Design, 2020, DOI 10.1007/s41939-020-00076-0.

ABSTRACT OF THE DISSERTATION

Numerical Study of Shock Focusing Phenomena Using Geometrical Shock Dynamics

by

Heng Liu

Doctor of Philosophy in Structural Engineering

University of California San Diego, 2021

Professor Veronica Eliasson, Chair

Shock wave focusing can lead to extreme thermodynamic conditions, and applications have been extended to a variety of areas such as civil engineering and medical treatment. Among all numerical approaches, geometrical shock dynamics (GSD) is a model capable of efficiently predicting the position, shape and strength of a shock. Compared to the traditional Euler method that solves the inviscid Euler equations, GSD is a reduced-order model derived from the method of characteristics that is more computationally efficient since it only considers the motion of the shock front instead of the entire flow field.

Whitham's original theory of GSD successfully relates the change of area upon the

shock front to the shock motion with an assumption of a uniform state behind the shock, so it is able to accurately predict the behavior of a shock wave with constant properties behind it. However, the truncation of the post-shock flow term discredits its application to shock waves with decaying properties behind (e.g., in the case of blast waves). In this study three two-dimensional GSD models were first reviewed with a focus on how the post-shock flow effect is accounted for. It turned out that the completeness of the post-shock flow term determines the accuracy of GSD for blast waves, but prior knowledge of the particular blast is required to achieve full completeness. The point-source GSD (PGSD) model thus stands out since it encodes the analytical solution to blast propagation and is independent of the initial energy content of the point-explosion. Then a general framework based on PGSD was proposed aiming at efficiently solving the irregular reflection phase of blast focusing problems. Lagrangian simulations were thus performed for the symmetric interaction between two cylindrical blasts and compared to the experimental results. An agreement in attenuation of the maximum pressure at the Mach stem was observed but an overestimation of the Mach stem growth at its early stage by PGSD was also seen. To address this issue, an alternative model called PGSDSS was developed that combines PGSD and the shock-shock approximate theory for cylindrical shock reflection off a straight surface.

Another advantage of PGSD is its capability to be extended to three dimensions. Unlike the traditional three-dimensional GSD studies using triangulated meshes, in this study the shock surface is represented by a point cloud arranged in an octree data structure, such that a fast k-nearest neighbor search is possible without the need of connectivity information. Differential geometric properties required by PGSD are obtained by computing the moving least squares (MLS) surface that approximates the underlying shock surface. The resulting MLS-PGSD model was utilized to investigate first the propagation of a single spherical micro-blast in air and then its reflection off a solid wall. A good agreement of the

blast front contour at different time instants with the experimental results was reached.

Chapter 1

Introduction

1.1 Motivation

A shock wave is always closely related to high energy density since it is most often generated by a sudden release of energy in a confined space. Analogously, if existing shocks are propagating in a confined volume concentration of energy is supposed to be achieved, that is manifested by extreme conditions created at the focal region including very high pressure and temperature. Shock wave focusing takes place when a shock propagates through non-uniform or moving media, reflects from solid or porous surfaces, or multiple shocks interact with each other [6].

In nature, bubble cavitation is one common source that leads to shock focusing during its collapse phase. When collapse eventually happens as the result of increased pressure surrounding a bubble and its own surface tension, a significant amount of energy contained inside is released in the form of shock wave accompanied by jet and visible light emission (i.e., luminescence). Then what follows is the interaction between shocks emitted by collapsing bubbles. Cavitation bubbles can be generated in different situations. For example, in ocean fast swimmers like dolphins can generate cavitation bubbles around the

trailing edge of their rear fin due to the movement of fins [6, 7]. Once collapse, the resulting jets and shock waves may hurt the dolphin and limit its speed. Cavitation can also be observed in plants. Within xylem, which is a tissue in vascular plants that transports water and nutrients from roots to stems and leaves, cavitation of water columns would result in embolism thus reduce hydraulic conductivity [8].

On the other hand, shock wave focusing events happening in human society often result in undesired effects, though most of them are non-intentional. One example is a sonic boom that disrupts people and cause minor damage to structures. Weak shocks are generated continuously from an aircraft body traveling through air at a speed faster than sound. As shocks coalesce, the accumulative effects make the sonic boom intense enough to be detrimental at large distances. Another unfavored occurrence of shock focusing is that in an underground coal mine structure. When an accidental explosion occurs underground, shock waves are forced to propagate in the channels and may focus. If no mitigation methods are implemented to effectively reduce the energy of the explosion, people's lives and infrastructure are in great risk [9].

However, one application of shock wave focusing in medicine is beneficial to patients as a noninvasive treatment to eliminate kidney stones. In extracorporeal shock wave lithotripsy (ESWL), weak shocks are generated in the lithotripter and focus in the patient's body where the kidney stone exists. At the focal region pressure is increased to a level that leads to the fragmentation of the stone, while outside the focal region weak shocks pass through with minimal damage to the surrounding tissues.

To summarize, the extreme conditions created at the focal region stemming from shock focusing can be either detrimental or beneficial, but an accurate prediction of shock focusing events is rarely a trivial task due to the nonlinear nature of shock waves and complicated physics associated with their interactions. Therefore, to better take advantage of benefits from shock focusing and attenuate its damage to environment and human lives,

understanding the basic physical mechanisms governing focusing behaviors is important.

1.2 Literature Review

Before proceeding to literature review on shock focusing, flow properties behind a shock front should be first discussed. In fact, there exist many approaches to generate shock waves but almost all require a sudden release of energy in a confined volume with its expansion exceeding the ambient speed of sound [10]. One practical method to generate shocks is to use a shock tube with constant cross section area, in which a sudden release of pressurized gas towards the low-pressure section produces compression waves that later coalesce into a shock wave. Figure 1.1 presents the time history of pressure experienced at a fixed location for the shock generated this way (often referred to as a "shock wave with constant properties behind"). Ambient pressure P_0 is recorded first at the point of measurement until the arrival time of the shock front, t_0. Abruptly, the pressure rises to its peak value P_s^+ in a step function manner, then stays constant for an extended period of time. Detonation of high explosive materials is another common source to be considered. However, in this situation, as a shock wave propagates outwards away from the center of explosion, pressure, density and particle velocity internal to the shock front are decaying with time. Such observation is also illustrated in the pressure-time profile in Figure 1.1 where a discontinues increase of pressure is followed by a gradual decline. The duration over which the pressure remains above P_0 is defined as the positive phase and labeled as Δt_+. The pressure continues to drop reaching its lowest value P_s^- and then recovers to the ambient level by either a gradual increase or a secondary shock at a later time. Analogous to Δt_+, Δt_- is used to refer to the negative phase. If the flow properties following a shock front decay exponentially, this type of wave is specifically defined as a blast wave.

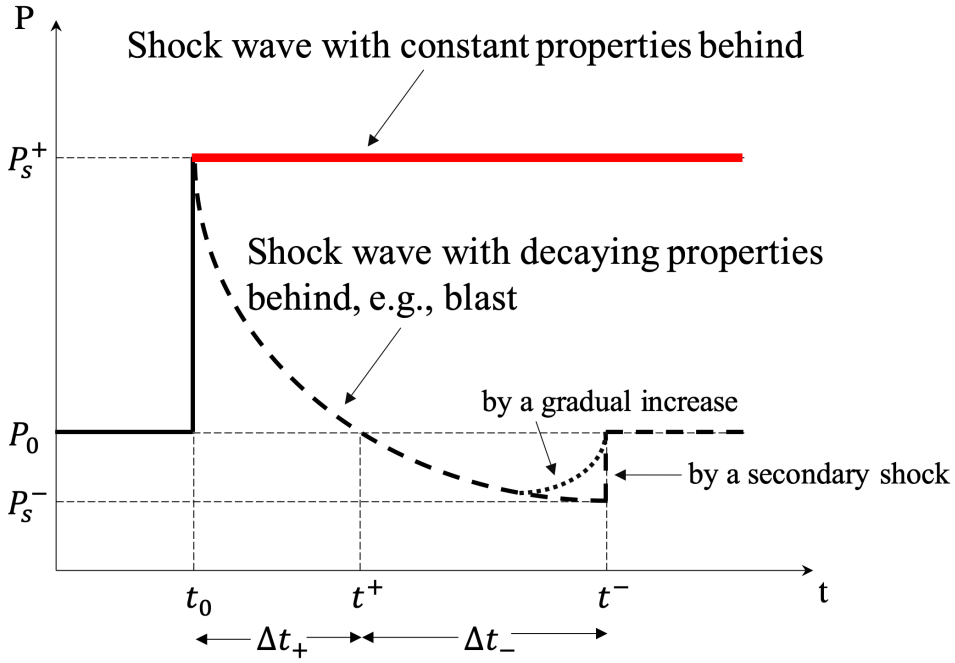

Figure 1.1: Typical time history of pressure at a fixed point experiencing a shock wave. Red solid line: shock wave with constant properties behind; Black dotted line: shock wave with decaying properties behind.

1.2.1 Shock Wave Focusing

The very first analytical work on cylindrical and spherical shock focusing can be traced back to the early 1940's. The motion of converging shock waves in a perfect gas at rest was studied by Guderley in 1941 [11], who demonstrated the existence of similarity solutions in the vicinity of the convergence center by reducing the problem into a nonlinear first-order ordinary differential equation. Stanyukovich [12] first developed an approximate method to determine the constant similarity exponent α of the shock front trajectory formula $R \sim (-t)^{\alpha}$, where R being the distance from the shock front to the focal point and t the time to reach the position, based on the analysis of the singular points of the differential equation. Mishkin and Fujimoto [13] argued that there should exist a single maximum pressure in the flow behind the shock front for all values of specific heat ratio γ.

This concept led to the determination of α in a closed form. However, their argument was challenged by Lazarus [14] as he showed a critical value γ_c beyond which the maximum in pressure is not resolved [15]. Such comment was later supported by Yousaf [16] who proved the equivalence of methods outlined by Stanyukovich [12] and Mishkin and Fujimoto [13]. Since Stanyukovich's result is an approximation to α, Mishkin's and Fujimoto's claim of exact expression for the similarity exponent was a false one. The self-similar solutions were then extended for non-ideal gas satisfying the equation of state of the Mie-Gruneisen type by Ramu [17], and for relaxing gas by Sharma [18]. Several experiments were performed to determine the similarity exponent, among which the first one was made by Perry and Kantrowitz [19], who pioneered the techniques to obtain cylindrically converging shocks in a shock tube. Baronets [20] found the exponent to vary with shock velocity through his experiments of imploding cylindrical shocks in argon and xenon created by means of pulsed induction discharges. Takayama *et al.* [21] measured the similarity exponent by performing least squares fits to streak camera recordings of converging cylindrical shock trajectories in air ($\gamma = 1.4$). The exponent for three different values of specific heat ratios (γ =1.13, 1.40 and 1.55) were determined experimentally by Kjellander *et al.* [22] with various initial Mach numbers.

Approximate solutions were developed since the 1970's that deal with complex situations arising from the interaction between multiple cylindrical or spherical shock waves. Among those, the Low Altitude Multiple Burst (LAMB) rules [23] were extensively used to approximate combined density, velocity and peak overpressure at a point in space due to coalesced waves. It is worth pointing out that the procedure of pressure addition is a nonlinear one that preserves the vector nature of the velocity and momentum [10]. The LAMB rules can be seen as loose conservation laws of mass, momentum and energy, so their accuracy depends on the selected models used to describe a single blast wave propagation in the free-field. The concept of image bursts [10] further simplifies the application of the

LAMB rules to symmetric interaction of shock waves by replacing imaginary sources with an ideal planar reflecting surface. Despite Brode's doubt about the assumptions of the rules [24], the nonlinear addition rules-based LAMB model was numerically implemented for various shock interaction applications. Yeghiayan *et al.* [25] used the LAMB codes to analyze gust, overpressure and thermal damage on an aircraft as the result of the enhancement of effects due to multiple bursts. Craver *et al.* [26] summarized the influence of shock wave produced by one burst on the flow field of another in terms of the fire ball development predicted by the LAMB codes. A number of LAMB calculations were carried out by Abeyta *et al.* [27] to take advantage of the model's efficiency. Overpressure and overpressure impulse-time histories at several fixed locations were reported to help determine physically plausible attack scenarios. Keefer and Reisler [28] placed multiple charges in equilateral triangular patterns to study simultaneous and non-simultaneous detonations. Their experiments showed that the maximum overpressure can be achieved by simultaneous detonations but required optimization of charge placement, and such observation was verified by the LAMB model. Moreover, the overpressure resulted from multiple charge detonation was found to cause damage at greater distance than if the same explosive weight had been denoted as a single charge. A similar topic regarding the influence of initial configuration of shocks that coalesce into a cylindrical one later was discussed by Yee and Abe [29]. Based on the simulation results, they delivered a report that clarifies the fact that initially non-circular shock wave yields higher pressure near the central point than initially circular shock wave.

With the advancement of computer hardware and algorithms specifically tailored for computational fluid dynamics, numerically solving the Euler or Navier-Stokes equations became an available option for shock focusing problems. Book and Löhner [30] performed finite element simulations to investigate cylindrically converging shock and observed the quatrefoil appearance of the shock front at a sufficiently low Mach number. Implosion

of two-dimensional polygonal shock fronts were studied by Aki and Higashino [31] with a finite difference scheme. Reconfiguration events during the process were observed that revealed the complexity of physics existing in the flow field ahead of the shock front. Non-circular shock wave focusing was also explored by Betelu and Aronson [32] who successfully described the intermediate asymptotic stage seen in the numerical simulations with the self-similar solutions. Balasubramanian and Eliasson [33] disturbed a cylindrically converging shock by placing cylindrical obstacles radially in its path in a series of Euler simulations. After analyzing the pressure and temperature recorded at the focal point for various configurations of obstacle size and number, they theorized that there should exist an optimal configuration that leads to the most extreme conditions at the center. Interaction of multiple simultaneous and non-simultaneous blast waves was numerically studied by Qiu and Eliasson [34]. The Euler equations were solved with point-source blasts initially defined by Taylor's similarity law [35], and a trend was found similar to that of Keefer and Reisler's [28]. Results showed that multiple munitions can be beneficial for creating peak overpressure at the focal point when compared to a single munition.

As an appealing alternative to a full Euler simulation, geometrical treatment of shock propagation has been developed since the 1950's. Chisnell [36] considered the convergence of a shock wave in a channel with varying cross section area and came up with a closed-form approximate solution for the change in shock strength as a function of channel area. The same expression was also independently derived by Chester [37] and Whitham [38, 39, 40], respectively. As illustrated in Figure 1.2, the so-called geometrical shock dynamics (GSD) discretizes a shock front into numerous small particles, then rays are introduced as orthogonal trajectories of the successive positions of these particles on the shock front. Each shock particle propagating along its own ray is treated as a problem of shock propagation in a non-uniform tube with solid walls, and the area-Mach number relation bridges the velocity of the particle to its ray tube area. Because of

its computational efficiency, GSD has been widely numerically implemented by scholars to study shock focusing behaviors especially when running time is the primary concern [41, 42, 43, 3].

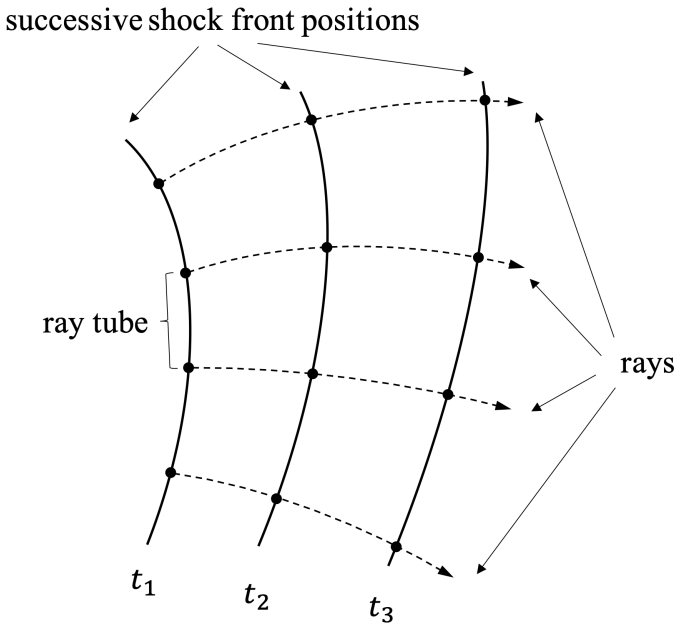

Figure 1.2: Schematic illustration of successive shock front positions at three different time instants and rays in geometrical shock dynamics.

As mentioned above, Perry and Kantrowitz's experiment [19] sparked the discussion about the stability of converging shocks as they argued that a converging wave is considered to be stable if it approaches perfect cylindrical or spherical shape without the interference of random disturbances as it propagates. They succeeded in converging a moderately strong shock wave with an initial Mach number of 1.7 in an axially symmetric shock tube, and presented schlieren photographs showing various phases of the formation as well as the stability of these converging waves. Knystautas *et al.* [44] achieved a stable convergence by patching up a number of planar detonation waves. They claimed that a polygonal shaped front was first generated then transitioned to a smooth cylindrical front through Mach reflections on collisions, but the quality loss of photographs makes it difficult to

confirm. Roig and Glass [45] designed a hemispherical chamber to experimentally study imploding spherical shocks. A blast wave was created by exploding the reactive gas at the origin of the hemisphere, then it became a converging shock when reflecting back from the inside of the chamber surface. The time-resolved pressure histories were found to be lower than the theoretical predictions. The same experimental setup was used by Saito and Glass [46] but temperature was measured spectroscopically at a much smaller observation area. As the result of the more precise measurement, their temperature results agreed better with the expected values. The stability of converging cylindrical shocks was also investigated experimentally using an annular shock tube by Wu *et al.* [47]. The breakdown of shock front curvature by artificial perturbations demonstrated the inherent unstable nature of converging shocks. Similar discussions from the viewpoint of the effects of initial disturbances' growth on the final shock wave convergence were also made by Takayama *et al.* [21], Watanabe *et al.* [48, 49], Matsuo *et al.* [50], Neemeh and Ahmad [51] and Eliasson *et al.* [52, 53]. Hosseini and Takayama [54] investigated the convergence and acceleration of spherical shock waves. Influence of the flow field ahead and the product gases on the converging shock waves were discussed.

Shock focusing due to the interaction between two identical weak blasts were studied by Higashino *et al.* [2]. By simultaneously exploding a pair of thin wires made of either copper or nichrome with a certain amount of initial energy, a symmetric interaction was achieved. The resulting schlieren photographs recorded the transitions from regular to irregular reflection, and pressure gauges registered time histories of the maximum pressure at the shock front. A similar experiment was conducted by Jiang *et al.* [4] who observed the reflection of a micro-blast generated by pulsed-laser beam focusing off a solid wall. This is equivalent to the shock interacting with another one of the same strength and size initialized on the opposite side of the wall according to the concept of image bursts [10]. Shock focusing was also examined as a technique to attenuate undesired propagation of

shock waves. In a laboratory environment an array of obstacles placed along a logarithmic spiral geometry showed its potential to confine the energy of a plane incident shock in a relatively small area in an air-filled shock tube test section (Ivanov *et al.* [55]) as well as in a water-filled test section (Wang *et al.* [56, 57, 58]).

1.2.2 Transition from Regular Reflection to Irregular Reflection

As extreme conditions at the focal region are mostly created through shock reflections, it is worth to note important contributions to the analysis of shock wave reflection. Since Ernst Mach [59] reported his discovery on shock reflection back in 1878 research has been conducted on this subject. Of particular interest is the determination of transition criteria from regular reflection (RR) to irregular reflection (IR) in various flow conditions. A regular reflection is defined as a shock pattern consisting of two shocks, namely the incident shock and the reflected shock, meeting at the reflection point. This type of shock reflection is supposed to be observed when an incident shock reflects off a surface with a proper angle in supersonic flow as illustrated in Figure 1.3(a), or a moving shock collides on an oblique surface inclined at a large angle as in Figure 1.3(c). Different than RR, an IR pattern features at least three shocks. The most often seen, but not the easiest configuration is a (single) Mach reflection (MR) as the cases shown in Figure 1.3(b) and (d) for steady flow reflection and pseudy-steady flow reflection, respectively. Besides the incident shock and the reflected shock, a third shock wave, the Mach stem, exists in an MR configuration. The three discontinuities meet at the triple point, from which a streamline originates separating flows deflected by the reflected shock and Mach stem. Flows on both sides of the streamline share the same pressure but may have different magnitudes of velocity in a direction parallel to the streamline.

The criteria for the transition from RR to IR in steady and pseudo-steady flows have been well established to date. The reflection domains are usually plotted in a complementary

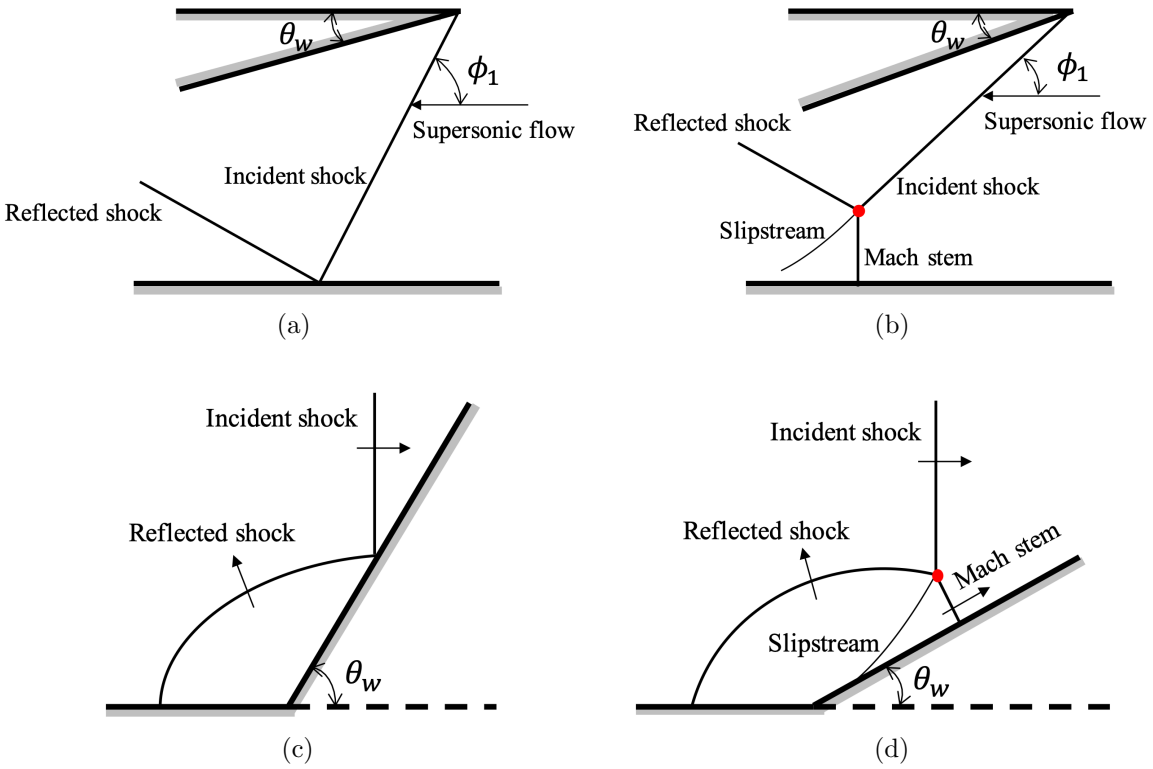

Figure 1.3: Schematic illustration of two basic shock wave reflection configurations: (a) Regular reflection in steady flows; (b) Irregular reflection in steady flows; (c) Regular reflection in pseudo-steady flows; (d) Irregular reflection in pseudo-steady flows. Triple point represented by a red dot.

wedge angle versus incident Mach number plane, i.e., the $\theta_w^c - M_s$ plane as presented in Figure 1.4. Basically there are four well known transition criteria that determine if an RR or IR should take place under certain circumstances. The **detachment criterion** proposed by von Neumann [60] defines a set of conditions beyond which the flow cannot be deflected anymore by the reflected shock, hence a two-shock configuration can no longer persist. The transition line in the $\theta_w^c - M_s$ plane from the detachment criterion that separates the RR and IR domains can be computed using the two-shock theory [61]. Initiated by von Neumann and then reintroduced by Hornung *et al.* [62], the **sonic criterion** states that the transition is only possible when the wedge corner generated signal can catch up with the reflection point in an RR configuration. This requires the flow immediately behind the

reflected shock to be at least sonic such that the signal that propagates at the local speed of sound can communicate the reflection point. Lock and Dewey [63] carried out an ingenious experiment that qualitatively proved the soundness of the sonic criterion. They succeeded in showing the sonic point measured by apparatus (the catch-up point) to agree well with the transition angle detected by visual inspection for planar shock over a straight surface. It is worth noting that in the $\theta_w^c - M_s$ plane the transition line from the sonic criterion obtained from solving the two-shock theory is very close to that from the detachment criterion so it is not shown in Figure 1.4. Later, Henderson and Lozzi [64] suggested another theory to determine the transition conditions for strong shocks and named it the **mechanical-equilibrium criterion**. They argued that a sudden pressure change due to the change of boundary conditions must be supported by either a compression wave or a rarefaction wave. Since no pressure discontinuity was observed during the transition process, the transition should take place when the reflected shock polar intersects the incident shock polar at the normal shock point in a shock polar plot. In order to compute the transition line from the mechanical-equilibrium criterion the three-shock theory [65] needs to be solved. Considering that only an IR configuration includes an independent length scale, Hornung *et al.* [62] proposed a so-called **length-scale criterion**, which is equivalent to the mechanical-equilibrium criterion in steady flows and boils down to the sonic criterion in pseudo-steady flows. After reviewing all four transition criteria, Ben-Dor summarized in his book [1] that the length-scale concept is the one that most likely leads to a proper prediction of the RR-IR transition because it successfully covers steady flow reflection and pseudo-steady flow reflection at the same time. As both an RR and IR are theoretically possible in the domain between the transition line resulted from the detachment criterion and that predicted by the mechanical-equilibrium criterion in the $\theta_w - M_s$ plane, i.e., the dual-solution domain, a hysteresis process can be expected. One possible reason for the discrepancy between the transition angle resulted from solving the

sonic criterion and that determined on the basis of visualization records is viscosity, which is neglected in the two-shock and three-shock theories. Skews [66] proved this by designing an experiment that aims to eliminate the influence of the boundary layer. By reflecting two identical shocks off each other in a bifurcated shock tube, the common-used wedge was effectively replaced by a virtual centerline in between the two shocks. Satisfactory synchronized results were obtained for different incident shock Mach numbers and the trend agreed very well with the sonic criterion.

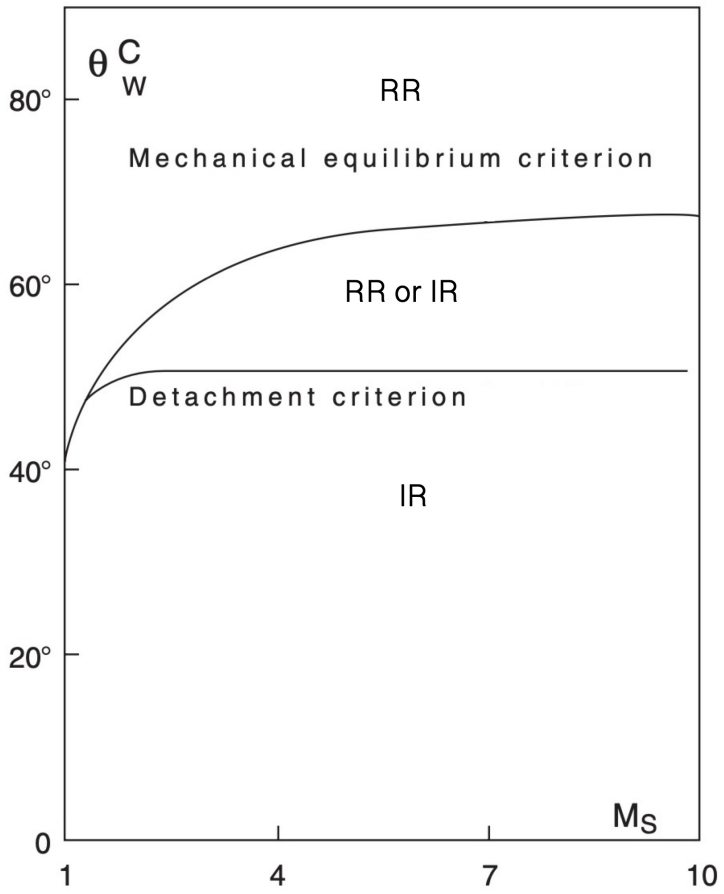

Figure 1.4: Domains of RR and IR as defined by the mechanical-equilibrium and the detachment criteria. In steady flows $\theta_w^c = 90^\circ - \phi_1$ and in pseudo-steady flows $\theta_w^c = \theta_w$. From [1], with permission from Springer.

To further explain different types of IR, Law and Glass [67] and Ben-Dor [68]

proposed a theory in which the shock reflection process can be considered to be a combination of two subprocesses, namely the shock-reflection process and the flow-deflection process. The reflected shock resulted from the shock-reflection process interacts the bow shock generated by the deflection of the shock-induced flow around a wedge corner, and a band of disturbances bridges the pressure gap, if any. Such a perturbation concept is inherently related to the sonic criterion. Following the perturbation concept, Ben-Dor developed analytical models for transitional Mach reflection (TMR) and double Mach reflection (DMR) [1]. The derivation was based on the assumption that the kink (the second triple point in DMR), defined as a position in the reflected shock where the curvature reverses, must be the furthest point that can be reached by the leading edge generated disturbances. Figure 1.5, from Ben-Dor [1], shows an example how irregular reflection pattern can be predicted for a given scenario using the models of the most recent knowledge and with experimental results. Except von-Neumann reflection (vNR), other irregular reflection patterns may also exist under special circumstances. One recent numerical investigation [69] proved the possibility of forming a three-shock confluence with a reflected shock bent towards the surface to which a Mach stem is attached. This shock configuration is unstable as the triple point is moving away from the surface in supersonic flows.

Compared to the well-established transition criteria for shock reflection in steady and pseudo-steady flows, the determination of critical conditions for a moving shock reflecting off a non-straight surface is still in dispute. This scenario belongs to shock reflection in unsteady flows as a continuous change of boundary conditions takes place during the shock reflection process. The reflected shock keeps adjusting itself to the changing wedge angle that leads to non-self-similar solutions. In contrast, pseudo-steady flow reflection is less complicated as it can maintain its self-similarity if no more independent scale lengths are introduced, for example, by shear stresses and heat flux [70]. Figure 1.6 shows another example of unsteady flow reflection as the result of the interaction between two initially

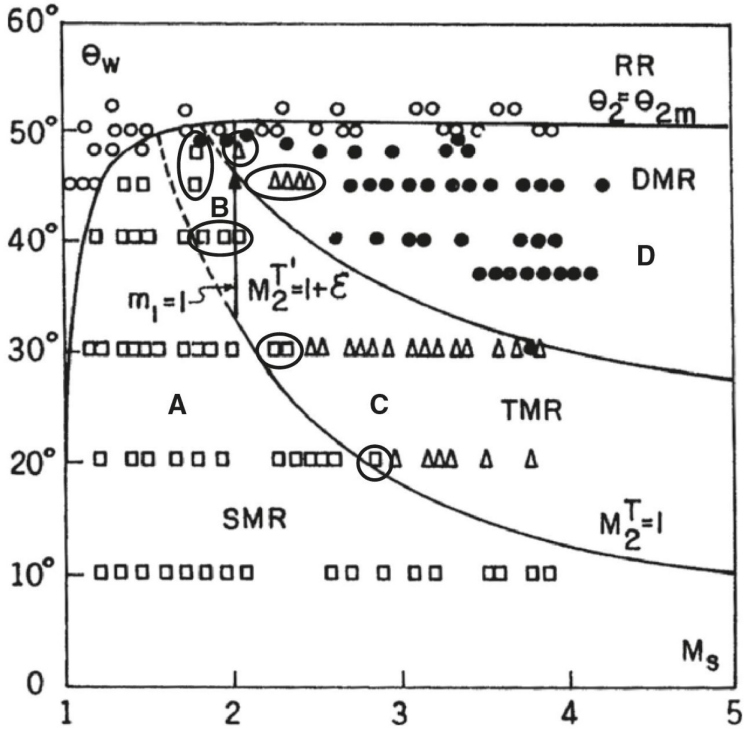

Figure 1.5: Transition lines that separate different types of shock wave reflections. Notation: SMR - single Mach reflection, PTMR - pseudo-transitional Mach reflection, TMR - transitional Mach reflection and DMR - double Mach reflection. From [1], with permission from Springer.

separated curved shocks. A closer inspection of the RR configuration and the subsequent (single) MR configuration is further illustrated in Figure 1.7. With regard to analytical models for shock reflection in unsteady flows, Ben-Dor [1] derived one for planar shock reflection off a cylindrical concave surface using the perturbation concept. Recently Geva *et al.* [71] introduced a modification to the two-shock theory to account for the flow behind the reflected shock propagating along the convex wedge. Based on the "no penetration" condition, a rotational velocity was imposed on the reflected shock about the reflection point in addition to a translational movement. Subsequently, they claimed that the RR-IR transition occurs when the reflected shock is perpendicular to the incident shock.

An extensive set of experiments were conducted by Skews and Kleine [72, 73] using

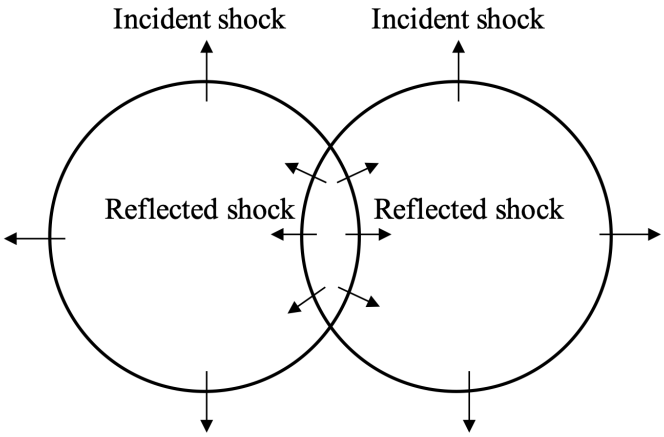

Figure 1.6: Schematic illustration of one scenario of shock wave reflection in unsteady flows: regular reflection between two initially separated curved shocks.

the perturbation technique to investigate the transition from RR to IR for a planar shock reflecting off a cylindrical convex surface. By placing transverse strips of adhesive tape on the wedge surface, finite perturbations can be generated when the incident shock passes by. Then the catch-up point, defined as where the flow reaches the sonic point with respect to the reflection point, is able to be determined by relating the evolution of shock configuration to the interaction between the disturbances and the shock pattern. This is done due to the fact that, in the upstream flow region of the catch-up point only regular reflection is possible according to the sonic criterion. Results showed that compared to the measured wedge angle at which the Mach stem became visible, the catch-up point appeared much earlier in the experiment, i.e., the RR-IR transition was delayed that occurred at a smaller angle than that predicted by the sonic criterion. Another case showing discrepancy between the catch-up point and the transition angle determined by visual inspection was reported by the same authors [74], where the corner generated signal was left behind the incident shock when the IR-RR transition initiated on a cylindrical concave surface. This indicates a delayed IR-RR transition that occurred at a larger angle than that predicted by the sonic criterion. The experiments of a planar shock reflecting off coupled surfaces were performed

by Skews and Blitterswijk [75] and Geva *et al.* [76]. In addition to noting the delay of the transition from RR to IR, they further asserted that shock reflection is influenced by the history of the flow process.

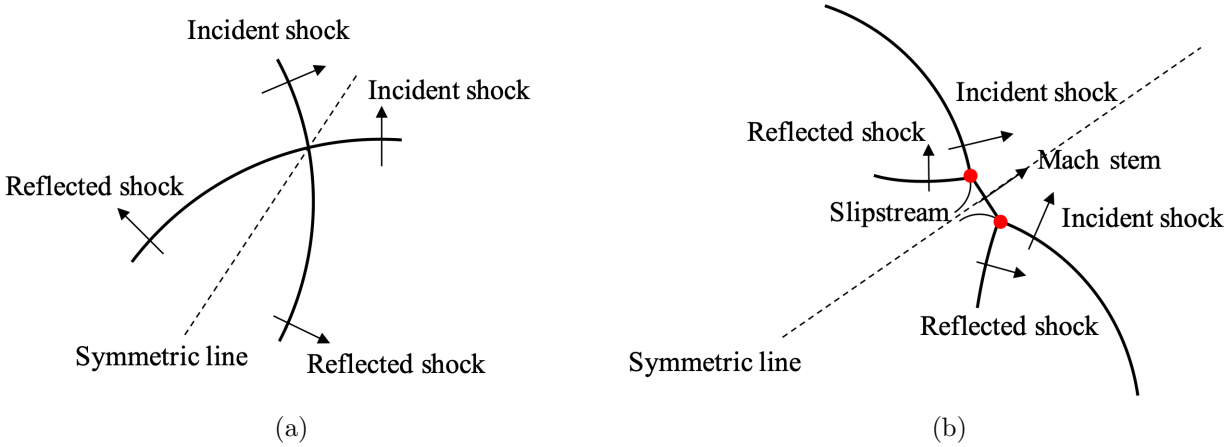

Figure 1.7: Schematic illustration of two basic shock wave reflection configurations in unsteady flows between two initially separated curved shocks: (a) Regular reflection; (b) Irregular reflection. Triple points represented by red dots.

However, most experiments carried out almost 30 years ago suffered from lack of resolution [77, 78, 79]. This is revealed by the experiment of Kleine *et al.* [80] who investigated the reflection of blast waves from a straight surface. Though the influence of the boundary layer was successfully eliminated by interacting two blasts in air, the measured transition spot from RR to IR based on visualization records still deviated substantially from the two-dimensional high-resolution numerical results. After reviewing all possible causes, they attributed such discrepancy to the non-optimal optical visualization system. Later, based on experiences Kleine *et al.* [81] proposed that, in order to observe the Mach stem at its very early stage an ideal visualization capability should allow the detection of minuscule flow features with a characteristic length below 0.05 mm.

Adequate resolution is also required for numerical simulations that solve inviscid conservation equations. Hryniewicki *et al.* [82] applied an Euler solver with adaptive mesh refinement (AMR) to measure the transition angle for a planar shock over a straight wedge.

Their results presented an RR-IR transition line no more than 1.6 degrees above the sonic criterion for an incident shock Mach number ranging from 1.6 to 4.0. Vignati and Guardone [83] numerically investigated the leading edge reflection pattern for cylindrically converging shock over convex obstacles. The resulting transition line that separates the RR and IR domains quantitatively agreed with that from the sonic criterion. More importantly, their results demonstrated that the suggestions made by Ben-Dor and Takayama [84] that shock reflection in unsteady flows can be interpreted as a sequence of pseudo-steady states were correct. A similar trend was also found by Gray and Skews [85] in their numerical simulation of a converging cylindrical shock reflection off a straight wedge. Hakkaki-Fard and Timofeev [86] numerically tested the perturbation concept for shock reflection in unsteady flows using different levels of refined grids. Compared to the analytical transition conditions obtained from solving a series of pseudo-steady shock reflection problems at each wedge angle, a good agreement was achieved using the most refined grid. Therefore, they claimed that the inconsistency between the sonic criterion applied to shock reflection in unsteady flows and the transition angles measured in Skews and Kleine's series of experiments [66, 73, 74] is due to insufficient optical resolution. By analyzing the interaction between the shock-reflection-induced disturbances and flow-deflection-induced disturbances with high-resolution simulations, Wang and Zhai [87] reached a conclusion that as long as the wedge is convex the flow in the vicinity of the reflection point will not be affected by the unsteady flow caused by wedge angle variation, so the transition is only determined by the local flow properties. That being said, the RR-IR transition can be predicted by the pseudo-steady flow criteria, regardless of wedge curvature, shock intensity and initial collision angle. There exist additional studies on shock reflection in unsteady flows utilizing geometrical shock dynamics including the works of Itoh *et al.* [88] and Barkhudarov *et al.* [89].

1.3 Contributions

This work will be presented with one chapter on two-dimensional GSD models (Chapter 2) and another one on a three-dimensional GSD algorithm developed by the author (Chapter 3). A final summary (Chapter 4) wraps up all the experiences gained from this project and further ideas are shared in the hope of shedding light on future efforts to extend the applications of GSD.

Major contributions made in this work are summarized as follows:

1. Presented a comprehensive study on two-dimensional geometrical shock dynamics and primary extensions that account for the post-shock flow effect.

2. Investigated the influence of the completeness of the post-shock flow term in an accurate description of blast propagation.

3. Proposed a general solution framework based on PGSD aiming at efficiently solving two-dimensional symmetric blast focusing problems.

4. Developed the MLS-PGSD model that can predict blast interactions in three-dimensional space.

Chapter 2

2D Geometrical Shock Dynamics

In general, to study shock interaction problems, the Navier-Stokes equations or the Euler equations, if only inviscid adiabatic compressible flows are considered, are solved numerically. The results involve all flow variables within the simulation domain such that shock fronts are either captured by detecting sharp discontinuous changes in the variables if shock-capturing schemes are applied, or explicitly introduced in the solution by shock-fitting schemes. However, since the shock front would have a large Mach number in compressive regions, a smaller time step is needed to satisfy the Courant-Friedrichs-Lewy (CFL) condition [90] to maintain the numerical stability. Moreover, the thickness of the shock front is usually on a much smaller scale compared to the grid size and large gradients are always present in the neighborhood of the shock front, so for the sake of accuracy a coarse grid resolution is not an option. Such a high demand for refined resolution in both time and space would result in expensive computational cost, which makes efficiency the major concern for implementing the Navier-Stokes or the Euler simulations.

For the purpose of efficiently modeling shock focusing problems numerically, geometrical treatment of shock behavior has received considerable attention over the last few decades. In 1957 Whitham [38, 39, 40] published a hyperbolic model that simplifies the full

Euler equations into descriptions of only the position, geometry and strength of a shock by applying linearized characteristic rules. The resulting theory called geometrical shock dynamics (GSD) successfully reduces the dimensionality of the problem by one [91, 92], and thus the complexity as well as the cost of the numerical computation is significantly reduced. In GSD theory, a shock front is discretized into numerous small particles and rays are introduced as orthogonal trajectories of the successive positions of these particles on the shock front. Then one treats each shock particle propagating along its own ray as a problem of shock propagation in a non-uniform tube with solid wall as illustrated in Figure 1.2. This allows the determination of a relation between the ray tube area and the shock Mach number — the "Area-Mach number $(A - M)$" relation, which is the fundamental component of GSD. Notably, the same relation was independently derived by Chester [37] and Chisnell [36], separately, such that the $A-M$ relation is also known as the CCW theory. It turns out that the results of GSD are accurate for shock propagation in uniform media with moderate strength if no large gradient exists in the post-shock flow. Various efforts were made to extend the application of GSD including modifications to accommodate for moving media [93], post-shock flow effects [3, 94, 95, 96] and detonation waves [97, 98].

2.1 $A - M$ Relation

A short review of the $A - M$ relation is first given as follows. Suppose a shock propagates down a tube of which the cross section area varies slowly as shown in Figure 2.1. If the cross section area of the tube is given as a function of the distance down the tube, $A(x)$, it is uniform before where the shock enters the tube and we write

$$A(x) = A_0 = \text{constant for } x = 0. \tag{2.1}$$

The tube starts to vary slowly in the neighborhood of $x = 0$ where the magnitude of change satisfies

$$\frac{|A(x) - A_0|}{A_0} \ll 1. \tag{2.2}$$

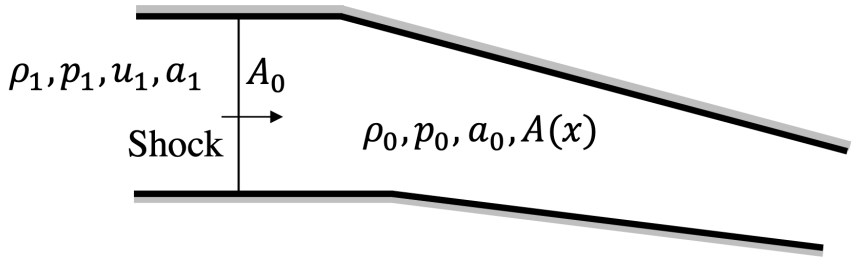

Figure 2.1: Schematic illustration of a shock propagating down a tube with varying cross section area.

By averaging the equations of one-dimensional inviscid compressible flow with varying cross section area for conservation of mass, momentum and energy along the tube, a set of partial differential equations (PDEs) dependent only upon the variable x can be obtained as follows

$$\partial_t \rho + u\partial_x \rho + \rho \partial_x u + \rho u \frac{A'(x)}{A(x)} = 0, \tag{2.3}$$

$$\partial_t u + u\partial_x u + \frac{\partial_x p}{\rho} = 0, \tag{2.4}$$

$$\partial_t p + u\partial_x p - a^2(\partial_t \rho + u\partial_x \rho) = 0. \tag{2.5}$$

Here ρ, u and p respectively denote density, particle velocity and pressure and $A'(x) = \frac{dA}{dx}$ in one-dimensional space. Speed of sound, a, is given by

$$a^2 = \frac{\gamma p}{\rho}, \tag{2.6}$$

where γ is the ratio of specific heats.

These equations hold everywhere in the smooth parts of the flow field that are

intersected by gasdynamic discontinuities, such as a shock in this case. At time instant $t = 0$ the incident shock arrives at position $x = 0$ and it separates the flow field into two regions: the undisturbed stationary state ahead of the shock with constant pressure p_0, density ρ_0 and speed of sound a_0, and the initial uniform state behind the shock featuring $u = u_1$, $a = a_1$, $p = p_1$ and $\rho = \rho_1$.

In the case of small variation of cross section area along the tube, it is reasonable to assume that the resulting disturbance to the initial state behind the shock and the change in shock Mach number is small. Therefore, the problem can be solved as a perturbation on the solution to the Euler equations for a uniform tube. The linearized differential equations are as follows

$$\partial_t(\delta\rho) + u_1\partial_x(\delta\rho) + \rho_1\partial_x(\delta u) + \rho_1 u_1\frac{A'(x)}{A_0} = 0, \tag{2.7}$$

$$\partial_t(\delta u) + u_1\partial_x(\delta u) + \frac{\partial_x(\delta p)}{\rho_1} = 0, \tag{2.8}$$

$$\partial_t(\delta p) + u_1\partial_x(\delta p) - a_1^2(\partial_t(\delta\rho) + u_1\partial_x(\delta\rho)) = 0, \tag{2.9}$$

where small perturbations are registered as $\delta\rho = \rho - \rho_1$, $A'(x) = (A(x) - A_0)'$ and so on.

These equations can be cast into characteristic form

$$C_+ : \{\partial_t + (u_1 + a_1)\partial_x\}((\delta p) + \rho_1 a_1(\delta u)) + \rho_1 u_1 a_1^2\frac{A'(x)}{A_0} = 0, \tag{2.10}$$

$$C_- : \{\partial_t + (u_1 - a_1)\partial_x\}((\delta p) - \rho_1 a_1(\delta u)) + \rho_1 u_1 a_1^2\frac{A'(x)}{A_0} = 0, \tag{2.11}$$

$$P : \{\partial_t + u_1\partial_x\}((\delta p) - a_1^2(\delta\rho)) = 0. \tag{2.12}$$

The general solution to the above compatibility equations can be obtained by integrating three families of characteristics featuring $\frac{dx}{dt} = u_1 + a_1$, $\frac{dx}{dt} = u_1 - a_1$ and $\frac{dx}{dt} = u_1$,

respectively

$$(\delta p) + \rho_1 a_1 (\delta u) = -\frac{\rho_1 u_1 a_1^2}{(u_1 + a_1)} \frac{A(x) - A_0}{A_0} + F(x - (u_1 + a_1)t), \tag{2.13}$$

$$(\delta p) - \rho_1 a_1 (\delta u) = -\frac{\rho_1 u_1 a_1^2}{(u_1 - a_1)} \frac{A(x) - A_0}{A_0} + G(x - (u_1 - a_1)t), \tag{2.14}$$

$$(\delta p) - a_1^2 (\delta \rho) = H(x - u_1 t), \tag{2.15}$$

where F, G and H are arbitrary functions. Each solution always holds along the corresponding characteristic line which is generally approximated by a straight line in an $x - t$ diagram. The three arbitrary functions can be determined from the initial conditions of the problem along with the boundary conditions at the shock. Because the C_+ characteristics behind the shock originate in the initial uniform state where $u = u_1$, $\rho = \rho_1$, $p = p_1$ and $A = A_0$, thus from equation (2.10) the arbitrary function F must be zero. It is this integration that provides sufficient information to determine the change in shock Mach number resulted from disturbances overtaking the shock. In fact, the other two functions G and H are not trivial and they are of subsidiary interest.

Considering the state immediately behind the shock are always related to the ambient undisturbed state ahead of the shock by the shock jump conditions

$$u = \frac{2a_0}{\gamma + 1} \left(M - \frac{1}{M} \right), \tag{2.16}$$

$$p = \frac{\rho_0 a_0^2}{\gamma(\gamma + 1)} \left[2\gamma M^2 - (\gamma - 1) \right], \tag{2.17}$$

$$\rho = \frac{(\gamma + 1)\rho_0 M^2}{(\gamma - 1)M^2 + 2}, \tag{2.18}$$

the perturbations at the shock can be expressed in terms of the change in Mach number

$$(\delta p) = p - p_1 = \frac{4\rho_0 a_0^2}{\gamma+1} M_0(M - M_0), \tag{2.19}$$

$$(\delta u) = u - u_1 = \frac{2}{\gamma+1} a_0 (1 + \frac{1}{M_0^2})(M - M_0), \tag{2.20}$$

where the shock Mach number is defined as the ratio of shock velocity in lab coordinates to the velocity of sound in the undisturbed gas, i.e., $M = \frac{U}{a_0}$, and γ is the ratio of specific heats that is set to be $\gamma = 1.4$ throughout this work.

When these equations are substituted into equation (2.10) with $F = 0$ we have

$$\left[\frac{4}{\gamma+1} M_0 + \frac{2}{\gamma+1}\left(1 + \frac{1}{M_0^2}\right)\frac{\rho_1 a_1}{\rho_0 a_0}\right](M - M_0) = -\frac{\rho_1 a_1^2}{\rho_0 a_0^2}\frac{u_1}{u_1 + a_1}\frac{A - A_0}{A_0}. \tag{2.21}$$

Once again, apply the shock jump conditions in equation (2.21) to express u_1, ρ_1 and a_1 in terms of M_0, and the following equation can be obtained

$$\frac{A - A_0}{A_0} = -g(M_0)(M - M_0), \tag{2.22}$$

where

$$g(M) = \frac{M}{M^2 - 1}\left(1 + \frac{2}{\gamma+1}\frac{1-\mu^2}{\mu}\right)\left((1 + 2\mu + \frac{1}{M^2}\right), \text{and} \tag{2.23}$$

$$\mu^2 = \frac{(\gamma-1)M^2 + 2}{2\gamma M^2 - (\gamma - 1)}. \tag{2.24}$$

Though a tube varies slowly, massive changes in cross section area accumulate over a sufficiently large length. To make the small perturbation theory work, the tube can be broken down into successive small lengths such that $A(x)$ only changes slightly along each tube element. Therefore, in each of such elements it is admissible to linearize about the local conditions and develop a small perturbation theory as described above. However, it

should be noted that the state at the entry to each element is not strictly uniform except the very first one due to error accumulation over the successive small tube elements, which complicates the problem by having a non-zero function F in equation (2.10). But, if such imperfection is neglected, equation (2.22) can be applied to each tube element with A_0 and M_0 taken to be the cross section area and shock Mach number at the entry to the subsection. This leads to the differential form of a relation, $M = M(A)$, which is also called the $A - M$ relation, expressed as

$$\frac{1}{A}\frac{dA}{dM} = -g(M). \tag{2.25}$$

The solution of equation (2.25) by integral may be written

$$\frac{A}{A_0} = \frac{f(M)}{f(M_0)}, \tag{2.26}$$

where

$$f(M) = \exp\left\{-\int_1^M g(\omega)d\omega\right\}. \tag{2.27}$$

For one-dimensional problems where a shock is propagating down a tube with varying cross section area, the ray tube is naturally defined by the solid walls and the area term A appearing in all above equations is exactly the ray tube area. However, if a shock front in a higher dimensional space is considered and no solid walls exist, the approximation of the area term becomes the priority for solving the problem. If a shock front is assumed to consist of numerous fluid particles, rays can then be introduced as orthogonal trajectories of the successive positions of the particles on the shock front. One way to understand these rays is to view them as particle paths, which are equivalent to solid walls in inviscid flows, such that the area term can be defined as the cross section

area of the tube bounded by rays. As a result, the shock front propagation problem breaks down into descriptions of shock front elements propagating down individual ray tubes.

Though such approximation of ray tubes and corresponding areas may be imperfect for a shock front with complex geometry, it is independent of the motion rule that governs the propagation of each shock element. If the motion rule defines how the local Mach number varies with the ray tube area, the inverse function of equation (2.26) can be used to compute the Mach number given current ray tube area and reference values. It is worth noting that $f(M)$ is a monotonically decreasing function that approaches infinity when the shock is attenuated into a Mach wave. Though the $A - M$ relation is derived based on the one-dimensional Euler equations, Whitham [40] argues that the results may be extended for spherical shocks of moderate strength. This makes the $A - M$ relation the core of geometrical treatment of shock propagation problems in two- and three-dimensional space.

2.2 Geometrical Shock Dynamics

If a shock front at time t is supposed to be in the form:

$$\alpha(\boldsymbol{x}) = a_0 t, \tag{2.28}$$

where a_0 is still the undisturbed speed of sound, then successive shock front positions are given by the family of implicit surfaces $S(\boldsymbol{x}, t) = \alpha(\boldsymbol{x}) - a_0 t = 0$. For example, at a specific time instant t_1, all the particles on the shock front can be found at coordinates satisfying the instantaneous surface function, i.e., $\{\boldsymbol{x} | \alpha(\boldsymbol{x}) - a_0 t_1 = 0\}$. Viewed this way, the area of each elementary ray tube is related to the shock front position. Moreover, the instantaneous Mach number at any particle should be able to be determined in terms of $\alpha(\boldsymbol{x})$ as the shock motion is indicated by its successive positions. The $A - M$ relation then provides a bridge to derive $\alpha(\boldsymbol{x})$.

Partial differential equations for geometrical shock dynamics were given by Whitham in [40] as

$$M = \frac{1}{\|\nabla \alpha\|}, \tag{2.29}$$

$$\nabla \cdot \frac{\boldsymbol{n}}{A} = 0, \tag{2.30}$$

$$\frac{A}{A_0} = \frac{f(M)}{f(M_0)}, \tag{2.31}$$

where $\boldsymbol{n} = \frac{\nabla \alpha}{\|\nabla \alpha\|}$ is the unit normal to the shock front.

2.3 Numerical Methods

Since only a small number of problems can be solved analytically using the method of GSD, many algorithms were developed to numerically implement GSD models including front tracking methods [3, 41, 42, 43, 92, 94, 95, 99, 100], finite difference [91] and finite volume schemes [101, 102] based on the conservation form of GSD, and a recent level-set fast marching approach [103], just to name a few. Among all these schemes, the front tracking-based Lagrangian schemes are the most popular ones that have been used for a wide range of shock dynamics problems since accuracy and speed can be well balanced. First developed in two dimensions by Henshaw *et al.* [41] and then extended to three dimensions by Schwendeman [42], the front tracking methods discretize a shock front into particles. These particles advance along individual rays normal to the shock front subjected to the local Mach number. Following this concept, Schwendeman [99] computed the propagation of shock waves in gases with non-uniform properties. Best [94] and Peace *et al.* [95] applied the front tracking method to quantitatively investigate influence of the post-shock flow effect on the accuracy of GSD by taking into consideration the interaction between the shock front and the non-uniform flow behind. Qiu and Eliasson [43, 3] used

this approach to study blast interaction to take advantage of its fast speed and achieved a good agreement with results from the Euler simulations. Ridoux *et al.* [100] extended Henshaw's Lagrangian scheme to remove its limitation for expansive shocks.

The Lagrangian schemes to solve various GSD models for two- and three-dimensional shock propagation problems in this work are based on the front tracking method. Instead of solving partial differential equations (2.29) – (2.31), the idea is to derive a kinematic equation purely from geometry in addition to the $A - M$ relation.

If $\boldsymbol{x}$ is used to denote the position vector of a particle on the shock front, then the shock front kinematics is given by

$$\frac{d\boldsymbol{x}}{dt} = a_0 M \boldsymbol{n}, \tag{2.32}$$

where $\boldsymbol{n}$ refers to the unit normal to the shock front that defines the propagation direction of the particle.

The $A - M$ relation is preserved, but in a numerically manageable form. Through some algebraic manipulation a kinetic relation is derived from the $A - M$ relation as

$$\frac{dM}{dt} = \frac{-a_0 M}{g(M)} \frac{A'}{A}, \tag{2.33}$$

where $g(M)$ is given in equation (2.22).

The last piece of information needed for integrating equations (2.32) – (2.33) is an explicit expression for $\frac{A'}{A} \equiv \frac{1}{A}\frac{dA}{dn}$. Best [94] for the first time mathematically deduced $\frac{A'}{A}$ for a diverging shock. Since the problems are restricted to two-dimensional flows, the shock front is represented as a one-dimensional curve and arc-length becomes the most natural choice of the argument for all variables. Considering that the arc-length is also a function of time, $\boldsymbol{x}$, $\boldsymbol{n}$ and M are written as $\boldsymbol{x}(s(t))$, $\boldsymbol{n}(s(t))$ and $M(s(t))$, respectively, in the following expressions for illustration purpose. Then $\frac{A'}{A}$ is given as a dot product as

follows

$$\frac{A'}{A} = \frac{d\boldsymbol{x}(s(t))}{ds(t)} \cdot \frac{d\boldsymbol{n}(s(t))}{ds(t)}, \tag{2.34}$$

where

$$\boldsymbol{n}(s(t)) = \left(\frac{dy(s(t))}{ds(t)}, -\frac{dx(s(t))}{ds(t)} \right). \tag{2.35}$$

A closer inspection of equation (2.34) reveals the fact that $\frac{A'}{A}$ is indeed the curvature. This can be seen by substituting equation (2.35) into the right side of equation (2.34), which yields curvature, κ,

$$\frac{A'}{A} = x'(s)y''(s) - x''(s)y'(s) = \kappa(s). \tag{2.36}$$

Here it should be noted that, since equation (2.36) is derived for a diverging shock on which any part has a convex shape, a positive curvature should always be obtained as the result of such geometry. In contrast, a negative curvature is expected in concave regions where the area of shock surface is decreasing.

All quantities required for equations (2.32) and (2.33) are thus known. The two-dimensional GSD model now can be numerically solved at a set of particles $\boldsymbol{x_i}$ that represent the shock front. The discretized forms of the ordinary differential equations (ODEs) become

$$\frac{d\boldsymbol{x}_i}{dt} = a_0 M_i \boldsymbol{n}_i, \tag{2.37}$$

$$\frac{dM_i}{dt} = \frac{-a_0 M_i}{g(M_i)} \kappa_i, \tag{2.38}$$

for $i = 1, 2, ...N$, and should be integrated simultaneously. This can be achieved by, for example, adopting a third-order Runge-Kutta scheme [104].

For the purpose of evaluating curvature, spline interpolation is fitted to the shock front with the parameterization with respect to arc-length. If s_i is used to denote the arc-length along the curve from the first particle to particle i, it can be approximated as below with satisfying precision if the particle density is sufficient

$$s_i(t) = \begin{cases} 0, & \text{if } i = 1 \\ s_{i-1}(t) + \|\boldsymbol{x}_i(t) - \boldsymbol{x}_{i-1}(t)\|. & \text{if } i = 2, 3, ...N \end{cases} \tag{2.39}$$

Then, the first- and second-order derivatives required for equation (2.36) can be obtained at particles from spline interpolation. It is worth noting that equation (2.36) is only valid for unit-speed curves that are usually in the form of being parameterized with respect to arc-length. If a curve is not parameterized by arc-length, a correction factor that accounts for the speed of the curve should be added to the function of curvature. So an approximation of arc-length is necessary, which requires the shock front to be adequately resolved. Guided by the resolution conditions proposed by Henshaw *et al.* [41], an appropriate number of particles that balances accuracy and speed should be selected to represent the shock front. If the average arc-length between particles is denoted by ds_{avg}, the criterion is given by

$$\Delta s_{avg}(0) = \frac{s_N(0)}{N} = k_1 \ll 1. \tag{2.40}$$

Such condition provides a lower bound on the number of particles, and usually $k_1 = 0.01$. Seeing that particles tend to spread out in expansive regions and cluster together in compressive regions, in order to maintain shock front resolution throughout the Lagrangian simulation a scheme that adds or deletes particles according to the local density is needed.

The particle spacing is checked every few time steps and demands that

$$\sigma_{min} \leq \sigma_i(t) = \frac{\Delta s_i(t)}{\Delta s_{avg}(t)} \leq \sigma_{max} \text{ for } i = 2, 3, ...N, \tag{2.41}$$

where $\Delta s_i(t) = s_i(t) - s_{i-1}(t)$, and σ_{min} and σ_{max} are typically set to be 0.5 and 1.5, respectively. If $\sigma_i(t) > \sigma_{max}$, a point is added using spline interpolation evaluated at $\frac{1}{2}(s_i(t) + s_{i-1}(t))$; if $\sigma_i(t) < \sigma_{min}$, the particle $\boldsymbol{x}_i$ is deleted. By removing redundant particles, not only is the numerical cost reduced, but the numerical stability is ensured at each time step. Moreover, since rays tend to cross each other, triple points form in compressive regions of the shock front, and therefore removing some clustered particles enables the triple points to be effectively fitted into the shock front.

The two-step smoothing procedure is another component of the numerical implementation of GSD that is used to dampen high frequency errors in $\boldsymbol{x}_i(t)$ and $M_i(t)$. If $\tilde{\boldsymbol{x}}_i$ and $\tilde{M}_i(t)$ stand for the smoothed position and the smoothed value of Mach number associated with the i'th particle, respectively, then the smoothing procedure is given by

$$\tilde{\boldsymbol{x}}_i(t) = \frac{1}{2}\left(\boldsymbol{x}_{i-1}(t) + \boldsymbol{x}_{i+1}(t)\right), \tag{2.42}$$

$$\tilde{M}_i(t) = \frac{1}{2}\left(M_{i-1}(t) + M_{i+1}(t)\right), \tag{2.43}$$

where first i-even and then i-odd particles are scanned. Best [94] found it desirable to apply such a smoothing procedure for compressive flows every few time steps, but that is unnecessary in the case of expansive flows.

An appropriate time step size is guided by the CFL condition. Following [41] the scheme used in this work that provides the upper bound on the selection of a time step,

Δt, is given by

$$\frac{\Delta t}{\Delta s_{min}(t)} = \frac{\Delta t}{\sigma_{min}\Delta s_{avg}} < k_2, \tag{2.44}$$

where the constant k_2 is usually taken to be 0.2.

2.4 Application of GSD to Blast Waves

It is well known that GSD is accurate for shock waves with constant properties behind [40, 41, 3, 91, 96], but blast waves are the ones that occur most frequently in both nature and man-made applications. For a blast wave flow properties behind the shock front are decaying exponentially as illustrated in Figure 1.1. This contradicts the assumption made in deriving GSD, which requires a uniform state behind the shock. To investigate whether the accuracy is compromised if such assumption is violated, in this section Whitham's original GSD model will be numerically implemented for the propagation of a single cylindrical blast and compared to both the analytical and Euler solutions.

Once a shock front is discretized, the position and Mach number of each particle are required by the Lagrangian scheme as initial input. Such information can be obtained from empirical laws or numerical solutions for a particular explosion. In this work Bach and Lee's analytical solution to a point-blast wave [105] as well as the Euler equations of gas dynamics are solved not only to provide initial conditions for the Lagrangian scheme that solves GSD but also to be used as references to evaluate the accuracy of various GSD models in predicting blast motion.

The analytical solution will be elaborated on in detail in Section 2.6 along with an improved GSD model. In terms of solving the Euler equations, a brief discussion is provided here. The primary solver used in this work for two- and three-dimensional shock dynamics problems is Overture [106], an open-source framework with both incompressible

and compressible flow solver capabilities. To simulate blast propagation in air, conservation laws of mass, momentum and energy for inviscid compressible flows are solved with a second-order Godunov scheme [107]. The unsteady Euler equations are represented in conservation form as

$$\frac{\partial \mathbf{Q}}{\partial t} + \frac{\partial \mathbf{E}}{\partial x} + \frac{\partial \mathbf{F}}{\partial y} + \frac{\partial \mathbf{G}}{\partial z} = 0, \tag{2.45}$$

with $\mathbf{Q}$, $\mathbf{E}$, $\mathbf{F}$ and $\mathbf{G}$ given by

$$\mathbf{Q} = \begin{bmatrix} \rho \\ \rho u \\ \rho v \\ \rho w \\ e \end{bmatrix}, \mathbf{E} = \begin{bmatrix} \rho u \\ \rho u^2 + p \\ \rho uv \\ \rho uw \\ (e+p)u \end{bmatrix}, \mathbf{F} = \begin{bmatrix} \rho v \\ \rho vu \\ \rho v^2 + p \\ \rho vw \\ (e+p)v \end{bmatrix} \mathbf{G} = \begin{bmatrix} \rho w \\ \rho wu \\ \rho wv \\ \rho w^2 + p \\ (e+p)w \end{bmatrix}, \tag{2.46}$$

where ρ is the density, u, v and w are the velocity components in the x-, y- and z-directions, and e is the energy per unit volume. Pressure p is related to the above variables by the equation of state (EOS) for the perfect gas

$$p = (\gamma - 1)\left[e - \frac{\rho(u^2 + v^2 + w^2)}{2}\right], \tag{2.47}$$

The conversion of the Euler equations from three to two dimensions can be simply achieved by discarding all terms in the z-direction.

Instead of simulating a condensed energy source, the PDE solver starts with a specific wave front of finite size such that extremely fine mesh and severe numerical oscillations arising from sharp discontinuities at the wave front can be avoided. The initial conditions used for the Euler equations are based on Taylor's similarity law [35]. This similarity law describes the distribution of flow properties within the blast front by assuming appropriate

similarity assumptions for an expanding blast of constant total energy E:

$$\frac{p}{p_0} = R_s^{-3}(t) f_1(\xi), \tag{2.48}$$

$$\frac{\rho}{\rho_0} = \psi(\xi), \tag{2.49}$$

$$u = R_s^{-\frac{3}{2}}(t) \phi_1(\xi). \tag{2.50}$$

Here, p_0 and ρ_0 denotes the ambient pressure and density ahead of the blast front. Nondimensionalized variable, $\xi = \frac{r}{R_s}$, the ratio between the radial distance measured from the explosion center and the radius of the blast front at time instant t, is used as the independent variable for functions f_1, ψ and ϕ_1.

Furthermore, the non-dimensional form of f_1 and ϕ_1 can be achieved by

$$f = \frac{a_0^2 f_1}{C^2}, \tag{2.51}$$

$$\phi = \frac{\phi_1}{C}, \tag{2.52}$$

where a_0 is the speed of sound in ambient air and C is a constant related to E.

Applying these assumptions to the conservation equations of mass, momentum, and equation of state for a spherically symmetric flow yields the non-dimensional forms as follows

$$\dot{\phi}(\xi - \phi) = \frac{\dot{f}}{\gamma \psi} - \frac{3}{2}\phi, \tag{2.53}$$

$$\frac{\dot{\psi}}{\psi} = \frac{\dot{\phi} + 2\phi/\xi}{\xi - \phi}, \tag{2.54}$$

$$3f + \xi \dot{f} + \frac{\gamma \dot{\psi}}{\psi} f(-\xi + \phi) - \phi \dot{f} = 0, \tag{2.55}$$

where $\dot{f} \equiv \frac{df}{dt}$ and so on.

The three ODEs can be numerically integrated simultaneously from $\xi = 1$ to 0. The values of f, ψ and ϕ at the blast front ($\xi = 1$) are determined by the shock jump conditions with an assumption of $p_s \gg p_0$ for a strong blast at its very early stage. Thus the distributions of pressure, density and particle velocity within the blast front can be obtained as shown in Figure 2.2, and remain the same for any total energy, E.

Approximate formulas that further reduce the effort to compute initial conditions for the Euler equations are presented by Taylor [35]. The release of energy, E, from the explosion only affects the maximum pressure and particle velocity at blast front by

$$p_{\max} = 0.155 R_s^{-3} E, \tag{2.56}$$

$$u_{\max} = 0.360 R_s^{-\frac{3}{2}} \left(\frac{E}{\rho_0} \right)^{\frac{1}{2}}. \tag{2.57}$$

As indicated by equations (2.56) – (2.57), once the initial radius is chosen, all initial conditions are determined for the numerical simulation of a spherical blast given energy. Throughout this work, spherical blasts are simulated with an initial radius $R_0 = 1.5$ mm, which is the same as that used by Jiang *et al.* [4] who performed Euler simulations to investigate the motion of a spherical micro-blast wave induced by laser beam focusing. For two-dimensional blast dynamics problems, the similarity law is modified to generate initial conditions for cylindrical blasts [108] with the same initial radius, i.e., $R_0 = 1.5$ mm. The verification of the Euler solver and the initial conditions, and the grid independence study can be found in Appendix A.

Both Bach and Lee's analytical solution and the Euler equations for a single cylindrical point-blast were numerically solved with an initial energy input $E_0 = 8,000$ J/m. To study the shock front behavior during its expansion, the variation of Mach number as a function of radius (i.e., $M - R$) is shown in Figure 2.3. A discrepancy can be observed between the $M - R$ curves from the analytical and Euler solutions at an early stage when

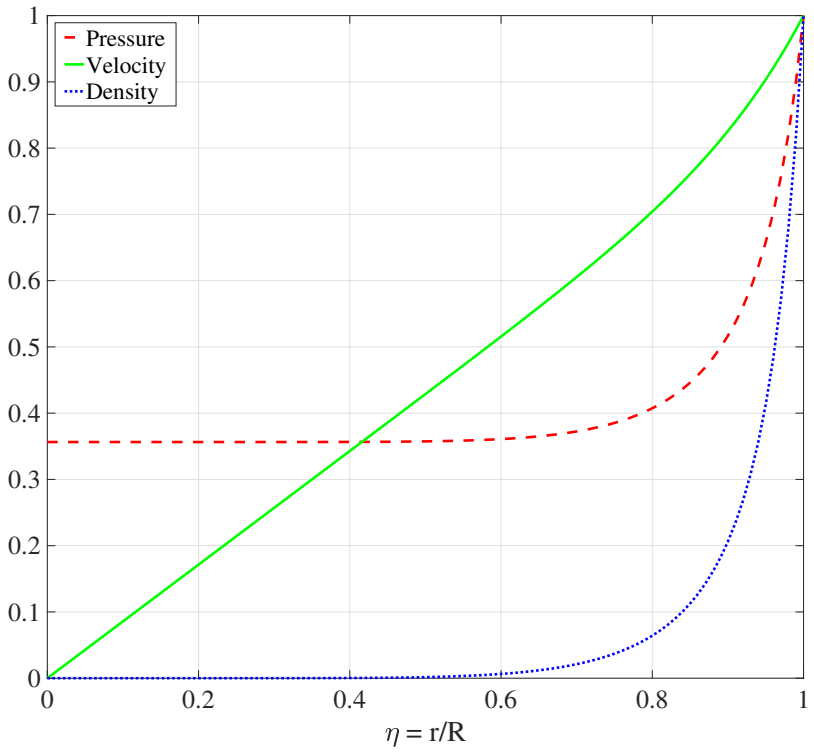

Figure 2.2: Normalized initial conditions based on Taylor's similarity law [84].

the blast front is very strong. The two curves gradually get closer as the blast front further expands and almost agree once the radius exceeds its initial size by a factor of 20.

Whitham's original GSD model represented by the system of equations (2.32) – (2.33) was solved with the Lagrangian scheme presented in Section 2.6 to verify its accuracy in predicting the blast motion. To start the scheme a shock front was represented by particles placed on a circle with a radius of 10.06 mm with spacing $\Delta s \approx 0.1$ mm. The corresponding Mach number at $R_0 = 10.06$ mm was found to be 11.81 and 9.76 according to the Euler simulation and analytical solution, respectively. Smoothing procedures are not needed for a single blast expansion but particles would be added if the local particle density becomes scarce as the blast front area increases. The GSD results are presented in Figure 2.3 where each resulting $M - R$ curve lies well above its corresponding reference. This

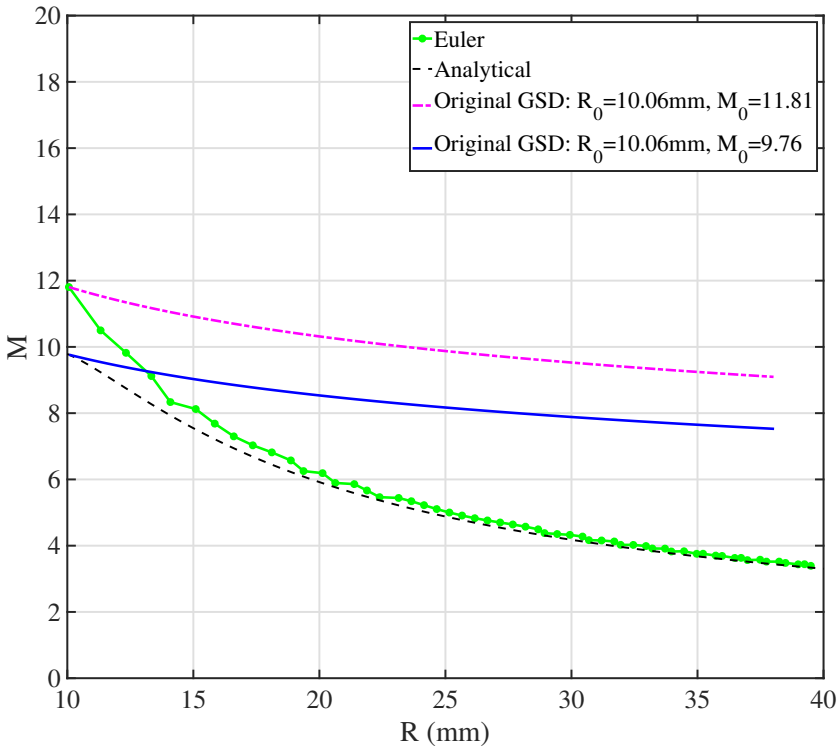

Figure 2.3: $M - R$ plots of the propagation of a single cylindrical blast in air. Initial conditions: $E_0 = 8,000$ J/m for the Euler and analytical solutions.

indicates that the blast front was not sufficiently attenuated throughout the Lagrangian simulation by the original GSD model.

2.5 Post-shock Flow Effect

To explore the reason why GSD falls short of accuracy when being applied to blast waves, the derivation of Whitham's original model needs to be reevaluated. Recall that when deducing the differential form of the $A - M$ relation that is valid only for a sufficiently large length in a non-uniform tube, the small perturbation theory is applied to each tube element by linearizing about the local conditions. That being said, in practice the initial uniform properties behind the shock, u_1, a_1, p_1 and ρ_1 in equation (2.10) are replaced by

the local properties, u, a, p and ρ, respectively. So the whole derivation of the $A-M$ relation is indeed just the substitution of the shock jump conditions as a function of Mach number into the compatibility equation along the C_+ characteristics. Then the resulting differential equation gives the variation of M with x (also with A since $A = A(x)$).

The compatibility equation along the C_+ characteristics without linearization is

$$\frac{\partial p}{\partial t} + (u+a)\frac{\partial p}{\partial x} + (\rho a)\left(\frac{\partial u}{\partial t} + (u+a)\frac{\partial u}{\partial x}\right) + \rho u a^2 \frac{A'(x)}{A(x)} = 0, \tag{2.58}$$

which can be rearranged into

$$\frac{\partial p}{\partial x} + \rho a \frac{\partial u}{\partial x} = -\frac{1}{u+a}\left(\frac{\partial p}{\partial t} + \rho a \frac{\partial u}{\partial t} + \rho u a^2 \frac{A'(x)}{A(x)}\right). \tag{2.59}$$

Consider that all total derivatives consist of changes of the property with respect to both time and location, then $d_t p$ and $d_t u$ along the shock trajectory are

$$\frac{dp}{dt} = \frac{\partial p}{\partial t} + a_0 M \frac{\partial p}{\partial x}, \tag{2.60}$$

$$\frac{du}{dt} = \frac{\partial u}{\partial t} + a_0 M \frac{\partial u}{\partial x}. \tag{2.61}$$

Multiply equation (2.61) by ρa then add it to equation (2.60) to get

$$\frac{dp}{dt} + \rho a \frac{du}{dt} = \frac{\partial p}{\partial t} + \rho a \frac{\partial u}{\partial t} + a_0 M \left(\frac{\partial p}{\partial x} + \rho a \frac{\partial u}{\partial x}\right). \tag{2.62}$$

Substituting equation (2.59) into the right hand side of equation (2.62) with some algebraic manipulations yields

$$\left(\frac{dp}{dM} + \rho a \frac{du}{dM}\right)\frac{dM}{dt} = -\left[a_0 M \frac{\rho u a^2}{u+a}\frac{A'(x)}{A} + \left(\frac{a_0 M}{u+a} - 1\right)\left(\frac{\partial p}{\partial t} + \rho a \frac{\partial u}{\partial t}\right)\right]. \tag{2.63}$$

It is not difficult to find that the equivalence of equation (2.63) to the $A-M$ relation,

(2.33), is established by the use of shock jump conditions in determination of $\frac{dp}{dM}$ and $\frac{du}{dM}$, along with the truncation of the term $\left(\frac{a_0 M}{u+a} - 1\right)\left(\frac{\partial p}{\partial t} + \rho a \frac{\partial u}{\partial t}\right)$. Now, it is necessary to make some comments about the accuracy of the $A - M$ relation derived in the manner presented in Section 2.1. Best [94] concluded that the criterion of Whitham's $A - M$ relation being a good approximation through linearization is

$$a_0 M \frac{\rho u a^2}{u+a}\left|\frac{A'(x)}{A}\right| \gg \left|\frac{a_0 M}{u+a} - 1\right|\left|\frac{\partial p}{\partial t} + \rho a \frac{\partial u}{\partial t}\right|. \tag{2.64}$$

Equation (2.64) lists two sources of disturbances that possibly modify the shock front: the term on the left hand side of this inequality characterizes the effect of changing area upon the shock front, and the right hand side represents the interaction between the shock front and the flow behind. The expression $\frac{\partial p}{\partial t} + \rho a \frac{\partial u}{\partial t}$ is called the "post-shock flow term" as it measures the non-uniformity of the flow behind the shock. It is equal to zero for a uniform flow, which is exactly the case of applying small perturbation theory to deduce the $A - M$ relation as done by Whitham. Though the change of area upon the shock front disturbs the flow immediately behind it such that $\left|\frac{\partial p}{\partial t} + \rho a \frac{\partial u}{\partial t}\right| > 0$, its absolute value is usually very small along the C_+ characteristics originating in a uniform state. This justifies the appropriateness of using the $A - M$ relation to describe the motion of an initially uniform shock wave. However, this term can also be fairly large if a strong gradient exists in the flow just behind the shock front. To what extent such non-uniformity affects the shock motion is determined by $\left|\frac{a_0 M}{u+a} - 1\right|$, which indicates the coincidence of the C_+ characteristic line and the shock trajectory. Recall that when deriving the $A - M$ relation the compatibility equation along the C_+ characteristics is applied at the shock front by using the shock jump conditions, but such being a good approximation requires the leading C_+ characteristic to coincide with the shock trajectory. This is true only for the case in the sonic limit, i.e., $M \to 1$, where the disturbances stemming from the non-uniform flow behind the shock

propagate along the C_+ characteristics, but do not meet the shock front so they impose no influence on its motion. On the other hand, if $M \to \infty$, Best reported that $\left|\frac{a_0 M}{u+a} - 1\right|$ tends to be 0.215 for $\gamma = 1.4$ [94], which suggests the significance of the post-shock flow effect as in this situation disturbances overtake and then modify the shock front. Consequently, since $\left(\frac{a_0 M}{u+a} - 1\right)\left(\frac{\partial p}{\partial t} + \rho a \frac{\partial u}{\partial t}\right)$ is not zero for most cases, the $A - M$ relation is accurate only when the effect of area change upon the shock dominates that of the interaction between the shock front and the non-uniform flow behind.

For the case of shocks with decaying properties behind, blast waves for example, the gradient in the flow immediately behind the shock front can make the term $\left|\frac{\partial p}{\partial t} + \rho a \frac{\partial u}{\partial t}\right|$ very large. As long as the shock is of moderate strength, disturbances will catch up with the shock front and modify it. The inequality in criterion (2.64) is then violated since $\left(\frac{a_0 M}{u+a} - 1\right)\left(\frac{\partial p}{\partial t} + \rho a \frac{\partial u}{\partial t}\right)$ becomes as significant as $a_0 M \frac{\rho u a^2}{u+a} \frac{A'(x)}{A}$ in terms of magnitude. Therefore, to make the $A - M$ relation appropriate for this type of shocks, a correction term must be added that accounts for the post-shock flow effect, and obviously, the truncated term itself is a good indication. A generalization of GSD was carried out by Best [94], who closed the motion rule for shock propagation by an infinite sequence of ordinary differential equations given as follows

$$\frac{dM}{dt} = \frac{-a_0 M}{d_M p + \rho a d_M u}\left[\left(\frac{\rho u a^2}{u+a}\right)\frac{A'}{A} + \left(\frac{1}{u+a} - \frac{1}{a_0 M}\right) Q_1\right], \tag{2.65}$$

$$\begin{aligned}\frac{dQ_k}{dt} = & -a_0 M\left\{\frac{\partial^k}{\partial t}\left(\frac{\rho u a^2}{u+a}\right)\frac{A'}{A} + \sum_{i=1}^{k}\left[\binom{k}{i}\frac{\partial^i}{\partial t}\left(\frac{1}{u+a}\right) Q_{k-i+1}\right]\right. \\ & \left. + \frac{\partial^{k-1}}{\partial t}\left(\frac{\partial(\rho a)}{\partial t}\frac{\partial u}{\partial x} - \frac{\partial(\rho a)}{\partial x}\frac{\partial u}{\partial t}\right) + \left(\frac{1}{u+a} - \frac{1}{a_0 M}\right) Q_{k+1}\right\},\end{aligned} \tag{2.66}$$

for $k = 1, 2, , ...$, where

$$Q_k = \frac{\partial^{k-1}}{\partial t}\left(\frac{\partial p}{\partial t} + \rho a \frac{\partial u}{\partial t}\right). \tag{2.67}$$

The above closed system can be written in a concise form by setting M to be Q_0: $d_t Q_k = f(Q_0, ..., Q_{k+1}, A'/A)$, for $k = 0, 1, ...$ Evidently the expression for $d_t Q_k$ depends on Q_{k+1}, such that each differential equation in the system is coupled to its successor in the sequence. By truncating all the terms involving Q_{k+1}, a kth-order complete GSD system is achieved. It is so named because the post-shock flow effect is only partially complete as the result of nonexistence of derivatives of orders higher than k. For example, the front-tracking based two-dimensional original GSD model consisting of equations (2.32) and (2.33) only achieves zeroth-order completeness. Moreover, if Q_1 is preserved but terms involving Q_2 are discarded, the **first-order complete GSD model** is obtained as follows, which contains three coupled ordinary differential equations for three unknowns, namely, $\boldsymbol{x}(t)$, $M(t)$ and $Q_1(t)$:

$$\frac{d\boldsymbol{x}}{dt} = a_0 M \boldsymbol{n}, \tag{2.68}$$

$$\frac{dM}{dt} = \frac{-a_0 M}{d_M p + \rho a d_M u} \left[\left(\frac{\rho u a^2}{u+a} \right) \frac{A'}{A} + \left(\frac{1}{u+a} - \frac{1}{a_0 M} \right) Q_1 \right], \tag{2.69}$$

$$\frac{dQ_1}{dt} = -a_0 M \left[\frac{\partial}{\partial t} \left(\frac{\rho u a^2}{u+a} \right) \frac{A'}{A} + \frac{\partial(\rho a)}{\partial t} \frac{\partial u}{\partial x} - \frac{\partial(\rho a)}{\partial x} \frac{\partial u}{\partial t} + \frac{\partial}{\partial t} \left(\frac{1}{u+a} \right) Q_1 \right]. \tag{2.70}$$

Once initial conditions are provided, the system can then be solved by numerical integration.

The first-order complete GSD model was solved with the Lagrangian scheme for the same case as the original GSD model presented in Section 2.3. In addition to the initial blast radius and Mach number, the initial value of Q_1 is also necessary to start the scheme. Since Q_1 requires partial derivatives with respect to time and location, which are not present until the scheme advances at least one time step, it is possible to estimate its value at $R_0 = 10.06$ mm only if prior knowledge exists. By estimating $d_x M$ from the analytical solution, all partial derivatives can be computed as functions of $d_x M$ [94] and then Q_1 follows. As a result, the $M - R$ curves obtained from solving the first-order complete GSD model with appropriate initial conditions are shown in Figure 2.4. Obviously, though

closing the system with one more equation untruncated (i.e., $\frac{dQ_1}{dt}$) succeeds in attenuating the blast front when compared to the original GSD model, the first-order complete GSD model predicts a much weaker blast at distance.

To investigate if solving a higher-order complete GSD model leads to a better accuracy, equation (2.63) is revisited. By explicitly computing the post-shock flow term, $\partial_t p + \rho a \partial_t u$, through the similitude relation $d_x M(M)$ obtained from the analytical solution, the so-called **modified GSD model** [3] comprised of equations (2.71) and (2.72) is considered to have preserved the full completeness without truncation at any level of Q_k. The resulting blast behavior excellently recovers the analytical solution as shown in Figure 2.4. This agrees with our expectation considering that the modified GSD model should be able to correctly and sufficiently account for the post-shock flow effect by fully expressing the post-shock flow term.

$$\frac{d\boldsymbol{x}}{dt} = a_0 M \boldsymbol{n}, \tag{2.71}$$

$$\frac{dM}{dt} = \frac{-a_0 M}{d_M p + \rho a d_M u}\left[\left(\frac{\rho u a^2}{u+a}\right)\frac{A'}{A} + \left(\frac{1}{u+a} - \frac{1}{a_0 M}\right)\left(\frac{\partial p}{\partial t} + \rho a \frac{\partial u}{\partial t}\right)\right]. \tag{2.72}$$

The influence of the completeness of the post-shock flow term is best illustrated in Figure 2.5, where the values of $\frac{a_0 M}{d_M p + \rho a d_M u}\left(\frac{\rho u a^2}{u+a}\right)\frac{A'}{A}$ and $\frac{a_0 M}{d_M p + \rho a d_M u}\left(\frac{1}{u+a} - \frac{1}{a_0 M}\right)\left(\frac{\partial p}{\partial t} + \rho a \frac{\partial u}{\partial t}\right)$ that represent the geometrical effect and the post-shock flow effect respectively are tracked throughout the Lagrangian simulation. Since the opposite of these two terms make up the blast acceleration, $\frac{dM}{dt}$ as in equation (2.72), a positive value signals its effect in attenuating the blast front. In light of the fact that the geometrical effects obtained from solving the first-order complete GSD model and from the modified GSD model do not deviate much from each other as seen in Figure 2.4, the change of area upon the blast front should not be the reason for the discrepancy manifested in the blast behaviors for these two models. On the other hand, starting at the same initial value the post-shock flow effect from the

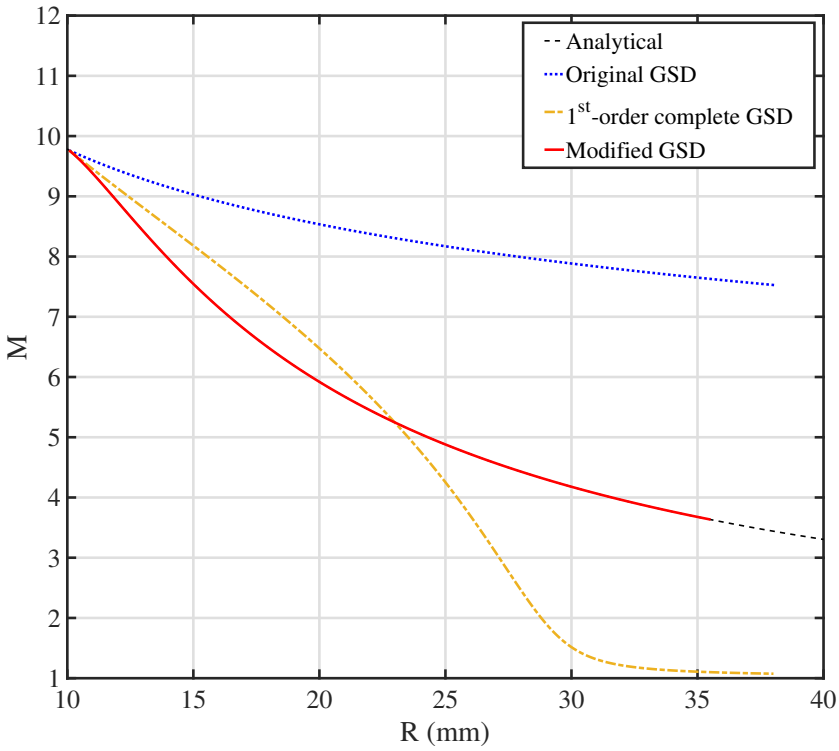

Figure 2.4: $M - R$ plots of the propagation of a single cylindrical blast in air for different GSD models. Initial conditions: $E_0 = 8,000$ J/m for the analytical solution; $R_0 = 10.06$ mm and $M_0 = 9.76$ for the GSD, 1^{st}-order complete GSD and modified GSD solutions.

modified GSD model soon departs from the first-order complete GSD result on its way to the peak value. Then the curve gradually slides and falls below its counterpart at $R \approx 17$ mm. Such observation of the post-shock flow effects at an early stage is echoed in the $M - R$ curves where the modified GSD model attenuates the blast front as accurately as the analytical solution suggests, while the first-order complete GSD model predicts a stronger blast. Later, as shown in Figure 2.5, the post-shock flow effect estimated by the first-order complete GSD model keeps increasing until arriving at its highest point at $R \approx 25$ mm, but its variance with the modified GSD result accumulates till the two curves intersect for the second time. This explains the over-attenuation of blast velocity

further away from the explosion center by the first-order complete GSD model as shown in Figure 2.4. Therefore, by comparing the post-shock flow effects from the two models and analyzing how their resulting blast behaviors differ accordingly, a conclusion can be made here that, the level of the completeness of the post-shock flow term determines the accuracy of geometrical shock dynamics when being applied to blast waves.

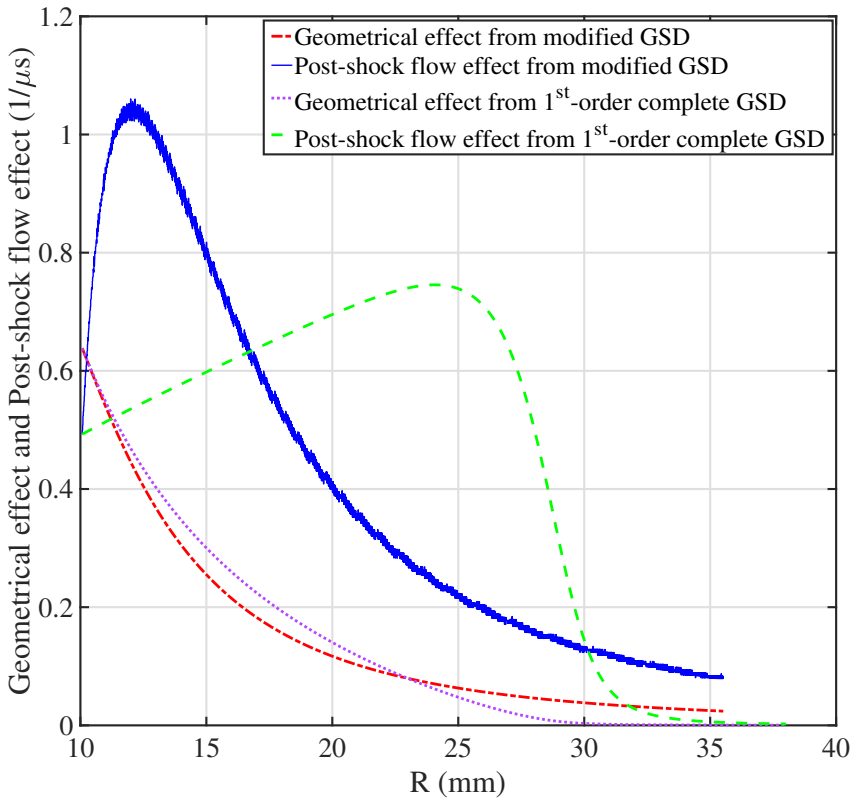

Figure 2.5: Variation of values involving the geometrical term and post-shock flow term as a function of blast radius. Initial conditions: $R_0 = 10.06$ mm and $M_0 = 9.76$ for the 1st-order complete GSD and modified GSD solutions.

2.6 Point-source GSD

The analytical solution to point-blast propagation and an improved GSD model based on it, referred to as point-source GSD, will be elaborated on in this section. Similar, but different than the classical self-similar solutions by Taylor [35] and Sedov [109] that are confined to the early stage of explosion when a blast front is still very strong, an approximate analytical method that is able to describe the entire propagation regime of a blast wave was proposed by Bach and Lee [105]. Such analytical solution was proved to be accurate even for weak blasts, which renders itself a perfect benchmark for the problems of blasts interacting at relatively low Mach numbers. The derivation of Bach and Lee's analytical solution is reviewed below.

Conservation equations of mass, momentum and energy for the unsteady one-dimensional adiabatic motion behind the blast wave are respectively written in a dimensionless form as follows

$$(\phi-\xi)\frac{\partial\psi}{\partial\xi}+\psi\frac{\partial\phi}{\partial\xi}+j\phi\frac{\psi}{\xi}=2\theta\eta\frac{\partial\psi}{\partial\eta}, \tag{2.73}$$

$$(\phi-\xi)\frac{\partial\phi}{\partial\xi}+\theta\phi+\frac{1}{\psi}\frac{\partial f}{\partial\xi}=2\theta\eta\frac{\partial\phi}{\partial\eta}, \tag{2.74}$$

$$(\phi-\xi)\left(\frac{\partial f}{\partial\xi}-\frac{\gamma f}{\psi}\frac{\partial\psi}{\partial\xi}\right)+2\theta f=2\theta\eta\left(\frac{\partial f}{\partial\eta}-\frac{\gamma f}{\psi}\frac{\partial\psi}{\partial\eta}\right), \tag{2.75}$$

where particle velocity profile ϕ, pressure profile f and density profile ψ are defined with respect to two dimensionless independent variables $\xi=\frac{r}{R_s(t)}$ and $\eta=\frac{c_0^2}{\dot{R}_s^2}=\frac{1}{M_s^2}$ as

$$\phi(\xi,\eta)=\frac{u(r,t)}{\dot{R}_s(t)}, \tag{2.76}$$

$$f(\xi,\eta)=\frac{p(r,t)}{\rho_0\dot{R}_s(t)^2}, \tag{2.77}$$

$$\psi(\xi,\eta)=\frac{\rho(r,t)}{\rho_0}, \tag{2.78}$$

and

$$\theta(\eta) = \frac{R_s \ddot{R}_s}{\dot{R}_s^2}. \tag{2.79}$$

Similar to Taylor's similarity law, ξ is the ratio between the radial coordinate measured from the explosion center and the instantaneous blast front radius, and η is a function of R_s. The numerical constant j that appears in the conservation equation of mass is defined as $j = 0, 1, 2$ for planar, cylindrical and spherical blast wave, respectively. The total energy enclosed by the blast wave should be conserved at all times and the energy integral is given as

$$y\left(\frac{I}{\eta} - \frac{1}{\gamma(\gamma-1)(j+1)}\right) = 1, \tag{2.80}$$

where

$$I = \int_0^1 \left(\frac{f}{\gamma-1} + \frac{\psi\phi^2}{2}\right)\xi^j d\xi, \tag{2.81}$$

$$y = \left(\frac{R_s}{R_0}\right)^{j+1}, \tag{2.82}$$

$$R_0 = \left(\frac{E}{\rho_0 a_0^2 k_j}\right)^{\frac{1}{j+1}}. \tag{2.83}$$

It is worth noting that R_0 is also called the characteristic explosion length, which is an intrinsic property of the explosion with total energy E. Also, $k_j = 1, 2\pi, 4\pi$ for $j = 0, 1, 2$, respectively.

According to the shock jump conditions, the boundary conditions should be satisfied

for variables at blast front $\xi = 1$ as follows:

$$\phi(1,\eta) = \frac{2(1-\eta)}{\gamma+1}, \tag{2.84}$$

$$f(1,\eta) = \frac{2}{\gamma+1} - \frac{(\gamma-1)\eta}{\gamma(\gamma+1)}, \tag{2.85}$$

$$\psi(1,\eta) = \frac{\gamma+1}{\gamma-1+2\eta}. \tag{2.86}$$

A hidden physical boundary condition must be satisfied at the origin of the explosion: $\phi(0,\eta) = 0$. This implies that the particle velocity should be zero at the center of symmetry. Now the mathematical formulation governing the flow field generated by the passage of a blast wave is complete. The solution to the energy integral (2.80) and conservation laws (2.73) – (2.75) satisfying boundary conditions (2.84) – (2.86) defines the dynamics of the blast wave and its flow structure at any instance of time.

Bach and Lee assumed a power-law density profile behind the blast wave

$$\psi(\xi,\eta) = \psi(1,\eta)\xi^{q(\eta)}, \tag{2.87}$$

where the exponent q can be determined by substituting the density profile into the integral of conservation of mass

$$q(\eta) = (j+1)[\psi(1,\eta) - 1]. \tag{2.88}$$

With the density profile known, equation (2.73) reduces to an ordinary linear differential equation of particle velocity profile $\phi(\xi,\eta)$. By satisfying the boundary condition $\phi(0,\eta) = 0$, the particle velocity profile takes the form

$$\phi(\xi,\eta) = \phi(1,\eta)\xi(1 - \Theta \ln \xi), \tag{2.89}$$

where

$$\Theta = \frac{-2\theta\eta}{\phi(1,\eta)\psi(1,\eta)}\frac{d\psi(1,\eta)}{d\eta}. \tag{2.90}$$

Finally, by substituting the density profile and particle velocity profile along with their partial derivatives with respect to ξ and η into the conservation of momentum, one can obtain the pressure profile after some algebraic manipulations

$$\begin{aligned} f(\xi,\eta) = f(1,\eta) + f_2(\xi^{q+2}-1) + f_3\{\xi^{q+2}[(q+2)\ln\xi - 1] + 1\} \\ + f_4\{2 - \xi^{q+2}[(q+2)^2\ln^2\xi - 2(q+2)\ln\xi + 2]\}, \end{aligned} \tag{2.91}$$

where

$$f_2 = \frac{\psi(1,\eta)}{q+2}\left\{(1-\Theta)\left[\phi(1,\eta) - \phi^2(1,\eta)\right] - \theta\left[\phi(1,\eta) - 2\eta\frac{d\phi(1,\eta)}{d\eta}\right]\right\}, \tag{2.92}$$

$$f_3 = \frac{\psi(1,\eta)}{(q+2)^2}\left\{\theta\left[\Theta\phi(1,\eta) - 2\eta\frac{d[\Theta\phi(1,\eta)]}{d\eta}\right] - \Theta\phi(1,\eta) - \Theta^2\phi^2(1,\eta) + 2\Theta\phi^2(1,\eta)\right\}, \tag{2.93}$$

$$f_4 = \Theta^2\phi^2(1,\eta)\frac{\psi(1,\eta)}{(q+2)^3}. \tag{2.94}$$

Here, q is given as in equation (2.88) and all the variables with $\xi = 1$ are evaluated at the blast front given in equations (2.84) – (2.86).

Since θ contained in the particle velocity and pressure profiles is yet unknown, in order to complete the solution the relationship between θ and η must be determined. By substituting all density, particle velocity and pressure profiles i.e., equations (2.87), (2.89) and (2.91) into the energy integral (2.80), one can solve for a differential form of the

relationship

$$\frac{d\theta(\eta)}{d\eta} = -\frac{1}{2\eta}\left\{\theta + 1 - 2\phi(1,\eta) - \frac{D+4\eta}{\gamma+1} - (\gamma-1)(j+1)\left[\phi(1,\eta) - \frac{(D+4\eta)^2}{4\theta y(\gamma+1)}\right]\right\} + \frac{D+4\eta}{8\eta^2(\gamma+1)}\left[\frac{(D+4\eta)\phi(1,\eta)}{\theta} - \frac{\phi(1,\eta)(\gamma+1)}{\theta\psi(1,\eta)} + 2(\eta+1) + (\gamma-1)(j+1)\frac{(\gamma+1)\phi^2(1,\eta)}{2\theta}\right] + \frac{2\theta[2+(\gamma-1)(j+1)]}{D+4\eta}, \quad (2.95)$$

where $D = \gamma(j+3) + (j-1)$.

Moreover, the relationship between the blast radius y and blast front velocity η is also found to be related to θ as

$$\frac{dy}{d\eta} = -\frac{(j+1)y}{2\theta\eta}. \quad (2.96)$$

Then, the solutions to the pair of ordinary differential equations (2.95) and (2.96) provide all the essential information about the propagation of a blast front including its instantaneous radius, velocity and acceleration. Functions $\theta(\eta)$ and $y(\eta)$ can be obtained simultaneously as the result of numerical integration (e.g. Runge-Kutta method) with the boundary condition satisfied at $\eta = 0$. The initial energy E only contributes to y through the characteristic explosion length R_0, while $\theta(\eta)$ acts as a scaling law that is independent of the energy of the explosion.

Recall that Whitham's original GSD model yields accurate results only when the flow behind the shock front is uniform such that the nonlinear geometrical effect becomes the dominant reason for the change of shock motion. However, for other cases where the shock front interacts strongly with the flow behind it, for example a blast wave, the resulting post-shock flow effect may become equally or even more influential than the geometrical effect so it should be taken into account in GSD. Considering Bach and Lee's analytical solution to point-blast propagation already encodes accurate blast behaviors,

a modification to the original GSD model to include such essential blast property was proposed by Yoo [110]. Rewrite equation (2.79) in the same manner as equation (2.38) using the equivalence $\dot{R}_s = a_0 M$ and $\ddot{R}_s = a_0 \frac{dM}{dt}$ to get

$$\frac{dM}{dt} = \frac{a_0 M^2 \theta}{R_s} = \frac{-a_0 M}{-j/M\theta} \frac{j}{R_s}. \tag{2.97}$$

In fact, $\frac{j}{R_s}$ is the curvature of a cylindrical ($j = 1$) and spherical ($j = 2$) blast, so $\frac{dM}{dt}$ can be further expressed as

$$\frac{dM}{dt} = \frac{-a_0 M}{\Phi(M)} \kappa, \tag{2.98}$$

where $\Phi(M) = -\frac{j}{M\theta}$ and $\theta(M)$ is given in equation (2.79) with the argument η replaced by $\frac{1}{M^2}$. Equation (2.98), which is the $\kappa - M$ relation particular for blast front, is effectively the core of the **point-source GSD (PGSD) model**. The main advantage of this model is that it defines the motion rule of blast propagation for all energy contents without the need to specify $\theta(\eta)$ for a particular point-source explosion. Moreover, the PGSD model can be further modified for condensed explosives as long as the resulting blast behavior is known beforehand. In this situation, the $M - R$ data is mostly used to generate $\Phi(M)$ that nonetheless encodes essential blast information only for that particular charge.

The same case was revisited here by solving the PGSD model with the Lagrangian scheme. The propagation of a cylindrical blast in air was simulated with initial conditions $M_0 = 9.76$ and $R_0 = 10.06$ mm. As shown in Figure 2.6, the resulting $M - R$ curve overlaps with the analytical solution as well as the modified GSD result, as expected.

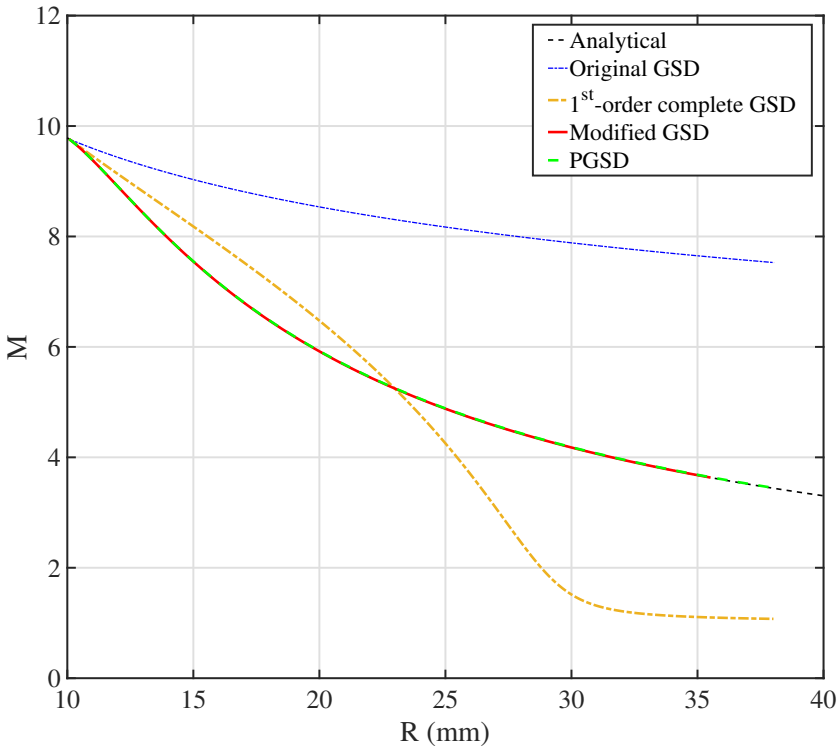

Figure 2.6: $M - R$ plots of the propagation of a single cylindrical blast in air for different GSD models. Initial conditions: $E_0 = 8,000$ J/m for the analytical solution; $R_0 = 10.06$ mm and $M_0 = 9.76$ for the GSD, 1st-order complete GSD, modified GSD and PGSD solutions.

2.7 $A - M$ Relation and $\kappa - M$ Relation

We are now in a good position to make additional comments about the equivalence of $\frac{A'}{A}$ to curvature κ, which has already been proved for the case of a two-dimensional diverging shock as in equation (2.36). A generalization of such equivalence is evident in partial differential equation (2.30) that can be rewritten as

$$\nabla \cdot \boldsymbol{n} - \frac{\boldsymbol{n} \cdot \nabla A}{A} = 0. \tag{2.99}$$

The equivalence

$$\frac{\boldsymbol{n}\cdot\nabla A}{A} = \frac{1}{A}\frac{dA}{dn} = \frac{A'}{A} \tag{2.100}$$

leads to

$$\frac{A'}{A} = \nabla\cdot\boldsymbol{n}. \tag{2.101}$$

In fact, the divergence of the unit surface normal is an alternative definition of curvature [111]. To prove this, first consider a two-dimensional implicit surface $\alpha(\boldsymbol{x})$ as defined in equation (2.28). Substituting $\boldsymbol{n} = \frac{\nabla\alpha}{\|\nabla\alpha\|}$ into the right hand side of equation (2.101) gives

$$\begin{aligned}\nabla\cdot\boldsymbol{n} &= \nabla\cdot\frac{\nabla\alpha}{\|\nabla\alpha\|}\\ &= (\alpha_x^2\alpha_{yy} - 2\alpha_x\alpha_y\alpha_{xy} + \alpha_y^2\alpha_{xx})/\|\nabla\alpha\|^3\\ &= \kappa,\end{aligned} \tag{2.102}$$

and it has the same properties as claimed by Best [94]: $\kappa > 0$ for convex regions, $\kappa < 0$ for concave regions, and $\kappa = 0$ for a plane shock.

Furthermore, for the case of shock surface propagation in three dimensions $\frac{A'}{A}$ is still related to the curvature, but strictly speaking, it is the sum of two principal curvatures as shown in equation (2.103)

$$\begin{aligned}\frac{A'}{A} &= \nabla\cdot\frac{\nabla\alpha}{\|\nabla\alpha\|}\\ &= (\alpha_x^2\alpha_{yy} - 2\alpha_x\alpha_y\alpha_{xy} + \alpha_y^2\alpha_{xx} + \alpha_x^2\alpha_{zz} - 2\alpha_x\alpha_z\alpha_{xz} + \alpha_z^2\alpha_{xx}\\ &+ \alpha_z^2\alpha_{yy} - 2\alpha_y\alpha_z\alpha_{yz} + \alpha_y^2\alpha_{zz})/\|\nabla\alpha\|^3\\ &= 2K_M,\end{aligned} \tag{2.103}$$

where the mean curvature K_M is half the sum of the two principal curvatures.

Therefore, the $A - M$ relation, equation (2.25), that describes how the shock front strength varies with the area upon it can now be replaced by the $\kappa - M$ relation, i.e.,

$$\frac{dM}{dt} = \frac{-a_0 M}{g(M)}\kappa, \tag{2.104}$$

where $g(M)$ is given in equation (2.22), and for a shock surface in three dimensions the sum of two principal curvatures is written in the form of κ for consistency.

The $\kappa - M$ relation represents the rate of change of the shock front Mach number subject to the local curvature, so it can be numerically integrated without needing the reference values A_0 and M_0 as in equation (2.26). Moreover, given that it is always cumbersome to define ray tubes and compute the cross section areas, another advantage of replacing the $A - M$ relation with the $\kappa - M$ relation is that unlike ray tubes that only exist virtually, curvature is clearly defined using differential geometry. This feature is also inherent to the PGSD model, especially when it is used to deal with a blast surface in three dimensions.

2.8 Application of PGSD to Blast Focusing Problems

The framework with the Lagrangian scheme solving the PGSD model used in this section for symmetric blast interaction problems is summarized next:

Step 1 – Find the transition conditions:

The critical conditions for the transition from regular to irregular reflection taking place where two neighboring blasts intersect should be first determined. If prior knowledge is accessible, the instantaneous Mach number and position of the shock front can be obtained through processing experimental schlieren images or from Euler

simulations. Various theoretical analyses also exist for computing the transition conditions and they are reviewed in detail in Section 1.2.2.

Step 2 – Generate initial input for the Lagrangian scheme:

The multi-blast front that is considered as a continuous curve seen in two-dimensional space is discretized by particles. Given a perfect circular shape is well preserved before any Mach stem arises, it is rational to assume that the velocity is evenly distributed along the shock front. Therefore, the Mach number at the transition instant and the instantaneous coordinates are stored at each particle as the initial input for the Lagrangian scheme.

Step 3 – Compute the irregular reflection phase through PGSD:

Once the frequency to apply mesh smoothing and regularization procedures is determined based on the shock front configuration and initial particle resolution, the Lagrangian scheme is started to take over the following computation for the irregular reflection phase. All the time steps registered in the scheme count from the transition instant.

Step 4 – Post-process data:

Only information about the shock front position and velocity is returned from the PGSD scheme once finished. Though the shock jump conditions can be used to derive the pressure, density and particle velocity in the flow immediately behind the shock front from the Mach number, accuracy is greatly in doubt if they are applied to the Mach stem with a very limited volume inside which energy is extremely condensed.

To evaluate the PGSD model as well as the application of geometrical shock dynamics to blast focusing problems, a symmetric interaction of a pair of cylindrical weak blast waves were simulated following the framework introduced above. This study is compared

to Higashino's experiments [2] in which two identical cylindrical blast waves were generated simultaneously by exploding two wires of the same size and material as illustrated in Figure 2.7. In the experiment, the exploding wires, made of either copper or nichrome, were 34 mm in length and 0.1 mm in diameter. The wires were placed 60 mm apart and exploded by an electrical discharge from capacitors that delivered energy of 25 J and 170 J for copper and nichrome wires, respectively. The same experiments were also numerically replicated by Qiu [3] using the modified GSD model. Due to uncertainties in the actual energy release in the wire explosions including incomplete detonation of the full length of wires and fractional usage of energy in explosions out of the total release from capacitors, a number of Euler simulations at different energy levels were first performed by Qiu in the hope of determining the actual energy release in explosions such that experimental results can be best reproduced. As a result, 117.09 J/m and 58.54 J/m of energy density were used to generate cylindrical point-blasts for Qiu's Lagrangian simulations for the copper and nichrome case, respectively.

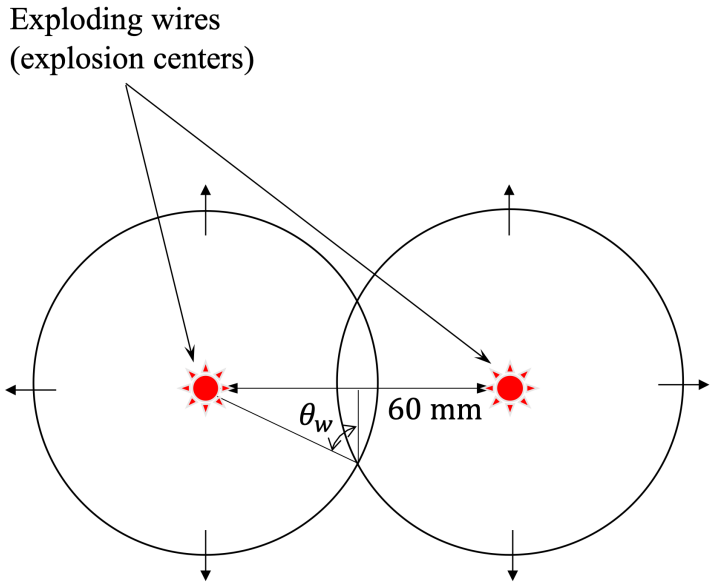

Figure 2.7: Schematic illustration of the experiments of Higashino *et al.* [2]. θ_w: wedge angle.

An approach to compute the transition conditions from regular to irregular reflection for the interaction between two identical cylindrical shocks was also introduced by Qiu [3]. It is done by communicating the shock motion known beforehand to the sonic criterion [62] via the wedge angle. Following this method the initial conditions for the PGSD scheme can be obtained with the energy density given above. An initial Mach number of 1.13 at an initial radius of 46.60 mm for the copper case, and an initial Mach number of 1.30 at an initial radius of 41.46 mm for the nichrome case turned out to be the instantaneous conditions when Mach stems are about to form during the interaction. The initial two-blast front was discretized with five particles per degree, i.e., a space step, $\Delta s \approx 0.2$ mm for the copper wire explosion and $\Delta s \approx 0.18$ mm for the nichrome wire explosion. Mesh smoothing and regularization procedures were implemented every few iterations such that particles in compressive regions would not travel across each other, while in the meantime the resolution could be well maintained in expansive regions.

Time history of the maximum pressure at the Mach stem was recorded in the PGSD Lagrangian scheme and compared to the modified GSD results as shown in Figure 2.8. Uncertainties exist in data that may pollute the time history of pressure by shifting the curves horizontally. This arises from the inconsistency between the transition time instant defined in Qiu's numerical study and that defined in this work. Since time registered in a Lagrangian simulation counts from the transition time instant, different definitions of such reference for the same explosion case would make the comparison between the two models less reliable. Consequently, it was carefully chosen for the current Lagrangian simulation by checking the corresponding Euler simulation using the initial energy density mentioned above.

Figure 2.8 suggests that the two models' solutions to the same explosion case agree in trend but differ in pressure values at the same time instance. Obviously, the maximum pressure curves from the PGSD model always lie above the modified GSD results for both

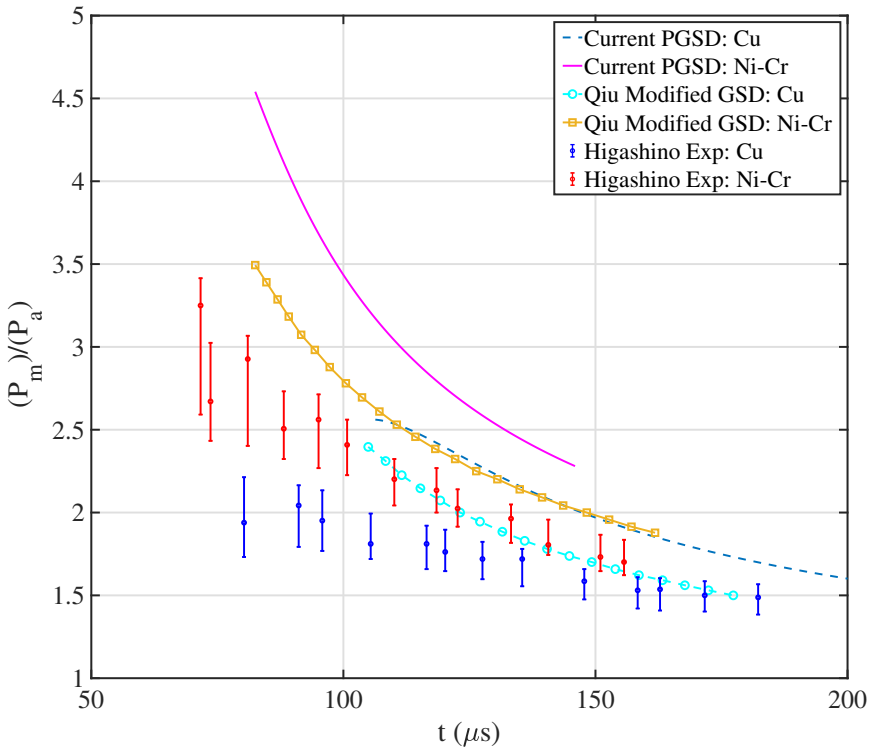

Figure 2.8: Ratio of maximum pressure at the Mach stem, P_m, to ambient pressure, P_a, as a function of time. Modified GSD data reproduced from [3] providing initial conditions to the current PGSD simulations. Experimental data reproduced from [2] with permission from Springer.

cases. Such discrepancy may come from differences in the reference time, or even from distinct intrinsic properties of the two models in terms of how the post-shock flow effect is dealt with. In fact, according to [3] two similitude relations were generated for the modified GSD model for each explosion case. One stems from the analytical solution and accounts for the propagation of the expansive part of the two-blast front, so the resulting shock behavior far away from the Mach stems should be in a good agreement with the PGSD model. The second similitude relation governs the growth of the Mach stems. It is obtained from the Euler simulations and applied to the particles on the Mach stems in the scheme. In this way the interaction between the Mach stem and nonlinear flows behind is considered

by the modified GSD model, which is possibly at a different level of intensity compared to the post-shock flow effect for a point-blast. This may be true as the result of complex flow field near the Mach stems, especially in the neighborhood of triples points those are responsible for the maximum pressure at an early stage of irregular reflection.

Theoretically and proved by the comparison, the main advantage of the PGSD model over the modified GSD model in solving blast dynamics problems lies in its efficiency. Though the latter is faster than the Euler simulation due to being a reduced-order model, it needs information beforehand about the blast behavior of a particular energy size, which can be cumbersome to obtain. If the irregular reflection that occurs where two blasts meet is of interest as well, one has to get access to the Euler solution to the same problem to generate the second similitude relation, so the availability of the model is lowered. In contrast, the PGSD model relies on $\theta(\eta)$ from the analytical solution [105] to account for the post-shock flow effect. Since $\theta(\eta)$ is indifferent to the energy of the point-source explosion, it only needs to be solved once and then can be used for any blast dynamics problems. Consequently, despite being short of information about Mach stem generation, the PGSD model preserves its speed to the fullest extent while only slightly compromising the accuracy in limited situations. For each case of the copper and nichrome wire explosions, the Lagrangian simulation took less than one minute on a single core of Intel Core(TM) i7-8750H CPU operating at 2.20 GHz with 32 GB memory, whereas an Euler simulation needed more than 48 hours with two cores of Intel Core(TM) i7-3930K CPU operating at 3.20 GHz with 16 GB memory.

This section will be closed by comparing the PGSD results to the experimental data using the initial conditions provided in Higashino *et al.*'s work. The main difficulty to make an appropriate comparison is still how to define the transition time that is used as the reference for the PGSD model. In the experiments, uncertainties not only came from image processing based on which the transition instant was determined, but also lay in the

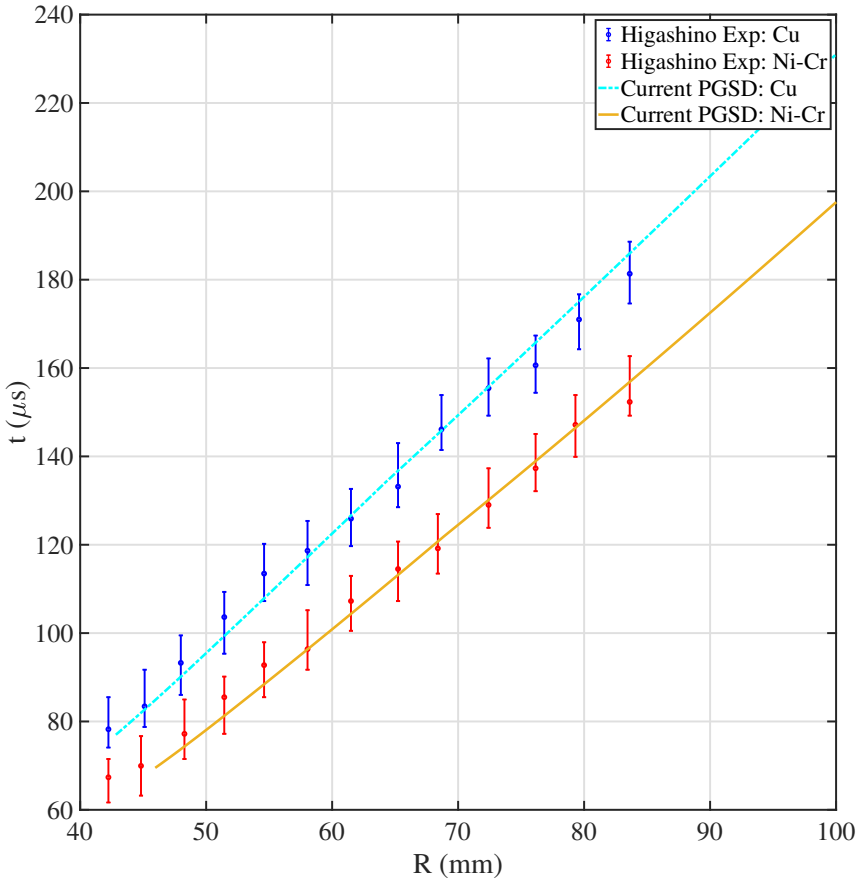

Figure 2.9: Arrival time of the shock front as a function of the radius reached. Experimental data reproduced from [2] with permission from Springer providing initial conditions to the current PGSD simulations.

time difference between the actual on-site of the wire explosion and when its luminosity was detected by photo-cells. Therefore, the time instants recorded in the experimental schlieren photographs should be treated with caution. In fact, the transition conditions measured in the experiments were given in Table 1 in [2] along with those predicted by von Neumann's detachment theory [60]. To avoid uncertainties in the measured data, the analysis of von Neumann was selected to generate the initial conditions for the PGSD scheme. By matching the arrival time of the undisturbed part of the shock front in a

least squares sense, as illustrated in Figure 2.9, the timeline of the Lagrangian simulation is consistent with that of the corresponding experiment. This makes the time history of the maximum pressure at the Mach front from the PGSD model comparable to the experimental data.

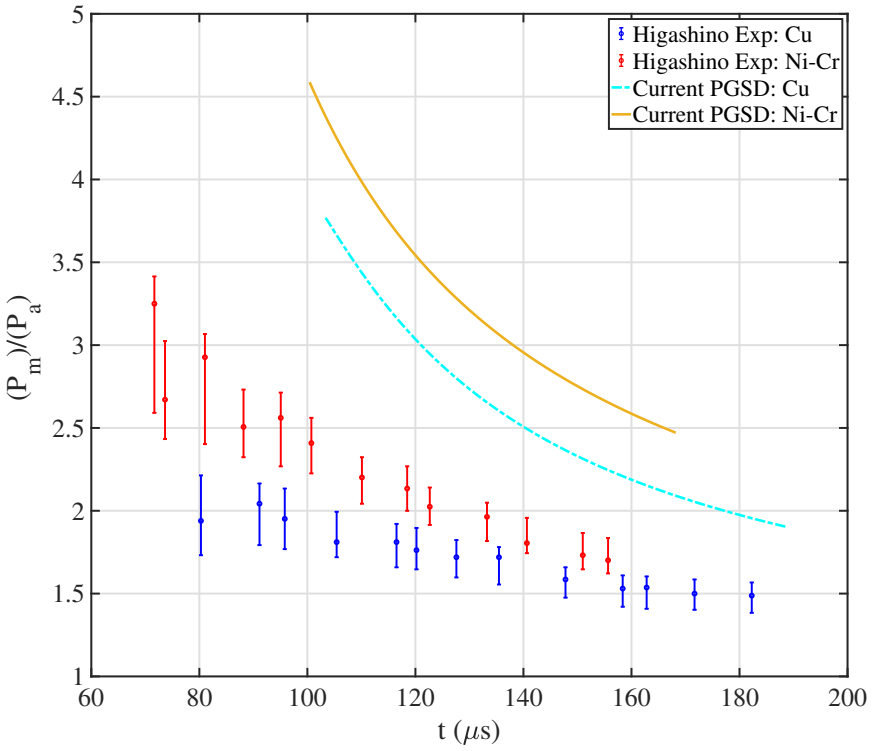

Figure 2.10: Ratio of maximum pressure at the Mach stem, P_m, to ambient pressure, P_a, as a function of time. Experimental data reproduced from [2] with permission from Springer providing initial conditions to the current PGSD simulations.

Figure 2.10 presents the results from the PGSD scheme with the same discretization rule introduced above, i.e., $\Delta s \approx 0.15$ mm for the copper wire explosion and $\Delta s \approx 0.16$ mm for the nichrome wire explosion. The mostly noticeable difference to the experimental data is that the PGSD's pressure value is higher than its counterpart at the same time instance for each case. This means that a much faster Mach stem is predicted by the PGSD model, in agreement with the observations in [3, 96]. Considering that geometrical shock

dynamics always tends to generate irregular reflection in compressive flows even when regular reflection is supposed to occur, the overestimation of Mach stem growth seems to be inevitable.

2.9 PGSD with the Shock-shock Approximate Theory – PGSDSS

One property of geometrical shock dynamics is its natural tendency to produce irregular reflection in compressive regions when regular reflection is expected. This is one of the reasons why the framework introduced in Section 2.8 directly starts the Lagrangian scheme at the transition instant from regular to irregular reflection for the problems of blast interaction. Another advantage of skipping the regular reflection phase is that it allows to construct the shock front in a more straightforward way. By using a continuous shock front to represent interacting blasts, the Lagrangian simulation avoids all difficulties in merging separated pieces if individual blasts were to be simulated at an early stage, primarily updating the connectivity information. In this sense, if an alternative framework with GSD is designed to solve blast focusing problems with initially separated blasts, it should be able to simulate the regular reflection that occurs between each pair of two neighboring ones. This is achieved by the model to be proposed in this section.

In fact, connectivity is not a one-time issue in terms of dealing with surface merging. Instead, it must be resolved over and over again every time any pair of blasts touches each other for the first time. In two-dimensional space, the task is manageable for some particular cases with simple geometry and one is symmetric interaction, so the interaction between multiple identical cylindrical blasts is aimed by this new model and the equivalence of every two-blast interaction to a blast impacting onto a reflecting wall further simplifies the problem. The blast is represented by a closed circle that evolves independently until it

touches the wall. Then, regular reflection is supposed to take place that features a perfect circular shape in the undisturbed part of the shock front. This can be achieved by applying a transmissive-like boundary condition in the Lagrangian scheme. To be specific, at each time step during regular reflection, particles that go across the wall are removed and new particles may have to be added close enough to the wall as the new ends of the curve. This renders the shock front no longer a closed curve such that the interpolation given in equation (2.34) should be dealt with care to account for the possible unevenness of particle resolution at both ends, but the effort needed to update the connectivity information is minimal. The wedge angle θ_w is tracked throughout the simulation and such special treatment of the regular reflection phase terminates once the pre-defined critical wedge angle is reached, i.e., $\theta_w = \theta_{wc}$.

To address the issue of overestimating Mach reflection by the PGSD model, the $\kappa - M$ relation is replaced by the shock-shock approximate theory to govern Mach stem growth in the new model. Whitham once applied the general theory of geometrical shock dynamics to the problem of diffraction of a plane shock by a concave corner and obtained the analytical solution to the trajectory of triple points (shock-shocks) [40]. Among all corner geometries Whitham considered, the shock-shock approximate theory for plane shock diffraction by a straight wedge as shown in Figure 2.11 becomes the inspiration for the current analysis of irregular reflection generated by a cylindrical shock impacting onto a reflecting wall. When a Mach stem is already formed, the shock front is separated by the triple point into two regions in which the Mach number is constant: M_0 for the undisturbed part and M_w for the Mach stem. The angle χ is the deflection angle between the triple point trajectory and the wedge reflecting surface tilted at θ_w above the ground. If a straight Mach stem is assumed, the undisturbed rays contained in a stream tube of

area $A_0 = \overline{AB'}\sin(\chi + \theta_w)$ pass through the area $A_w = \overline{AB'}\sin(\chi)$, so a relationship

$$\frac{f(M_w)}{f(M_0)} = \frac{\sin(\chi)}{\sin(\chi + \theta_w)} \tag{2.105}$$

can be obtained by using the $A - M$ relation to connect ray tube area and Mach number. Since the shock front is continuous at the triple point, the distance traveled by the triple point as part of the undisturbed shock should be the same as that being one end of the Mach stem, i.e., $\overline{AB'} = a_0 M_0 t/\cos(\chi + \theta_w) = a_0 M_w t/\cos(\chi)$. This leads to the relationship between the two Mach numbers

$$\frac{M_w}{M_0} = \frac{\cos(\chi)}{\cos(\chi + \theta_w)}. \tag{2.106}$$

Given the Mach number of the plane incident shock M_0 and wedge angle θ_w, the system consisting of equations (2.105) and (2.106) provides the solutions to χ and M_w. In this shock-shock approximate theory, nothing more than the trajectory of the triple point is yielded that is described by a single variable χ.

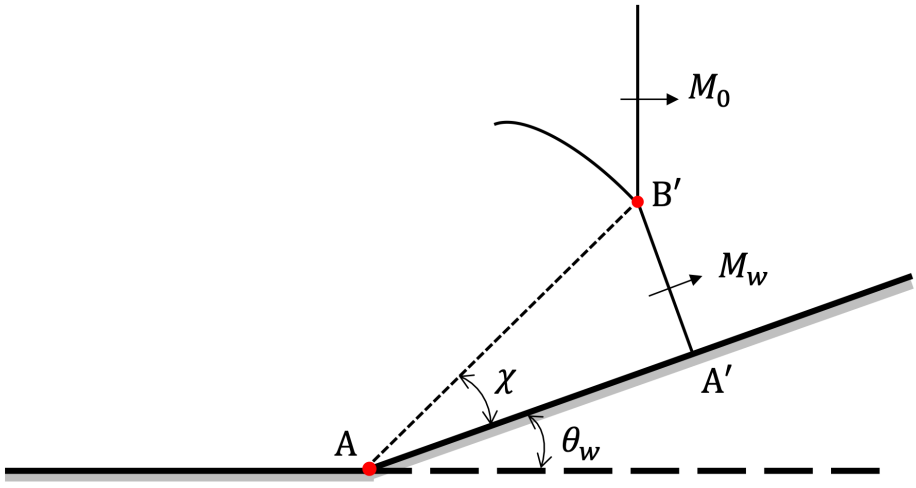

Figure 2.11: Schematic illustration of the diffraction of a plane shock by a straight wedge. Triple points represented by red dots.

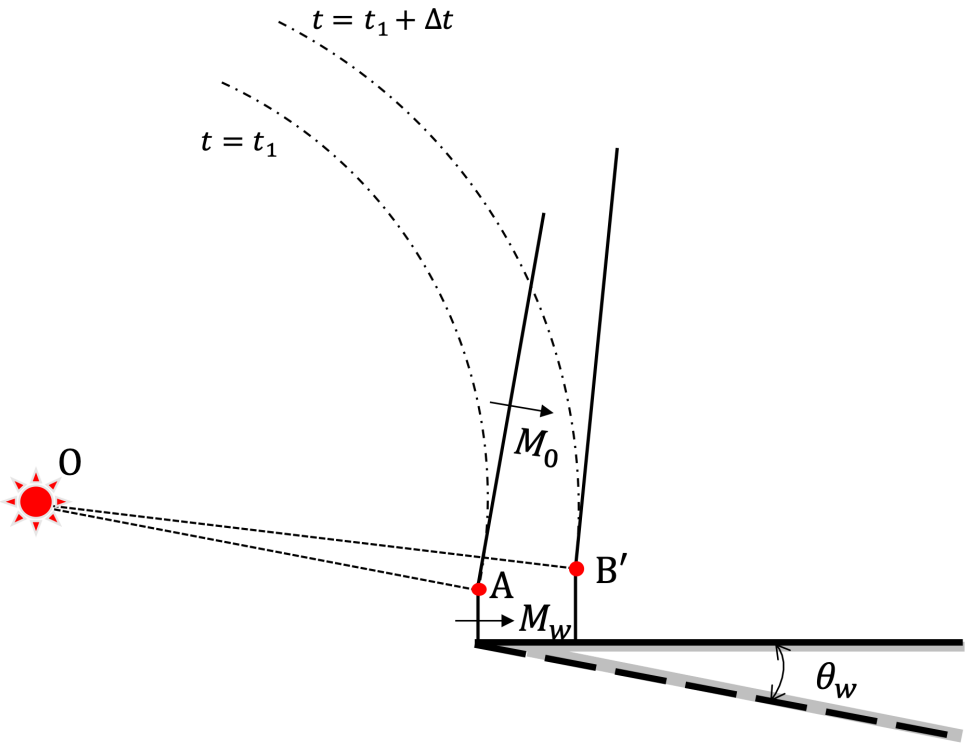

Figure 2.12: Schematic illustration of the treatment of cylindrical shock reflection off a straight surface as the diffraction of a plane shock by a straight wedge. Triple points represented by red dots.

When cylindrical shock reflection off a straight surface is considered, it is equivalent to the diffraction of a cylindrical shock by a straight wedge with continuously decreasing tilt angle. One difficulty remains and that is how to adapt the theory above to a curved incident shock. The most straightforward way is to simply treat the incident shock as a plane shock in the three-shock configuration as indicated in Figure 2.12. Once the transition angle θ_{wc} is reached, the Mach stem arises from the reflecting surface, assumably in a perpendicular manner. Then solve equations (2.105) and (2.106) with θ_w being the instantaneous wedge angle and M_0 being the Mach number for the expanding cylindrical shock. The resulting deflection angle, χ, and Mach number at wall, M_w, together give the location of the triple point after an infinitesimal period of time Δt, i.e., $B' = (x_A + M_w a_0 \Delta t, y_A + \tan(\chi) M_w a_0 \Delta t)$. However, B′ is not guaranteed to be on the undisturbed part of the shock front as there is

no constraint on the radial position of the triple point in equations (2.105) – (2.106).

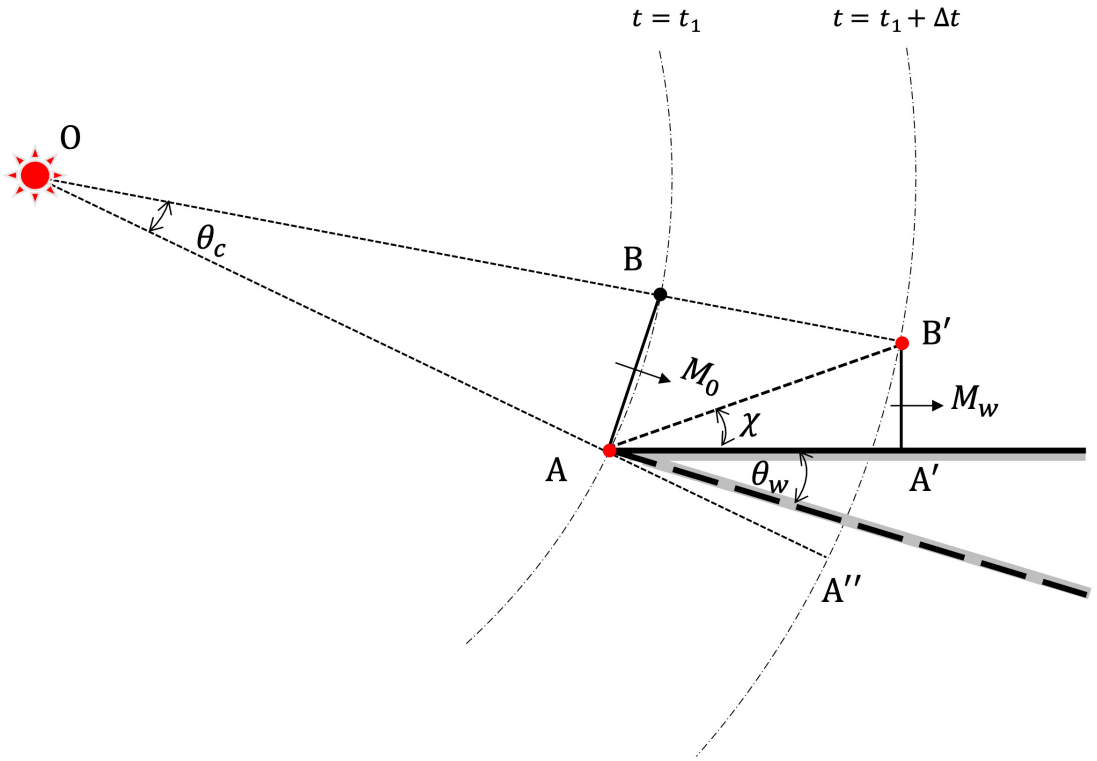

Figure 2.13: Schematic illustration of the diffraction of a cylindrical shock by a straight surface. Triple points represented by red dots.

In contrast, the circular geometry of the undisturbed part of the shock front is communicated to the triple point in an improved theory as presented in Figure 2.13. Here A is still the current location of the triple point but the cylindrical incident shock is no longer simplified as a plane shock. Instead, a curved shock element is considered as the incident shock in the three-shock configuration and its curved shape is preserved in developing the theory except when computing its ray area. This makes sense because in the Lagrangian scheme introduce in Section 2.3, the arc-length between two neighbor particles is approximated as a straight line in the calculation of the $A - M$ relation. The other end of the cylindrical shock element, point B, will become the triple point located at B′ after an infinitesimal time interval, but its current position is unknown. As a result, the

instantaneous wedge angle θ_w is also unknown considering that the wedge bottom surface is always parallel to the propagation direction of the incident shock that nonetheless depends on the choice of B. In fact, θ_w is related to the location of B in the following way:

$$\begin{aligned}
&\angle A'AA'' + \angle B'AA' + \angle BAB' + \angle OAB = \pi, \\
\longrightarrow\ &\angle A'AA'' + \chi + \frac{\pi}{2} - \chi - \theta_w + \frac{\pi - \theta_c}{2} = \pi, \\
&\longrightarrow \theta_w = \angle A'AA'' - \frac{\theta_c}{2},
\end{aligned}$$

where point O is the explosion center that is given in the initial conditions, and θ_c is the central angle of the minor arc between points A and B.

Similar to the shock-shock approximate theory for plane shock diffraction by a wedge, the relationship between Mach numbers M_w and M_0 is established by $\frac{M_w}{M_0} = \frac{\overline{AA'}}{\overline{BB'}}$. The law of sines further gives $\frac{\overline{AA'}}{\overline{BB'}} = \frac{\overline{AA'}/\overline{AB'}}{\overline{BB'}/\overline{AB'}} = \frac{\cos(\chi)}{\sin(\frac{\pi}{2} - \theta_w - \chi)/\sin(\frac{\pi}{2} + \frac{\theta_c}{2})}$, so

$$\frac{M_w}{M_0} = \frac{\cos(\chi)\cos(\frac{\theta_c}{2})}{\cos(\chi + \theta_w)}. \tag{2.107}$$

On the other hand, the undisturbed rays contained in a stream tube of area $A_0 = \overline{AB}$ passing through the area $A_w = \overline{A'B'}$ leads to

$$\frac{f(M_w)}{f(M_0)} = \frac{\sin(\chi)\sin(\frac{\pi}{2} + \frac{\theta_c}{2})}{\sin(\chi + \theta_w - \frac{\theta_c}{2})}. \tag{2.108}$$

The last piece of the new theory is a constraint that enforces the radial position of point B′ to be consistent with the radius of the undisturbed part of the shock front after an infinitesimal time span. This leads to another advantage of using a cylindrical shock as the

incident shock over the simplification of it into a plane one. It is given by

$$\|(x_A + M_w a_0 \Delta t, y_A + \tan(\chi) M_w a_0 \Delta t) - (x_O, y_O)\| = \overline{OB'}. \tag{2.109}$$

The shock-shock approximate theory for cylindrical shock reflection off a straight surface is thus complete. A system comprised of equations (2.107) – (2.109) along with the relation $\theta_w = \angle A'AA'' - \frac{\theta_c}{2}$ should be solved by a numerical algorithm with (x_A, y_A), θ_w and M_0 known at the current time step. The radius of the undisturbed part of the shock front at the next time step, $\overline{OB'}$, is not necessary to be determined at point B$'$ that is yet unknown; instead, the average radius can be used which is known after integrating the PGSD model for a time interval Δt. Moreover, equation (2.27), which only involves the geometrical effect, is used in (2.108). This is reasonable given that the triple point is always part of the undisturbed blast whose propagation is well described by the PGSD model, such that the motion of a Mach stem is independent of the post-shock flow effect by assuming a straight Mach stem. Consequently, the solutions to M_w, χ and θ_w in turn lead to the exact location of B$'$ at the next time step. All particles that traverse line segment A$'$B$'$ should be removed, which is considered to be the Mach stem.

Three processes, namely, individual blast expansion, a special treatment of regular reflection and the shock-shock approximate theory for cylindrical shock reflection off a reflecting surface for Mach reflection, together form the **PGSD with the shock-shock approximate theory (PGSDSS) model**. It is the essential part of an alternative framework for the symmetric interaction between initially separated blasts, along with the determination of the transition angle and data post-processing. To test the proposed PGSDSS model, the interaction between two identical cylindrical blasts located 20 mm from each other was numerically investigated. By taking advantage of symmetry, only one blast at a height of burst of 10 mm was actually simulated with the Lagrangian scheme

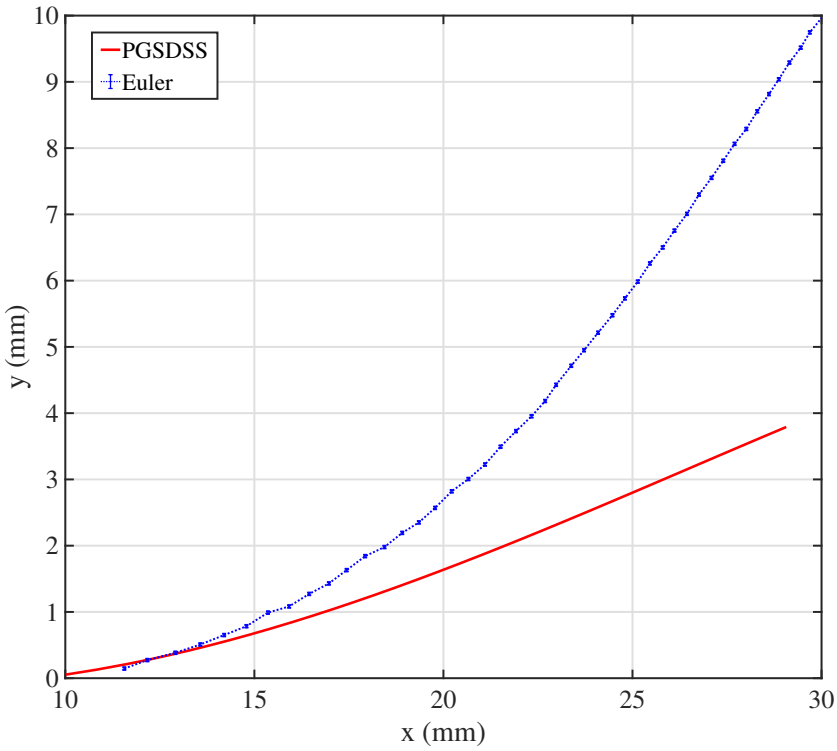

Figure 2.14: Comparison of the trajectory of the triple point for the interaction between two identical cylindrical blasts from the Euler and PGSDSS solutions. Initial conditions: $E_0 = 10,000$ J/m for the Euler solution; $R_0 = 5$ mm and $M_0 = 26.7$ for the PGSDSS solution.

solving the PGSDSS model. The initial conditions $R_0 = 5$ mm and M_0=26.7 were extracted from a two-dimensional Euler simulation with an initial energy density of 10,000 J/m for each point-explosion.

The triple point trajectory from the PGSDSS model with spacing $\Delta s \approx 0.08$ mm is compared to the Euler result as presented in Figure 2.14. As a result, opposite to the PGSD model, PGSDSS predicts a Mach stem that grows slower than the Euler simulation. Though uncertainties exist in the Euler result because the triple points were manually located at each time step by observing the sharp discontinues in flow properties, its size in each data point should not exceed the grid size $\Delta s = 0.04$ mm. Obviously, this is not

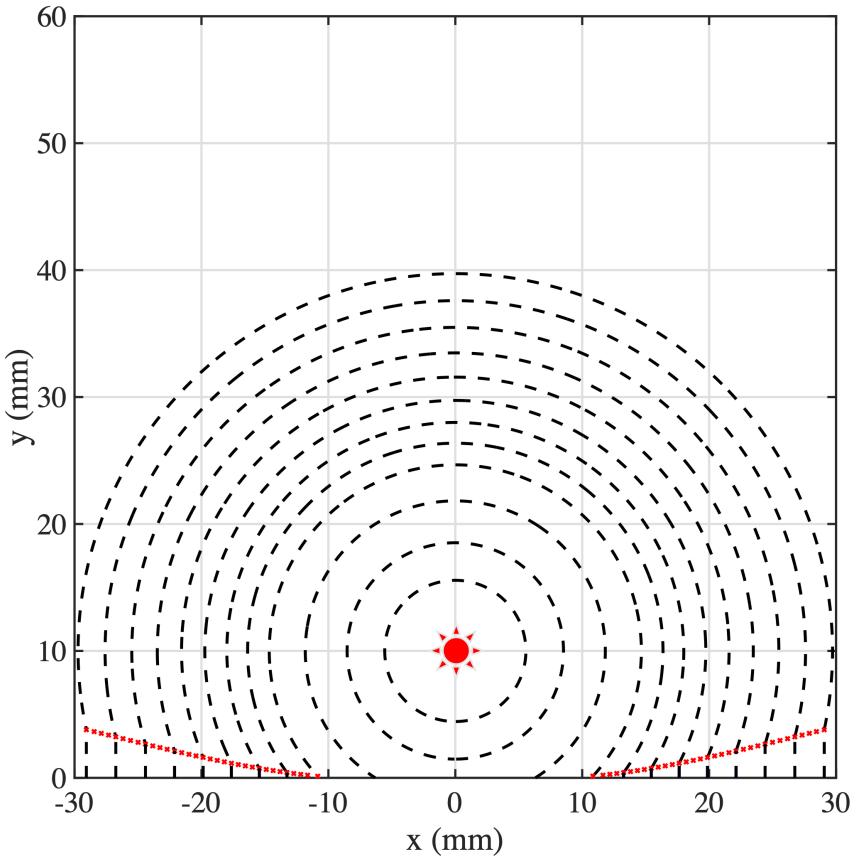

Figure 2.15: Evolution of the shock front formed by the interaction between two identical cylindrical blasts. Only half of the shock fronts shown with triple points represented by red dots. Initial conditions: $R_0 = 5$ mm and $M_0 = 26.7$ for the PGSDSS model.

sufficient to explain the discrepancy between the two trajectories of triple point further away from the explosion center. One primary contributor may be the assumption of a straight Mach stem made in the shock-shock approximate theory used in the PGSDSS model. In fact, as found in the Euler simulation, a curved Mach stem is more often seen to be generated from cylindrical shock reflection off a straight wall. This would result in a more significant curvature reverse at the triple point that accelerates its motion. Also, an even distribution of Mach number on the Mach stem is the result of trivial curvature but it

in turn suppresses the change of the Mach stem's shape. Figure 2.15 shows the shock front evolution with triple points marked independently. As expected, a perfect circular shape is excellently preserved in the undisturbed part of the shock front at each time step plotted. Though the PGSDSS model was used only to describe the symmetric interaction between two cylindrical blasts by exploiting its equivalence to one shock reflection off a straight wall, it has the potential to deal with multi-blast interaction as long as the axial symmetry can be established between every two neighboring blasts.

2.10 Chapter Summary

In this chapter, the general theory of geometrical shock dynamics (GSD) was first reviewed in detail. As the essential component of GSD, the $A - M$ relation was derived by substituting the shock jump conditions as a function of Mach number into the compatibility equation along the C_+ characteristics. It relates the change of area upon the shock front to shock motion with an assumption of a uniform state behind the shock. Numerical implementation of GSD is most often carried out by a front-tracking based Lagrangian scheme. It theoretically has an advantage over Euler simulations in efficiency as the result of GSD being a reduced-order model. Whitham's original GSD model [38, 39, 40] is able to achieve a good accuracy for the cases where geometrical effect is the dominant reason for shock motion, but falls short when being applied to blast waves where a strong gradient exists in the flow immediately behind the front. Such post-shock flow effect was recovered by Best [94] by integrating an infinite sequence of ordinary differential equations simultaneously. An arbitrary-order complete GSD model can then be achieved by truncating equations in the system but complexity increases considerably for every higher level of completeness. Hence, the first-order complete GSD model was solved, along with Qiu's modified GSD model [3], with the in-house Lagrangian codes for the problem of a single cylindrical blast

propagation in air. Compared to the modified GSD's result that excellently agrees with the analytical solution due to its ability to fully account for the post-shock flow effect, the first-order complete GSD model only shows limited improvement over the original GSD model. Such observation demonstrated the significance of the post-shock flow term's completeness in an accurate description of blast motion.

Then, the PGSD model [110] was introduced that encodes Bach and Lee's analytical solution to a point-blast. Unlike the modified GSD model that requires prior knowledge for a specific explosion, PGSD can be used for any energy content if the analytical solution is solved for once. This makes it an appropriate model for blast interaction problems since it well balances accuracy and speed. Therefore, based on the Lagrangian scheme that solves the PGSD model a framework was proposed to deal with symmetric blast focusing. By choosing to start the scheme at the transition instance from regular to irregular reflection that occurs between neighboring blasts, initial input can be generated with Mach number evenly distributed on the shock front. The PGSD model then takes over the computation for the subsequent Mach reflection phase, from which flow information immediately behind the moving front can be obtained through the shock jump conditions. Following the framework, Lagrangian simulations were performed aiming at numerically replicating Higashino *et al.*'s experiments of the two-blast interaction produced by exploding copper or nichrome wires simultaneously [2]. Though the simulation results have a similar trend in time history of the maximal pressure at the Mach stem with the experimental data, the PGSD model exhibits an obvious overshoot in both cases. This is believed to be caused by GSD's inherent tendency of overestimating the development of Mach reflection in compressive regions even when regular reflection is supposed to take place.

To overcome this issue, a new model was developed that treats regular and irregular reflection in different manners. The model is capable of being initialized with two separated blasts represented by two closed circles in two-dimensional space. Once the two curves

meet, regular reflection is realized by applying boundary conditions such that a perfect circular shape can be preserved near the intersections. Irregular reflection follows as soon as the pre-defined transition condition is reached. Mach stem growth is then governed by the shock-shock approximate theory for cylindrical shock reflection off a straight wall, while the undisturbed part of the shock front is still described by the PGSD model. The so-called PGSDSS model was evaluated by comparing the triple point trajectory to the Euler simulation for the interaction of two identical cylindrical blasts. As a result, the PGSDSS model yielded almost a straight line of trajectory in the xy-plane that lies lower than its counterpart all the time, which signals an underestimated Mach stem throughout its development. Such observation is just opposite to that from the PGSD model which instead overestimated the Mach stem growth, and one possible cause is the assumption of a straight Mach stem made in deriving the shock-shock approximate theory.

Chapter 2, in part is currently being prepared for submission for publication of the material. Heng, Liu; Veronica, Eliasson. The dissertation author was the primary investigator and author of this material.

Chapter 3

3D Point-source Geometrical Shock Dynamics

After three two-dimensional GSD models that account for the post-shock flow effect were investigated in Chapter 2, the PGSD model stood out due to its good accuracy for blast propagation and adaptation to any point-explosion initial energy. Moreover, as the result of replacing the $A - M$ relation with the $\kappa - M$ relation, another advantage of PGSD is its capability to be simplify extended to three dimensions. Therefore, the goal of this chapter is to develop a PGSD model suitable for three-dimensional shock dynamics problems; particularly, how to compute the differential geometric properties of the shock surface required by PGSD will be the focus. The choice of the parameters in the model as well as the trade-offs between accuracy and efficiency will also be discussed.

3.1 Point Cloud and Octree Data Structure

A point (particle) cloud is a natural choice to represent the shock front in three-dimensional space for GSD if it is chosen to be solved using a particle method. Assuming

a point cloud consisting of points $\mathcal{P} = \{\boldsymbol{p}_i\}$ in the Euclidean space $\mathbb{R}^3$ sampled from a shock front surface $\mathcal{S}$ at an arbitrary time instant, in general, a triangulated mesh can be formed whose vertices belong to $\mathcal{P}$. Connectivity information should be explicitly stored in some data structure that provides essential support for basic operations such as inserting and removing triangles when necessary. Thus, updating the connectivity information is necessary throughout the numerical simulation. However, it would cause significant inconvenience if regularization of triangulated surface needs to be frequently implemented, especially for the cases of multi-shock interaction where points become densely spaced in the neighborhood of triple points. In order to avoid errors arising from incorrectly updating mesh connectivity and to enable a fast k-nearest neighbor search, a point cloud is arranged in an octree date structure that only stores positional date without the need of the connectivity information.

Since being introduced by Meagher in the early 1980's [112], the octree data structure has been widely used to store large quantity of three-dimensional data and deal with positional queries. Octree as a spatial data structure is hierarchical in nature. It consists of nodes that occupy the volume formed by a rectangular cuboid. Each node has a chosen middle point, the geometric center of the body for example, that defines three planes that pass it while being parallel to the xy-, xz- and yz-planes, respectively. As a result, an inner octree node has eight children, each corresponds to an octant. In practice, starting at a root node that occupies the space containing the whole point cloud, a recursive subdivision procedure partitioning space into eight octants is performed until a stopping criterion is reached. In general, the criterion defines the minimum number of points and the maximum depth. The maximum depth indeed sets the lower bound to a node's size. If a node satisfies the stopping condition, a further subdivision is not necessary and the node becomes a leaf node sitting at the bottom level of the octree, otherwise the node is considered to be an internal node. In this way, all points in the cloud are assigned

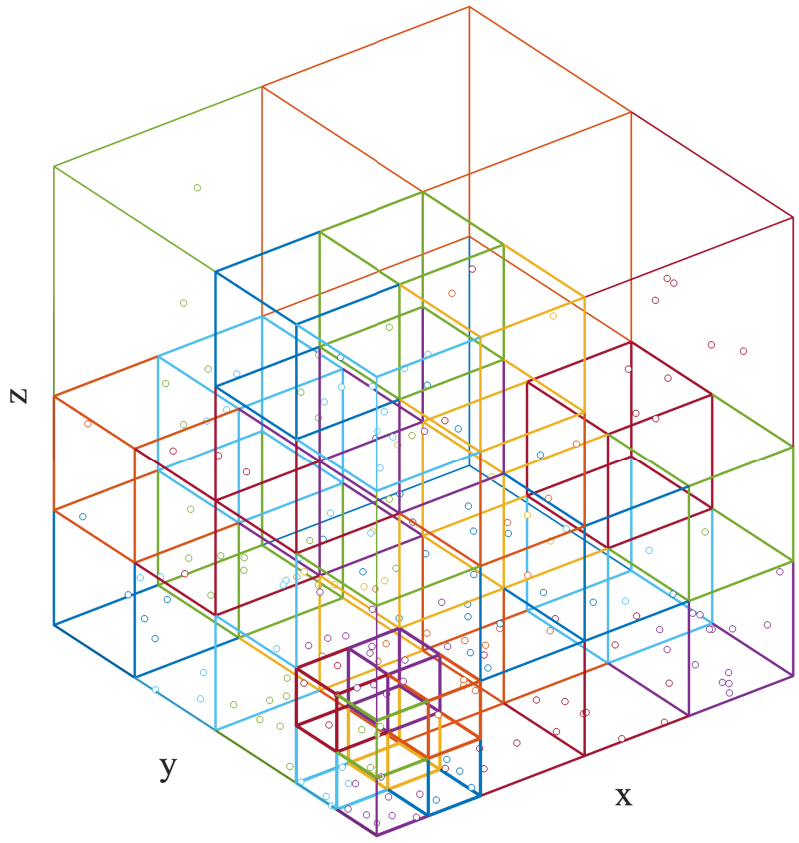

Figure 3.1: Schematic illustration of an octree data structure. Points (dots) and the occupied leaf node presented in the same color.

to leaf nodes as illustrated in Figure 3.1 and a list of points is stored in each occupied leaf. Since a point cloud that represents a shock surface in three dimensions is usually not fully volumetric, a large portion of space is not occupied by points. Thus most internal nodes only have few children without being empty and this makes the octree data structure ideally suitable for efficiently storing and retrieving positional data of a shock surface. A fast k-nearest neighbor search for a given point can be achieved by examining the neighbor nodes of the occupied leaf in a strategic way suggested by Behley *et al.* [113].

3.2 Moving Least Squares Surface

All surface approximation methods are based on the assumption that the given point cloud is a good representation of the underlying surface in a sense that it should be as small as possible while conveying sufficient essential shape information without noisy or redundant points. Among smooth approximate surfaces, the moving least squares (MLS) surface [114, 115, 116] is motivated by differential geometry and devised with an aim to minimize the error of the approximation. This is done by locally approximating the surface with polynomials in a weighted least squares sense.

The main idea of computing an MLS surface is the definition of a projection procedure that is able to project any point near the point cloud onto the same surface. Then, the MLS surface is such projection surface defined by the points that can be projected onto themselves.

3.2.1 MLS Projection Procedure

Assuming a point cloud $\mathcal{P} = \{\boldsymbol{p}_i \in \mathbb{R}^3\}$ is sampled from a surface $\mathcal{S}$, the goal of the MLS projection procedure is to project an arbitrary point $\boldsymbol{r} \in \mathbb{R}^3$ near the point cloud onto a two-dimensional manifold $\mathcal{S}_p$ that approximates $\mathcal{S}$. Two steps are involved to compute a projector locally.

Step 1 – Reference plane:

A local reference plane $\mathcal{H}$ for $\boldsymbol{r}$ is computed with the support of $\boldsymbol{r}'s$ k-nearest neighbors, $\boldsymbol{p}_i^{\boldsymbol{r}}$. The plane is defined by the plane normal, $\boldsymbol{n}_T$, and a point passed through, $\boldsymbol{q}$, as $\mathcal{H} = \{\boldsymbol{x} | \boldsymbol{n}_T \cdot (\boldsymbol{x} - \boldsymbol{q}) = 0\}$. $\boldsymbol{q}$ is the projection of $\boldsymbol{r}$ onto $\mathcal{H}$ and defined as $\boldsymbol{q} = \boldsymbol{r} + d\boldsymbol{n}_T$. Figure 3.2 illustrates this projection process but from a two-dimensional point of view for simplicity. The scalar variable d and vector variable $\boldsymbol{n}_T$ are computed via minimizing the local weighted sum of squared distance

between $\boldsymbol{p}_i^{\boldsymbol{r}}$ and $\mathcal{H}$

$$\sum_{i=1}^{k} \left[\boldsymbol{n}_T \cdot (\boldsymbol{p}_i^{\boldsymbol{r}} - \boldsymbol{q})\right]^2 \theta(\|\boldsymbol{p}_i^{\boldsymbol{r}} - \boldsymbol{q}\|), \tag{3.1}$$

where the weights attached to $\boldsymbol{p}_i^{\boldsymbol{r}}$ are defined by the weight function, $\theta(s)$, which is a smooth, positive but monotonically decreasing function in the whole domain of $\boldsymbol{x}$. A popular form of the weight function is a Gaussian, $\theta(s) = e^{-\frac{s^2}{h}}$, where h is a hyper-parameter that reflects the anticipated spacing between neighbor points free of sharp features. A smaller h causes the weight function to decay faster, which leads to a more local approximation and vice versa, such that h effectively serves as a measurement of feature size. By changing h the surface tends to smooth out all features of size smaller than h.

Step 2 – Local mapping:

The reference plane, $\mathcal{H}$, approximates the tangent plane to $\mathcal{S}$ near $\boldsymbol{r}$, and a local orthonormal coordinate system is set up on it. The origin of the local coordinate system is chosen to be located at $\boldsymbol{q}$, and one axis coincides with the reference plane normal, $\boldsymbol{n}_T$, which is known from step 1. Then a local polynomial approximation $g(x_i, y_i)$ to the heights z_i of $\boldsymbol{p}_i^{\boldsymbol{r}}$ over $\mathcal{H}$ is computed by minimizing

$$\sum_{i=1}^{k} \left[g(x_i, y_i) - z_i\right]^2 \theta(\|\boldsymbol{p}_i^{\boldsymbol{r}} - \boldsymbol{q}\|), \tag{3.2}$$

where (x_i, y_i) are the coordinates of the projection of $\boldsymbol{p}_i^{\boldsymbol{r}}$ onto the reference plane and $z_i = \boldsymbol{n}_T \cdot (\boldsymbol{p}_i^{\boldsymbol{r}} - \boldsymbol{q})$. Similar to minimizing function (3.1), this is another optimization problem that solves the coefficients of the bivariate polynomial $g(x, y)$ in a weighted least squares error sense. Then the projection of $\boldsymbol{r}$ onto $\mathcal{S}_p$ is defined by the polynomial value at the origin, $\boldsymbol{q} + g(0, 0)\boldsymbol{n}_T$, and it is part of the MLS

surface.

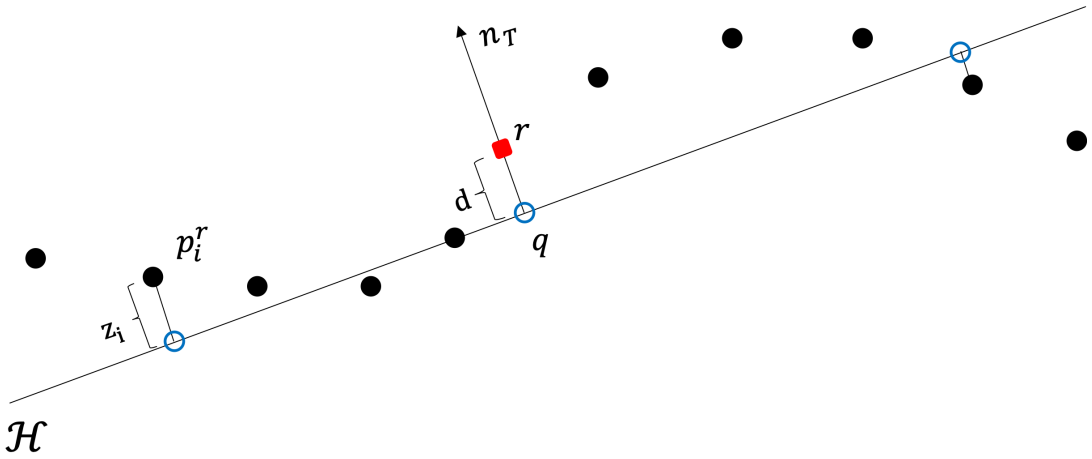

Figure 3.2: Schematic illustration of the MLS projection. $\boldsymbol{r}$: the point to be projected; $\mathcal{H}$: the reference plane defined by the normal, $\boldsymbol{n}_T$, and the projection, $\boldsymbol{q}$; $\boldsymbol{p}_i^{\boldsymbol{r}}$: the supporting neighbors of $\boldsymbol{r}$.

3.2.2 Computing the Projection

The first step of the MLS projection procedure is a nonlinear optimization problem with constraints. For function (3.1), there may be more than one local minimum near $\boldsymbol{r}$ given its k-nearest neighbors in the point cloud. Considering $\mathcal{S}_p$ approximates the underlying surface $\mathcal{S}$ represented by the point cloud, if $\boldsymbol{r}$ is close to $\mathcal{S}$, the resulting reference plane should be close to $\boldsymbol{r}$. In this sense, the least local minimum with a small absolute value of d should be chosen. Moreover, the key to the success of finding the least one among all local minimum heavily relies on the initial estimate of $\boldsymbol{n}_T$. Only if no sharp features nor high curvature regions exist in the neighborhood of $\boldsymbol{r}$, or no prior knowledge about $\boldsymbol{n}_T$ is provided, an iterative scheme should be adopted to find the initial value of $\boldsymbol{n}_T$ by minimizing function (3.1). First, the plane normal is solely solved by assuming $d = 0$. In this situation the weights $\theta_i = \theta(\|\boldsymbol{p}_i^{\boldsymbol{r}} - \boldsymbol{r}\|)$ are fixed, and function (3.1) becomes a quadratic

function in $\boldsymbol{n}_T = [n_1, n_2, n_3]$. To make sure $\boldsymbol{n}$ does not vanish, the constraint $\|\boldsymbol{n}_T\| = 1$ should always be satisfied. Then one can apply the method of Lagrange multipliers that converts the optimization problem into solving

$$\nabla_{n_1,n_2,n_3,\lambda} \mathcal{L}(n_1, n_2, n_3, \lambda) = \mathbf{0}, \tag{3.3}$$

where $\mathcal{L}(n_1, n_2, n_3, \lambda) = \sum_{i=1}^{k} \left[\boldsymbol{n}_T \cdot (\boldsymbol{p}_i^{\boldsymbol{r}} - \boldsymbol{r})\right]^2 \theta_i - \lambda(n_1^2 + n_2^2 + n_3^2 - 1)$.

In fact, the search for such a reference plane with $d = 0$ resembles principal component analysis (PCA). PCA can be seen as the result of projecting each data point onto the first few components to achieve dimension reduction while preserving as much of the variation in data as possible. In this specific case, all three dimensions are preserved if the point cloud's positional information is considered as features, and the direction that exhibits the least amount of variation is the plane normal. Then the minimization problem can be rewritten in a bilinear form

$$\min_{\|\boldsymbol{n}_T\|=1} \boldsymbol{n}_T^T B \boldsymbol{n}_T, \tag{3.4}$$

where the covariance matrix $B = \{b_{mn}\} \in \mathbb{R}^{3\times 3}$ is defined as

$$b_{mn} = \sum_{i=1}^{k} (p_{i_m}^r - r_m)(p_{i_n}^r - r_n)\ \theta_i. \tag{3.5}$$

The solution to the minimization problem (3.4) is given as the eigenvector of the covariance matrix that corresponds to the smallest absolute eigenvalue. Once $\boldsymbol{n}_T$ is computed, the next step is to minimize function (3.1) with respect to d. Since $\boldsymbol{n}_T$ is now fixed, this is a nonlinear optimization problem in one dimension. Considering d should have a small value, Alexa *et al.* [115] suggested to find d within the range of $[-\frac{h}{2}, \frac{h}{2}]$ where only one local minimum was found. Such constraint on h agrees with the intuition that

h is related to feature size in a way that smooths out the features of size smaller than h. Then d can be computed by evaluating the weighted least squares (3.6)

$$\min_{-\frac{h}{2}\leqslant d\leqslant\frac{h}{2}} \sum_{i=1}^{k} \left[\boldsymbol{n}_T \cdot (\boldsymbol{p}_i^{\boldsymbol{r}} - \boldsymbol{r} - d\boldsymbol{n}_T)\right]^2 \theta(\|\boldsymbol{p}_i^{\boldsymbol{r}} - \boldsymbol{r} - d\boldsymbol{n}_T\|). \tag{3.6}$$

Once $d \neq 0$ is returned, the iterative scheme shifts the focus to refine $\boldsymbol{n}_T$ by fixing d. Weights change with $\boldsymbol{n}_T$ if $d \neq 0$, so neither problem (3.3) nor (3.4) should be evaluated since they are for the case of fixed weights. Instead, the nonlinear minimization problem, (3.7), is solved

$$\min_{\|\boldsymbol{n}_T\|=1} \sum_{i=1}^{k} \left[\boldsymbol{n}_T \cdot (\boldsymbol{p}_i^{\boldsymbol{r}} - \boldsymbol{r} - d\boldsymbol{n}_T)\right]^2 \theta(\|\boldsymbol{p}_i^{\boldsymbol{r}} - \boldsymbol{r} - d\boldsymbol{n}_T\|). \tag{3.7}$$

To summarize, the framework of an iterative scheme that minimizes function (3.1) is listed as follows:

Initial guess of $\boldsymbol{n}_T$:

The success of finding the least one among all local minimum for function (3.1) heavily relies on the initial estimate of $\boldsymbol{n}_T$. It is possible that an initial guess is given as part of the input data in the form of surface normal. If no prior knowledge is provided, it can be computed by solving either optimization problem (3.3) or (3.4) for the regions free of sharp features and high curvature.

Iterative nonlinear minimization:

The following two steps are repeated until both $\boldsymbol{n}_T$ and d change no more than a pre-defined threshold:

1. Minimize along d that is bracketed in a range of $[-\frac{h}{2}, \frac{h}{2}]$ by solving the optimization problem (3.6).

2. Solve $\boldsymbol{n}_T$ by minimizing the weighted least squares error as in (3.7) subject to

$\|\boldsymbol{n}_T\| = 1$.

In fact, the search space of $\boldsymbol{n}_T$ can be visualized as tangent planes to a sphere centered at $\boldsymbol{r}$ with a radius of d. Alexa *et al.* [114] found that $\boldsymbol{n}_T$ only changes slightly for a fixed d, so they approximated the sphere locally in the neighborhood of $\boldsymbol{q}$ using the reference plane to be defined by $\boldsymbol{q}$ and $\boldsymbol{n}_T$. This simpler linear search space effectively changes $\boldsymbol{n}_T$ and d at the same time so makes the iterative scheme more efficient. However, the difference between the sphere search and the plane search was found to be small.

The second step of the MLS projection procedure is a standard linear least squares problem given $\theta_i = \theta(\|\boldsymbol{p}_i^{\boldsymbol{r}} - \boldsymbol{q}\|)$ is known once the reference plane is determined. The coefficients of the polynomial are solved by a system of linear equations of size equal to the number of coefficients. Usually, polynomials of degree three is used in all the following Lagrangian simulations.

3.3 Surface Normal and Curvature

The sign of curvature bears physical meaning as mentioned in Section 2.7 for two-dimensional GSD: a positive curvature is the result of convex regions and a negative curvature should be obtained where the shock front is concave. For a shock surface in three dimensions, curvature should be defined in a similar way. Considering κ represents the sum of two principal curvatures as in equation (2.98) and principal curvatures are simply the maximum and minimum values of the normal curvature, the definition of normal curvature should be revisited to guarantee a positive curvature anywhere on a diverging spherical shock.

Given a unit tangent vector $\boldsymbol{u}$ to surface $\mathcal{S}$ at $\boldsymbol{p}$, let α be an arc-length parameterized curve in $\mathcal{S}$ with initial velocity $\alpha'(0) = \boldsymbol{u}$, then the normal curvature of $\mathcal{S}$ in the $\boldsymbol{u}$ direction

can be computed by [117]

$$k(\boldsymbol{u}) = \alpha''(0) \cdot \boldsymbol{n}(\boldsymbol{p}) = \kappa(0)\boldsymbol{N}(0) \cdot \boldsymbol{n}(\boldsymbol{p}), \tag{3.8}$$

where $\boldsymbol{n}(\boldsymbol{p})$ is the surface normal at $\boldsymbol{p}$, and $\kappa(0)$, $\boldsymbol{N}(0)$ are respectively the absolute curvature value and the principal normal to the curve at $\kappa(0) = \boldsymbol{p}$. Seeing that principal normal, $\boldsymbol{N} = \frac{\boldsymbol{u}}{\|\boldsymbol{u}\|}$, is the one always pointing in the direction that the tangent plane is turning, the sign of a principal curvature indeed depends on the choice of the surface normal orientation. On a sphere any point is umbilic and the value of normal curvature is exactly the same anywhere, so only if the surface normal points inward the sum of the two principal curvatures is positive for a diverging spherical shock. However, this contradicts the GSD theory in which the surface normal is supposed to have the same orientation as the direction of propagation.

In practice, principal curvatures are not obtained from equation (3.8), instead they are computed through the first and second fundamental forms. In the second step of the MLS projection procedure, a bivariate polynomial $g(x_i, y_i)$ that approximates the heights z_i is solved in a local coordinate system by minimizing the sum of weighted squared errors. Therefore, an MLS surface patch can be expressed as a parametric surface $\boldsymbol{x}(u, v) = (u, v, g(u, v))$, and the first and second fundamental forms follow as below

$$E = \boldsymbol{x}_u \cdot \boldsymbol{x}_u, \quad F = \boldsymbol{x}_u \cdot \boldsymbol{x}_v, \quad G = \boldsymbol{x}_v \cdot \boldsymbol{x}_v; \tag{3.9}$$

$$L = \boldsymbol{x}_{uu} \cdot \boldsymbol{n}, \quad M = \boldsymbol{x}_{uv} \cdot \boldsymbol{n}, \quad N = \boldsymbol{x}_{vv} \cdot \boldsymbol{n}. \tag{3.10}$$

where $\boldsymbol{n}$ is the unit surface normal that can be constructed by

$$\boldsymbol{n} = \frac{\boldsymbol{x}_u \times \boldsymbol{x}_v}{\|\boldsymbol{x}_u \times \boldsymbol{x}_v\|}, \tag{3.11}$$

but its orientation is arbitrary. Then the mean curvature K_M is given by

$$K_M = \frac{GL + EN - 2FM}{2(EG - F^2)}. \tag{3.12}$$

The mean curvature computed this way still depends on the choice of the orientation of the surface normal, $\boldsymbol{n}$, as discussed earlier. To guarantee positive normal curvatures anywhere on a diverging spherical shock surface, the idea is to store the outward surface normals known at the current iteration as the reference for the next iteration. Then at each iteration the orientation of the surface normal to an MLS surface patch can be determined by comparing it to the reference stored at the same point. This is true only if the normal to the moving surface at each point does not vary much between iterations and this assumption is proved to be valid in practice. Once the surface normal is ensured to be pointing outward, according to equation (3.8) normal curvatures must be negative in all directions at any point on a sphere due to $\boldsymbol{N}(0) < 0$. Therefore, to accommodate for the curvature's definition in the $\kappa - M$ relation, i.e., equation (2.98), it is necessary to define κ specifically for a shock surface in three dimensions as

$$\kappa = -2K_M. \tag{3.13}$$

Though it is attractive to use the normal to the reference plane, $\boldsymbol{n}_T$, as the normal to the shock surface, $\boldsymbol{n}$, in the PGSD scheme, they are not the same in general. In comparison to the reference plane that approximates the tangent plane to the shock surface, the polynomial obtained from the second step of the MLS projection allows a more accurate evaluation of the surface normal at the same point based on a detailed description of the local geometry. However, the difference between $\boldsymbol{n}$ and $\boldsymbol{n}_T$ is usually not large as long as $\boldsymbol{n}_T$ makes sense in the first place. That being said, a successful calculation of the surface normal significantly depends on the reference plane being a solid approximate of the local

tangent to the shock surface. If the first step of the MLS projection procedure fails to yield an $\boldsymbol{n}_T$ that faithfully reflects the local geometry such as in the neighborhood of high curvature regions and sharp features, it is not realistic to expect an accurate $\boldsymbol{n}$ from the second step.

3.4 MLS-PGSD

As discussed in the previous section, the curvature (sum of two principal curvatures) of a shock surface at a given point can be obtained by computing the local MLS surface patch centered at that point. To be specific, on the reference plane a two-dimensional local coordinate system is built with an arbitrarily defined orthonormal basis, which enables the computation of the first- and second-order derivatives of the image function $\boldsymbol{x}(u, v)$ with respect to u and v. This leads to the first and second fundamental forms, and then the surface normal and curvature at the point simply follow. It should be pointed out that, curvature is an intrinsic geometric property that is independent of the choice of the coordinate system, but the calculation of the surface normal must undergo a transformation from local to global coordinate system so in the end the surface normal is defined in the same space as the point cloud.

Since surface normal and curvature are obtained from computing the MLS surface, the three-dimensional PGSD model is named MLS-PGSD, and it consists of the same essential components as the two-dimensional model:

$$\frac{d\boldsymbol{x}}{dt} = a_0 M \boldsymbol{n}, \tag{3.14}$$

$$\frac{dM}{dt} = \frac{-a_0 M}{\Phi(M)} \kappa. \tag{3.15}$$

Here, $\Phi(M) = -\frac{2}{M\theta}$ with $\theta(M)$ defined by Bach and Lee's analytical solution [105] and

introduced in Section 2.6. Moreover, $\Phi(M)$ for a spherical blast only needs to be solved for once due to its adaptation to any size of explosion, just similar to its counterpart for a cylindrical blast.

Now all ingredients of a Lagrangian scheme that solves the MLS-PGSD model are ready except surface regularization techniques. Similar to the scheme introduced in Section 2.3 , the time step size is still guided by the CFL condition [90]. In this case Δs_{min} can be found when searching the k-nearest neighbors within the octree data structure for each point to construct the MLS surface. Such a procedure also reveals the local point density, based on which insertion and removal of points are applied every few iterations.

Unlike deleting points from the point cloud in compressive regions of the shock front, adding points on the MLS surface where the local point density is insufficient is not a trivial task. Inspired by Alexa *et al.* [114], the basic idea is to compute the Voronoi diagram of the MLS surface and then add points at vertices of the diagram, if needed. However, computing the Voronoi diagram of the entire MLS surface is computationally expensive and not necessary. In practice, only local MLS surface patches with a lower point density than a user defined threshold is considered, and Voronoi diagrams are computed on local reference planes instead of on MLS surface patches. To be more specific, when computing the MLS surface following the procedures outlined in Section 3.2, all candidate points are first detected. These candidates are the ones centered at which a local MLS surface patch is built with fewer number of supporting neighbors than the threshold adapted to the local geometry. These patches may overlap but a fix to one patch usually solves the issue for the overlapping ones. Starting from a randomly selected point on the list, a local reference plane $\mathcal{H}$ is built in the first step of the MLS projection procedure and all supporting neighbors are projected onto $\mathcal{H}$. A Voronoi diagram of these points is computed and each vertex is equidistant from three or more neighbors, so circles can be drawn centered at vertices that touch neighbors without including any one of them inside. Then the circle

with the largest radius is chosen and its center (i.e., a Voronoi vertex) is projected onto the MLS surface thus becoming an added point. Such process is repeated interactively until the point density of this surface patch satisfies the density requirement set by the user. Moreover, all supporting neighbors of the current MLS surface patch should be compared to the points on the list. If a point on the list is found to be part of the current patch, it does not need a fix so it is removed from the list. In this way, no efforts are wasted in up-sampling overlapping patches.

Figure 3.3 illustrates this point-insertion procedure, in which all supporting neighbors represented by the black dots have already been projected onto the reference plane centered at the red square. A Voronoi diagram of these points is computed and cells are bounded by red segments. The vertex marked bold in the top-left corner is found to have the largest radius, so it is projected onto the local MLS surface patch and becomes the first added point there. At the end of the process, as indicated by Figure 3.3, five other vertices are also chosen to generate added points and the updated Voronoi cells are segmented by black dashed lines. As a result, the point density becomes nearly uniform on both the reference plane and the MLS surface patch.

A smoothing procedure can also be applied to dampen high frequency errors accumulated during the propagation of a shock surface in three dimensions. In contrast to the smoothing procedure designed for two-dimensional shock problems that is independent of the PGSD model, smoothing is naturally embedded in the MLS projection procedure. In fact, the MLS projection procedure not only provides the surface normal and curvature at the point to be projected, but also its projection on the MLS surface. Such relocation of points effectively removes high frequency noise present in numerical data in a least squares sense while ensuring the minimal loss of information. Additionally, since point relocation is just a side product of computing the MLS surface, application of the smoothing procedure does barely increase the computational cost.

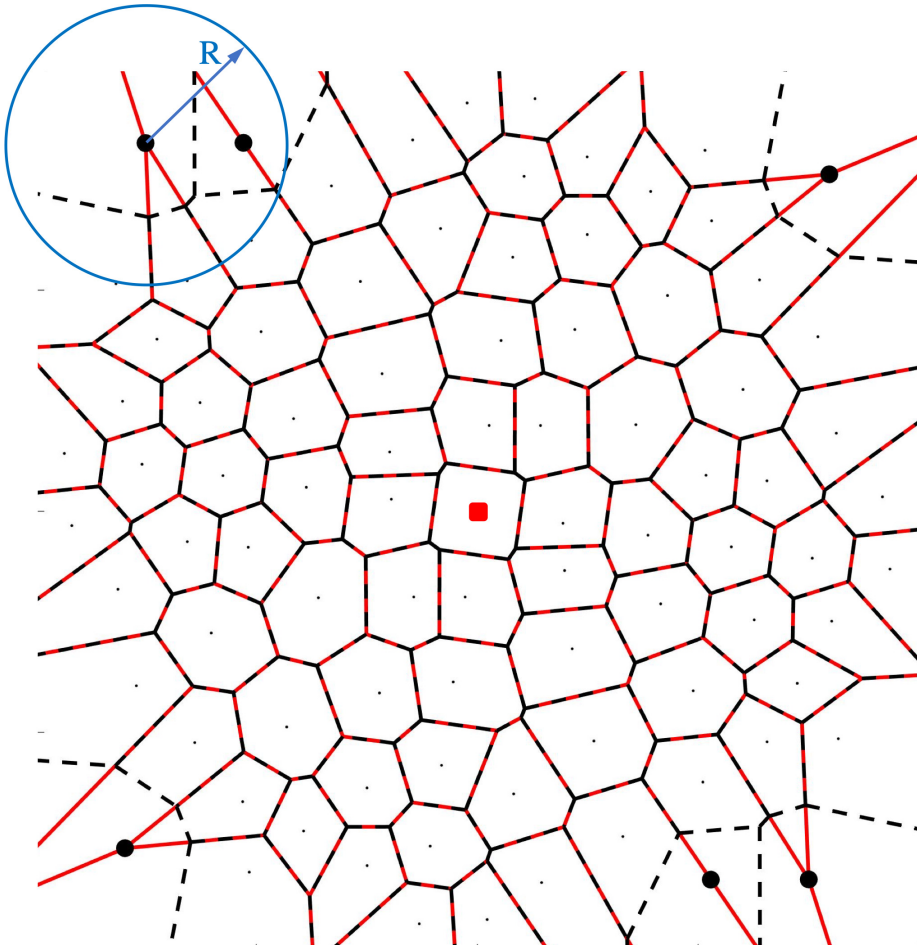

Figure 3.3: Schematic illustration of a Voronoi diagram on the local reference plane centered at a point (red square). In the regions of insufficient point (black dots) density Voronoi vertices (bold black dots) projected onto the MLS surface becoming the added points.

To verify that the MLS-PGSD model encodes the correct analytical information of blast motion in three dimensions, the propagation of a single spherical blast was first simulated and compared to the analytical solution. The initial conditions for the Lagrangian scheme ($R_0 = 30$ mm and $M_0 = 21.69$) were first obtained from Bach and Lee's analytical solution ($E_0 = 10,000$ J). Then a point cloud comprised of 1318 points was generated that represents the instantaneous blast surface. As shown in Figure 3.4, the resulting $M - R$ plot from the MLS-PGSD model agrees excellently with that from the analytical solution

with the largest discrepancy of 1.7% found at $R = 59$ mm. This shows that the accuracy of the MLS-PGSD model is good for being used for more complicated shock interaction problems in three-dimensional space.

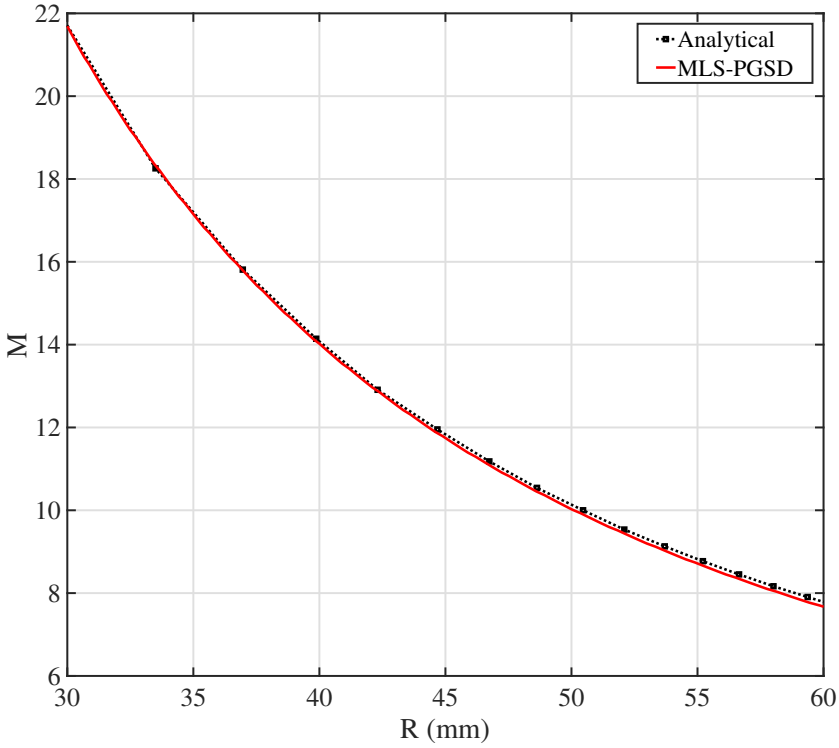

Figure 3.4: $M - R$ plots of the analytical and MLS-PGSD solutions to the propagation of a single spherical blast. Initial conditions: $E_0 = 10,000$ J for the analytical solution; $R_0 = 30$ mm and $M_0 = 21.69$ for the MLS-PGSD solution.

3.5 Application of MLS-PGSD to Blast Focusing Problems

In Section 2.8, a solution framework was proposed to solve two-dimensional blast focusing problems with the Lagrangian scheme solving the PGSD model. Analogously, interactions between spherical blasts of equal strength are supposed to be dealt with by a

similar framework but using the MLS-PGSD model. In this section, the MLS-PGSD model will be tested for the symmetric interaction between a pair of spherical micro-blast waves and compared to the experimental as well as Euler results. The experimental data is from the work of Jiang *et al.* [4], in which the behavior of a micro-blast wave was investigated by examining its propagation in space and subsequent reflection off a solid wall. In the experiment, a blast was generated by focusing laser beams in ambient air with a wall set at a stand-off distance of 5 mm below the focal point of the laser beams. The resulting blast can be considered as a point-blast and it was observed to have a nearly perfect spherical shape. The total energy released was measured to be 1.38 J, which is approximately equivalent to 3.3 mg TNT if assuming the conversion is only performed energy-wise. Euler simulations were also carried out by Jiang *et al.* [4] for the same configuration as the experiment. They used Taylor's similarity law to generate initial conditions for the axisymmetric simulation as discussed in Section 2.4, and the following calculation was taken over by a finite difference scheme.

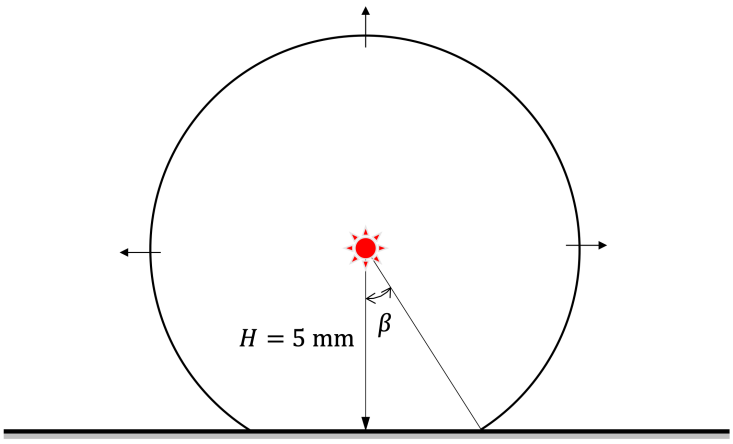

Figure 3.5: Schematic illustration of the experiment of Jiang *et al.* [4]. H: height of burst and β: angle of incidence.

In this work, the objective of the Lagrangian simulations that solve the MLS-PGSD model is to match the experiment of Jiang *et al.* [4] with minimal computational cost.

Therefore, the generation of the initial point cloud that leads to the most efficient calculation becomes the priority of the problem. Following the framework proposed in Section 2.4, the simulation should start when the transition from regular to Mach reflection first occurs. This transition information is given in the work of Jiang *et al.* [4] where the critical angle of incidence was measured between 30° to 37° in the experiment, while their Euler simulation indicated a larger critical angle. To resolve such conflict, transition criteria can be used as a reference. As discussed in Section 1.2.2, since the high-resolution requirement for observing a Mach stem at its very early stage can be satisfied due to the advancement in both computer hardware and experimental visualization systems, some recent studies [82, 83, 86, 87] successfully predicted the transition from regular to irregular reflection in unsteady flows using the pseudo-steady flow criteria, specifically, the sonic criterion. Slightly different than the experimental observation, the sonic criterion predicts a critical transition angle of around 39° for this micro-blast reflection case. Therefore, taking both the experimental observation and theoretical prediction into consideration, the critical angle of incidence was finally chosen to be 37° for the current Lagrangian simulation to make it comparable with the experiment.

Regarding the blast Mach number at the transition instance, though not provided in the work of Jiang *et al.* [4] it can be approximated using Bach and Lee's analytical solution to point-blast propagation. But, before proceeding to the determination of the instantaneous Mach number, the analytical solution itself as well as the MLS-PGSD model needs to be first proved to be valid for the propagation of a micro-blast as described by the experiment. By applying the shock jump conditions to compute the pressure in the flow immediately behind the blast front using Mach number, the resulting curves of maximum pressure at the blast front against the blast radius are presented in Figure 3.6. A good agreement was found between the current results (Lagrangian simulation and analytical solution) and that from Jiang *et al.*'s experiment in spite of possible uncertainties

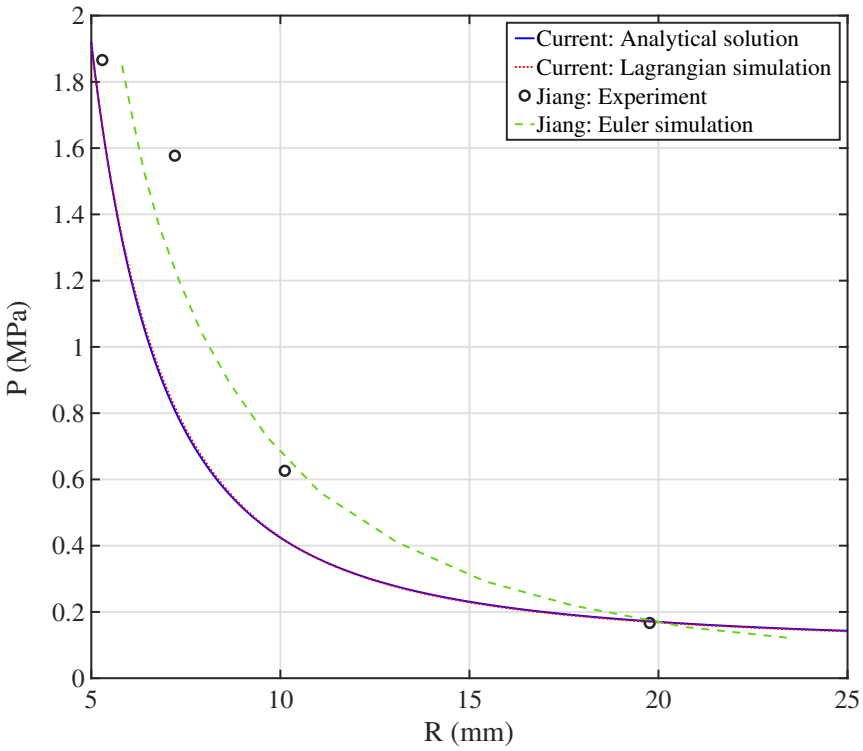

Figure 3.6: Pressure at the blast front as a function of distance from the explosion center. Initial conditions: $E_0 = 1.38$ J for the analytical solution; $R_0 = 5$ mm and $M_0 = 4$ for the Lagrangian simulation. Experimental and Euler simulation data reproduced from [4], with permission from Springer.

in the calibrated measurements, especially near the 5-mm location where the pressure from the current computations only shows a very slight discrepancy to the experimental data point. This agreement is also supported by the micro-blast reflection experiment. In the experiment the Mach number was estimated to be 3.8 at the moment when the blast touched the wall, while both the current computations reported a Mach number of 4.0 at the same stand-off distance.

In the case of a height of burst of 5 mm, an incidence angle of 37° corresponds to a spherical blast with a radius of 6.26 mm. For this size the blast front Mach number is found to be 3.08 using the analytical solution. Based on such a configuration, a point cloud was

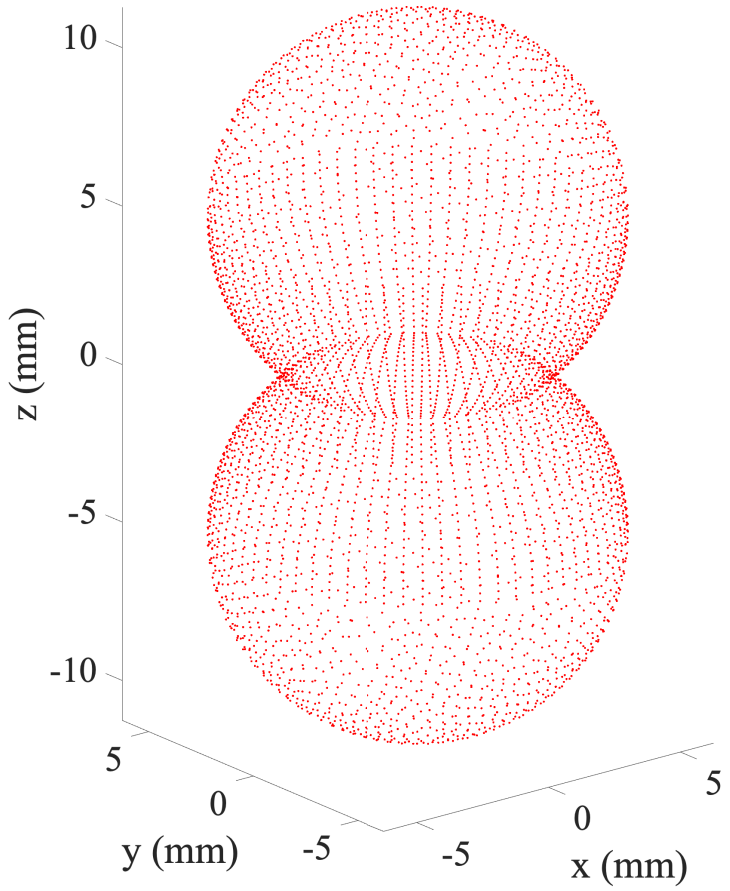

Figure 3.7: Initial point cloud that represents a surface created by the interaction between two identical spherical blasts.

generated that represents a continuous surface created by the symmetric interaction between two special blasts of the same strength, which is equivalent to a single blast reflecting off a solid wall. As shown in Figure 3.7, the point cloud consists of two sub-clouds that each represent a spherical blast, and no points exist inside any part of the spheres including where the two spheres overlap. Points are placed consistently in a latitudinal manner in the neighborhood of the intersection with point density gradually reduced towards the

orthodrome furthest away from the intersection. On the back of the two spheres points are more arbitrarily positioned but the point density is nearly uniform. Such arrangement of points is particularly designed to accommodate for the future growth of the Mach stem in the compressive regions. As for the size of the point cloud, if too many points are used to represent the underlying surface the simulation speed would be significantly lowered, but in the case of too few points the geometry of the Mach stem may not be well defined and the features contained in the neighborhood of triple points may not be preserved. As a result, in this case 4662 points were used to develop the point cloud that balances simulation speed and accuracy.

However, in the real world, the process of regular reflection between two spherical blasts represents physical singularities in space that emerge where blasts intersect in the sense of discontinuity in curvature and an undefined tangent plane. The subsequent transition to irregular reflection leads to not only a change in the shape of the shock front but also the smoothing of singularities due to a combination of physical properties, including viscosity and specific heat ratio. Though these physical attributes are not considered in the present mathematical model for simplicity, smoothing naturally occurs in the current numerical simulation. In the MLS-PGSD model, a continuous shock front surface is required and presented by a point cloud. For the case of micro-blast reflection off a solid wall, triple points arise as the result of the occurrence of Mach reflection and are manifested in the form of singularities of the shock surface. These singularities may not be precisely spatially represented by points in the cloud, but they are still smeared during the MLS projection procedure. Even though such smearing of the singularities is purely numerical rather than physical, it provides essential differential geometry information that is needed for the PGSD model. More importantly, given the violent nature of Mach reflection that expands at a very high velocity, severe numerical instability is more likely to arise in the neighborhood of triple points. In fact, despite the smoothing procedure that is only applied

every few iterations, the number of supporting points used to build an MLS surface patch is the key for maintaining numerical stability and accuracy. The choice of the number of neighbors is subject to the local surface smoothness but should be independent of point spacing that varies as the surface evolves, such that an n-tier type structure is used to define the neighborhood domain as illustrated in Figure 3.8. If the point to be projected is in the undisturbed part of the shock front, a two-tier point structure built around that point is sufficient to yield accurate surface normal and curvature as proved in the previous case of propagation of a single micro-blast. A similar structure was also used by Zhang *et al.* [118], albeit defined in a triangulated mesh, to develop a least squares smoothing procedure for the case of a collapsing bubble surface in three dimensions. On the other hand, if the point to be projected is near triple points, at least a four-tier point structure is needed. The resulting MLS surface patch is of a similar size as that approximating the undisturbed part of the shock front due to the higher point density in the neighborhood of triple points as designed in the initial point cloud. A similar effect can also be achieved by adjusting h of the weight function while having the same point structure anywhere, but this is less efficient.

To further speed up the Lagrangian simulation, the MLS projection procedure was also optimized. For points far away from the compressive regions, by assuming that the reference plane $\mathcal{H}$ passes through the point to be projected in the first step of the MLS projection procedure, the number of variables in nonlinear equation (3.1) is reduced to one, i.e., $(\boldsymbol{n}_T, d) \rightarrow \boldsymbol{n}_T$. Such assumption is reasonable if the input point is close to the underlying surface that is free of any sharp features, the points on the back of two spheres for example. This simplification saves the computational cost of iterative minimization while only minimally affecting accuracy of the projection. However, for the points in the neighborhood of the compressive regions, a complete optimization of equation (3.1) is necessary, otherwise the resulting surface normal and curvature may be wrong.

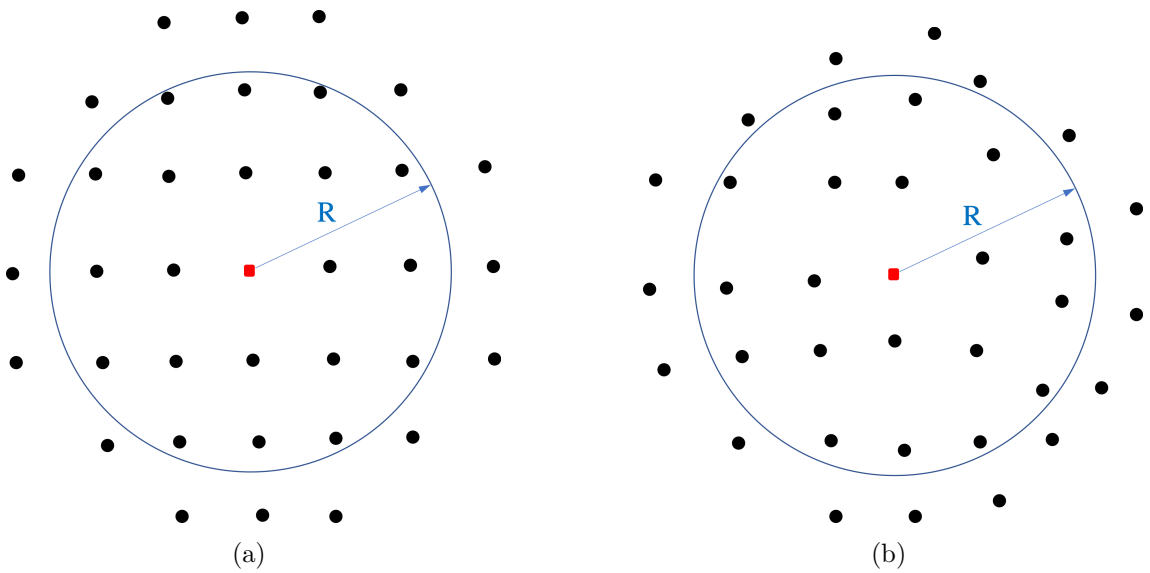

Figure 3.8: Schematic illustration of the neighbor point domain with a two-tier type structure around the point to be projected (red square) within a search ball for (a) consistent placement of points; (b) more arbitrary placement of points.

Only three time instants were chosen in the work of Jiang *et al.* [4] to present the instantaneous interferograms obtained in the experiment, during which the blast front experienced the transition from regular to irregular reflection due to its interaction with the solid wall. To replicate such a process, the Lagrangian simulation was started at the transition instance with the initial point cloud expanding at $M_0 = 3.08$ and lasted more than 4 µs. By projecting the resulting point cloud onto the xz-plane, the two-dimensional contours of the blast front at 2 µs and 4 µs (time starts from the transition instant in the Lagrangian simulation) were obtained. In Figure 3.9 the numerical results are overlaid onto the corresponding experimental interferograms with the same scale, despite the fact that it is unclear whether optical distortions were removed in the experiments. The first observation is that the undisturbed part of the shock front from the Lagrangian simulation agrees well with that from the experiment at both selected time instances, though the interferograms appear to be slighted distorted while the Lagrangian contours maintain a perfect spherical shape. However, Figure 3.9(a) indicates that the Mach stem predicted by

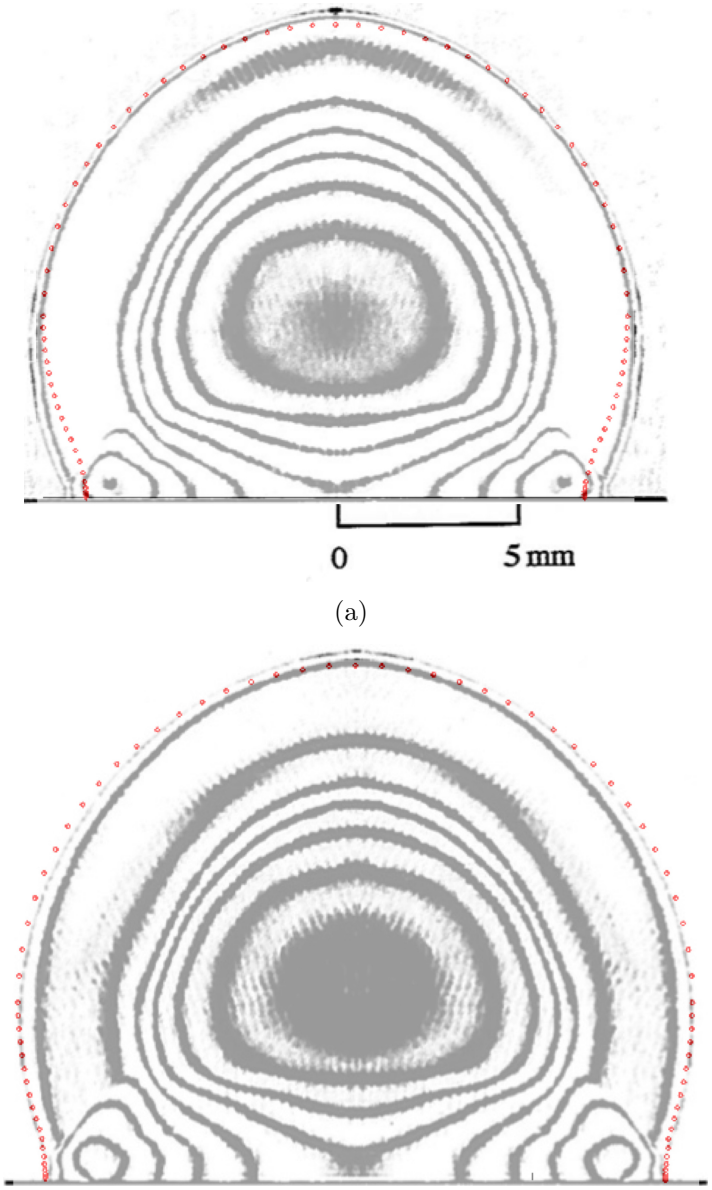

(a)

(b)

Figure 3.9: Overlay of the blast front contours at the same time instances from the current Lagrangian simulation (red circles) and the experimental interferograms (background) from [4] with permission from Springer. (a) 2 µs after the transition instant; (b) 4 µs after the transition instant.

the MLS-PGSD model has been propagating at a lower speed along the wall compared to the experiment while the Mach stem height is of similar magnitude. This observation

may be partially due to the choice of the number of supporting neighbors used to build the local MLS surface patches for the sake of numerical stability, which nonetheless excessively restricted the growth of the Mach stem at its early stage. Consequently, the neighboring part of the contour lags behind. After another 2 µs, as the Mach stem weakened during propagation, the effect of smearing should be alleviated so the blast front contour predicted by the MLS-PGSD model is expected to match better the experimental interferogram. This is verified by Figure 3.9(b), in which the two blast front contours almost overlap despite the slight distortion in the experimental interferogram.

Maximum pressure at the Mach stem can also be extracted from the Lagrangian solution and it was found to be on the plane of $z = 0$ throughout the simulation. That being said, the extreme events always occurred at the reflecting wall from the perspective of image bursts [10], and this makes the maximum pressure profile comparable to the data from height of burst studies if expressed as a function of angle of incidence. In an effort that combines experimental and analytical results, several reflected pressure profiles at the wall as a function of angle of incidence were given by Unified Facilities Criteria 3-340-02 (UFC) [5] for some characteristic scaled heights of charge, $H/W^{\frac{1}{3}}$, where W being the weight of the TNT charge and H the height of burst. For this micro-blast reflection case, the scaled height of charge turns out to be 1.83 ft/lb$^{\frac{1}{3}}$. The closest characteristic value reported by UFC is 1.9 ft/lb$^{\frac{1}{3}}$ and the corresponding pressure history is reproduced in Figure 3.10. In general, the curve from the Lagrangian simulation shares a similar trend with the UFC data and they gradually get closer with an increase in the angle of incidence. However, in contrast to the observation made in the case of two-dimensional symmetric blast interaction where the Mach stem was overestimated by the PGSD model, in this case the peak pressure at the Mach stem was found to be lower than that of the UFC data. The reason is still unknown and the lack of the source of information of the UFC data further obscures the comparison. On the other hand, the three-dimensional Euler solution (the setup of the

current Euler simulation and its comparison with Jiang *et al.*'s results [4] can be found in Appendix A.1) shows a better agreement with that from the Lagrangian simulation as shown in Figure 3.10. However, this time the Lagrangian simulation is conservative in developing the Mach stem at its early stage. The reason may partially be the choice of the number of neighbor points to compute the local MLS surface patches as discussed earlier. Additionally, since the maximum pressure can only be obtained from GSD by being converted from the resulting shock front Mach number, its accuracy is questionable if the energy is condensed in a limited volume bounded by the shock front, when a Mach stem is just formed, for example. Thus, such comparison of pressure at the very early stage of Mach stem growth is less reliable.

Finally, the advantage of geometrical shock dynamics in efficiency is inherited by the three-dimensional MLS-PGSD model and was proved in this study. The Lagrangian simulation for the reflection case took approximately 16 hours on a single core of Intel Core(TM) i7-8750H CPU operating at 2.20 GHz with 32 GB memory, while the three-dimensional Euler simulation was finished after 14 days with four cores of Intel Core(TM) i7-3930K CPU operating at 3.20 GHz with 16 GB memory.

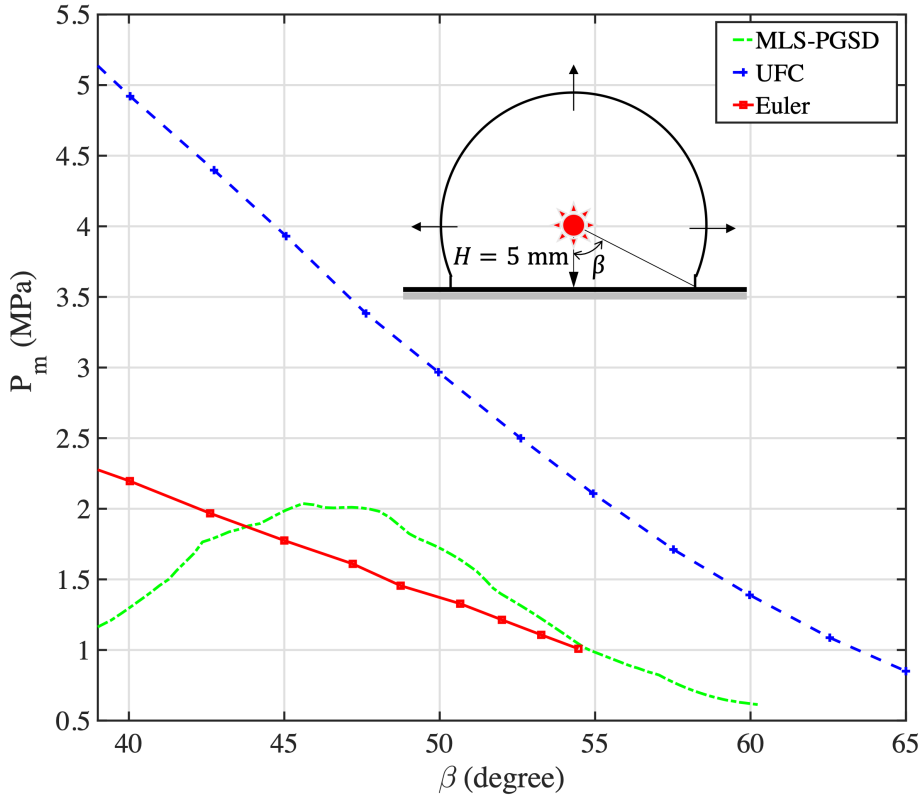

Figure 3.10: Maximum pressure at the Mach stem, P_m, as a function of angle of incidence, β. Initial conditions for the Euler and Lagrangian MLS-PGSD simulations based on the experiment [4]. UFC data reproduced from [5] for the scaled height of charge of 1.9 ft/lb$^{\frac{1}{3}}$.

3.6 Chapter Summary

In this chapter, by taking advantage of PGSD in its capability to be extended to three dimensions, the MLS-PGSD model that describes blast motion in three-dimensional space was proposed and the associated Lagrangian scheme was elaborated on. The essential component of this novel model is to compute the MLS surface that approximates the underlying shock front surface defined by a point cloud. The main idea of computing an MLS surface is the definition of a projection procedure that is able to project any point near, or in, the point cloud onto the same surface. Then, the MLS surface is such projection surface defined by the points that can be projected onto themselves. Since the projection

involves two procedures that each solve an optimization problem, the related theories and techniques were also given in detail in this chapter.

The application of the projector to each point in the cloud not only yields differential geometric properties that are needed by PGSD, but also is able to obtain a piecewisely smoothed surface that filters out high frequency errors in a least squares sense. Such smoothing can be viewed as a surface regularization tool and almost no extra computational cost is added. Deleting points from the point cloud is a simple task, if necessary, since the octree data structure does not store any connectivity information. Point-insertion is also viable though requires some efforts. It is achieved by computing the Voronoi diagrams on local reference planes and then adding points at vertices where the point density is most scarce.

Lagrangian MLS-PGSD simulations were performed for a height of burst case and compared to the experiment of Jiang *et al.* [4]. In the experiment, investigations were made for the propagation of a spherical micro-blast generated by focusing laser beams and then subsequent reflection off the wall. Following the same order, the MLS-PGSD model was first verified by the experimental data for the propagation phase. Once the point cloud for the irregular reflection phase was generated using the information of transition from regular to irregular reflection, the Lagrangian scheme took over the following calculation for the Mach reflection. The resulting blast front contours after 2 µs and 4 µs counting from the transition instant were overlaid onto the experimental interferograms. At $t = 2$ µs, the Lagrangian simulation predicted a Mach stem having propagated less distance along the wall. This may be due to the choice of the number of neighbor points used to compute the local MLS surface patches, which maintained the numerical stability at the expense of restricting the Mach stem growth at its early stage. As the Mach stem weakens during expansion, the effect of numerical smearing is alleviated so the two blast front contours almost overlap at $t = 4$ µs. These observations were echoed in the plot of the maximum

pressure at the Mach stem as a function of angle of incidence, in which the curve from the Lagrangian simulation reaches the peak value at a later time when compared to the three-dimensional Euler solution, but the two curves gradually converge with time.

Chapter 4

Summary and Future Directions

4.1 Summary

This dissertation investigated the possibility of applying front-tracking based GSD algorithms to two-dimensional and three-dimensional blast focusing problems. In Chapter 2, three models that extend two-dimensional GSD to account for the post-shock flow effect were discussed in detail. The comparison between the first-order complete and fully complete GSD models revealed the importance of preserving an intact post-shock flow term, which is truncated by the original GSD model, in predicting blast motion. Among these models, due to its accuracy and independence of initial energy of the point-explosion, the PGSD model was chosen for a general framework aiming at efficiently solving the irregular reflection phase of blast focusing problems. Experiments of Higashino *et al.* [2] was numerically replicated by the Lagrangian simulations that solve the PGSD model, and the resulting plot of the maximum pressure at the Mach stem as a function of time showed a trend in agreement with the experiment, however, an overestimation of the Mach stem growth was also observed. In order to address this issue, an alternative model that is able to start the simulation with initially separated blasts was derived and examined for the

symmetric interaction between two cylindrical blasts. The resulting trajectory of triple points indicates an underestimated Mach stem possibly due to the assumption of a straight Mach stem.

To take advantage of PGSD in its capability to be extended to three dimensions, a Lagrangian scheme based on the MLS-PGSD model was developed for three-dimensional blast focusing problems in Chapter 3. Unlike the traditional three-dimensional GSD studies using triangulated meshes, in this new model a point (particle) cloud arranged in an octree data structure was used to represent the shock surface. The curvature and surface normal that is required by the model is achievable by computing the MLS surface that approximates the underlying shock surface. Lagrangian simulations were performed for the case of a micro-blast reflection off a reflecting wall and compared to the experimental results of Jiang *et al.* [4]. A good agreement of the blast front contour at different time instants was confirmed. Moreover, a three-dimensional Euler simulation was also carried out for the same case. The difference of the maximum pressure at wall at the early stage of Mach stem growth revealed the possible influence of the choice of the parameters in computing the MLS surface.

Additionally, as presented in the Appendix, the Euler solver used throughout this work and the method to generate initial conditions for blast simulations were verified by the comparison with Jiang *et al.*'s study [4]. Grid independence studies were then carried out to determine the grid size that best balances simulation speed and accuracy.

4.2 Future Directions

The PGSD model introduced in Section 2.6 encodes correct point-blast propagation information by containing the essential component of Bach and Lee's analytical solution. In fact, not only point-explosion is targeted, a model in a similar form can encode any real

explosion whose resulting blast wave is affected by numerous factors including shape of the charge, efficiency of energy release, gas product and media, etc. To obtain the $\kappa - M$ relation for the new model, some form of formula describing how the resulting blast behaves as it expands is required either in a direct or an indirect manner. However, unlike the PGSD model, the new model developed for a particular explosion event is not necessarily independent of energy size.

All GSD models are essentially built upon some $\kappa - M$ relation, though that varies for different types of shock waves. The $\kappa - M$ relation describes how a shock front element accelerates subject to the local curvature, so the calculation of curvature becomes the priority when the accuracy of that GSD model is concerned. Among all the two-dimensional Lagrangian schemes that solve a GSD model, cubic spline interpolation is the most popular tool used to compute the curvature. Such interpolation process inevitably smooths out singularities, for example triple points in the cases of multi-shock interaction. On the other hand, such smoothing in turn reshapes the neighborhood of the singularities that are originally undefined due to discontinuous tangent and curvature. As a result, differential geometric properties required by GSD can then be determined at the singularities. Moreover, as shown in Section 2.8, GSD always tends to overestimate the growth of a Mach stem, and it is reasonable to relate this observation to imperfect estimation of the curvature at the triple points. In the future, the interpolation procedure should be further investigated in the hope of making the resulting curvature better reflect the local shock behavior near triple points.

Similarly, when applying the $\kappa - M$ relation to three-dimensional shock focusing problems, the calculation of curvature (i.e., sum of two principal curvatures) is the major source of error. Unlike two-dimensional cases in which the resulting cubic spline interpolant connects all given particles, the MLS surface approximation is indeed a least squares fitting method that does not necessarily pass through every point (particle) in three-dimensional

space, so the curvature is estimated at these relocations rather than where points are originally positioned. In general, this approximate surface is smoothed and very close to the underlying surfaces defined by the input point cloud. However, in the neighborhood of where shocks intersect the relocation may be far enough away to make the resulting curvature inappropriate. There are some parameters that can be tuned to adjust the local surface smoothness still having to be systematically studied, including those in the weight function and octree data structure. The number of neighbor points used to build a local MLS surface patch also affects how far the point to be projected would be moved, however, that depends on the local point placement. For the case of micro-blast reflection off a wall as presented in Section 3.5, points were initially densely placed in a consistent pattern near triple points, while a more arbitrary placement was utilized for the points far away from the triple points. In the future, completely arbitrary initial placement of points should be a direction to explore and the effort may concentrate on how to suppress error accumulation as the result of a significantly uneven point distribution. This investigation will also extend the application of the MLS-PGSD model to more complicated multi-blast interaction problems. Finally, in order to accelerate the three-dimensional problem solving process, parallelization of the Lagrangian MLS-PGSD scheme is a priority such that the benefit of GPU computing can be exploited.

Appendix A

A.1 Verification of the Euler Solver and Initial Conditions

To verify the Overture Euler solver [106] and the initial conditions for blast dynamics problems, simulations were performed for the propagation of a spherical blast in air created by a 1.38 J point-explosion and compared to the results presented in the work of Jiang *et al.* [4]. For this specific case, initial conditions were provided by Taylor's similarity law [35] that solves flow properties internal to the shock front at a particular radius. Then the Euler equations were solved Overture's three-dimensional inviscid compressible solver on a computational domain that covers a cube of 16 mm with varied grid sizes. A probe was inserted 5 mm away from the explosion center at which pressure was collected as a function of time.

Figure A.1(a) shows the measured pressure time history from Jiang *et al.*'s experiment. In the experiment a micro-blast wave was created by pulsed-laser beam focusing with a total energy of 1.38 J discharged at 1.4 kV. Jiang *et al.*'s numerical result is presented in Figure A.1(b) in which results from our current Euler simulations are also shown. In general, a similar trend can be seen in all pressure profiles but peak pressure values differ. Approximately 1.9 MPa was recorded as the highest value by the pressure

transducer in the experiment, whereas a peak value of 1.7 MPa can be read from Jiang *et al.*'s axisymmetric simulation with gird size $\Delta x \times \Delta r = 0.035$ mm $\times$ 0.05 mm. Despite substantial discrepancy in blast arrival time between the experiment and all current Euler simulations (also manifested in Jiang *et al.*'s simulation) due to uncertainties in the experimental data, a peak pressure of 1.55 MPa was achieved in this study compared to 1.9 MPa from Jiang *et al.* This result was achieved by using a uniform grid size of $\Delta s = \Delta x = \Delta y = \Delta z = 0.05$ mm. In comparison, though adaptive mesh refinement (AMR) was implemented for all current simulations that equally regrids a cubic grid into eight when necessary, a coarse grid (i.e., $\Delta s = 0.1$ mm) did not yield a peak pressure as high as using a fine grid (i.e., $\Delta s = 0.05$ mm). It is worth pointing out that the choice of the initial spherical blast radius also plays an important role in final results. If Taylor's similarity law was solved at $R_0 = 3$ mm to generate initial conditions, a slightly underdeveloped blast was observed when compared to $R_0 = 1.5$ mm using the same mesh. So according to this present study, the three-dimensional Euler simulation for the case of micro-blast reflection (as presented in Section 3.5) used a uniform grid size of $\Delta s = 0.05$ mm with AMR.

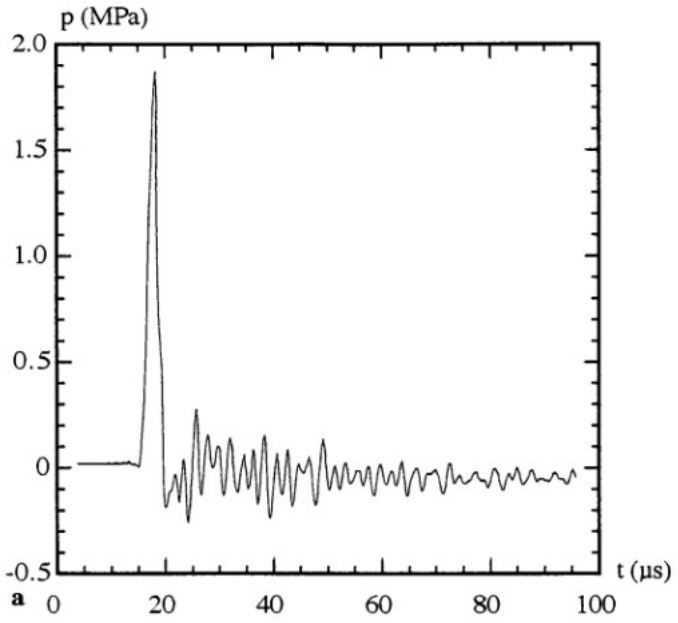

(a)

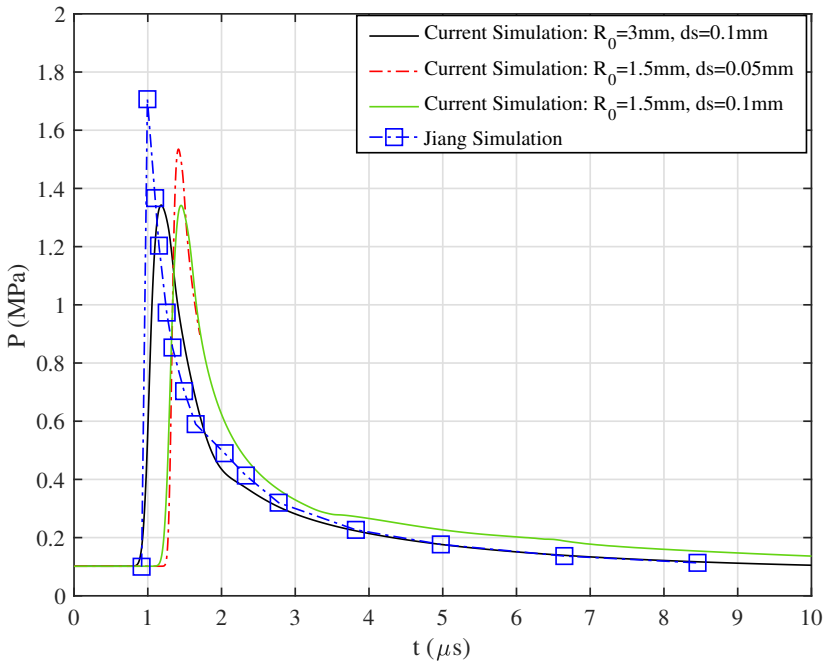

(b)

Figure A.1: Time history of pressure recorded 5 mm away from the explosion center: (a) Experimental data from Jiang *et al.* [4], with permission from Springer; (b) Numerical results from current Euler simulations and that reproduced from Jiang *et al.* [4], with permission from Springer.

A.2 Grid Independence Study for 2D Euler Simulations

Though the Overture Euler solver and the usage of Taylor's similarity law to generate initial conditions for blast dynamics problems have been discussed as above, a grid independence study is still needed to find a proper grid size for two-dimensional simulations. The test case is blast reflection off a solid wall. Specifically, as illustrated in Figure A.2, a single explosive with a total energy of 8,000 J/m is positioned 10 mm above the reflecting wall and two probes are placed (i) 5 mm above the wall (Probe A), and (ii) at the wall (Probe B). The former probe would not only record pressure history of the incident blast that expands from the initial radius of 1.5 mm, but also monitor the influence of the reflected wave on the flow at that location. Three different squared grid sizes were tested: 0.1 mm, 0.04 mm and 0.016 mm. Figure A.3(a) shows the time history of pressure recorded by probe A. The results from the 0.04 mm grid and the 0.1 mm grid display a maximum difference in incident blast Mach number of 8.3%, while 5.3% is observed between the 0.016 mm grid and the 0.04 mm grid. Moreover, the 0.016 mm grid and the 0.04 mm grid predict an almost identical second peak as the result of the passage of the reflected shock, while the coarsest mesh slightly delays its arrival. Regarding the Mach number at wall, lager discrepancies between these three grid sizes can be seen in Figure A.3(b). Theoretically, a high grid resolution enables more accurate results, but it requires more computational resources. For this test case, more than 72 hours were needed for the simulation using the 0.016 mm grid with two cores of Intel Core(TM) i7-3930K CPU operating at 3.20 GHz with 16 GB memory, while that using the 0.04 mm grid only took almost 12 hours. Therefore, a uniform grid sized at 0.04 mm is chosen for the two-dimensional Euler simulations throughout this work to balance simulation accuracy and speed.

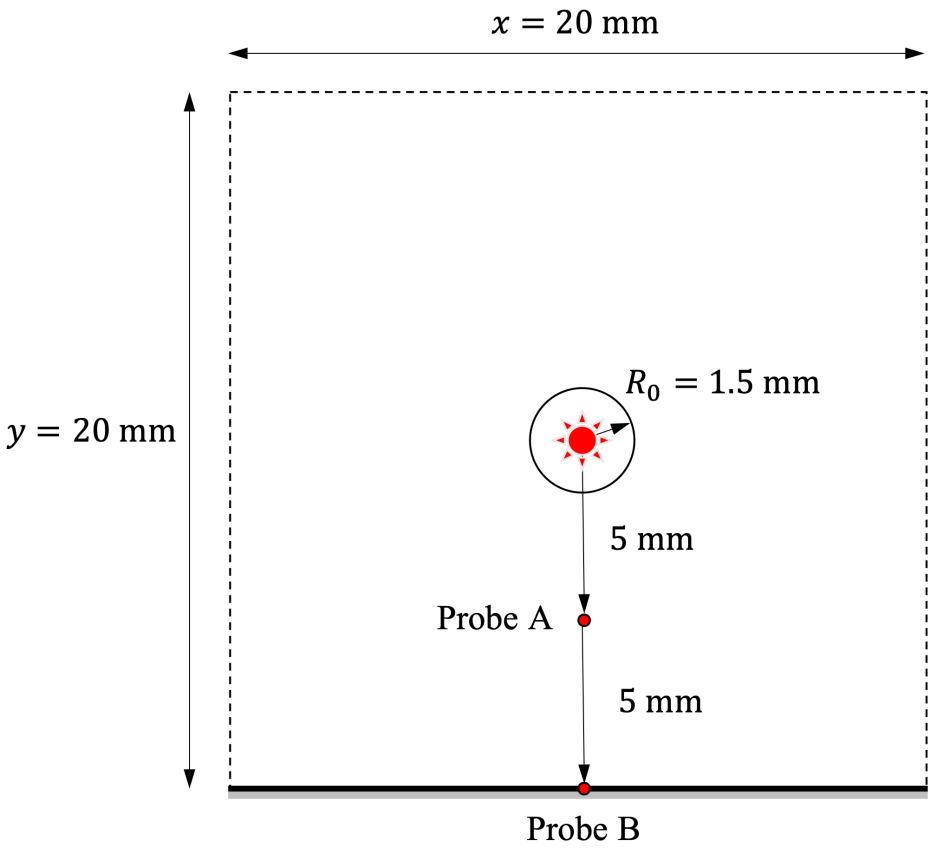

Figure A.2: Schematic illustration of the 2D Euler simulation domain for the grid independence study.

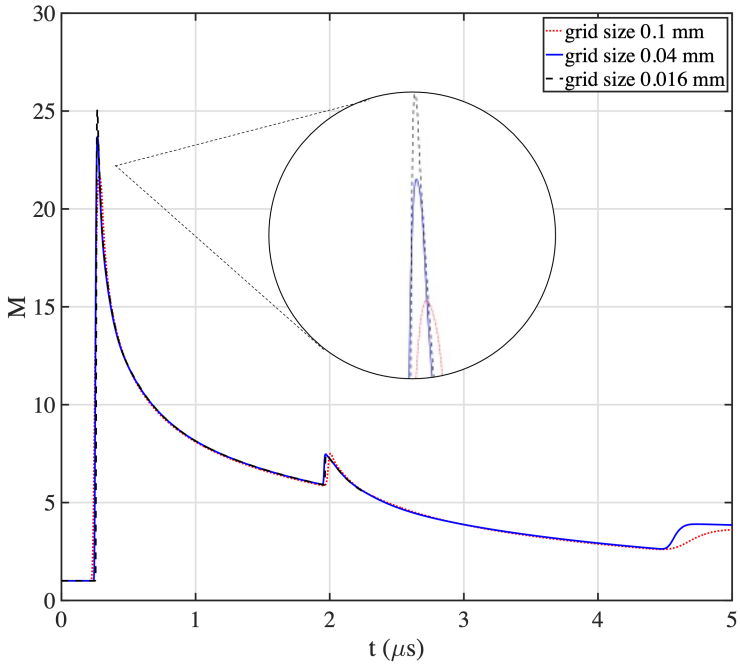

(a)

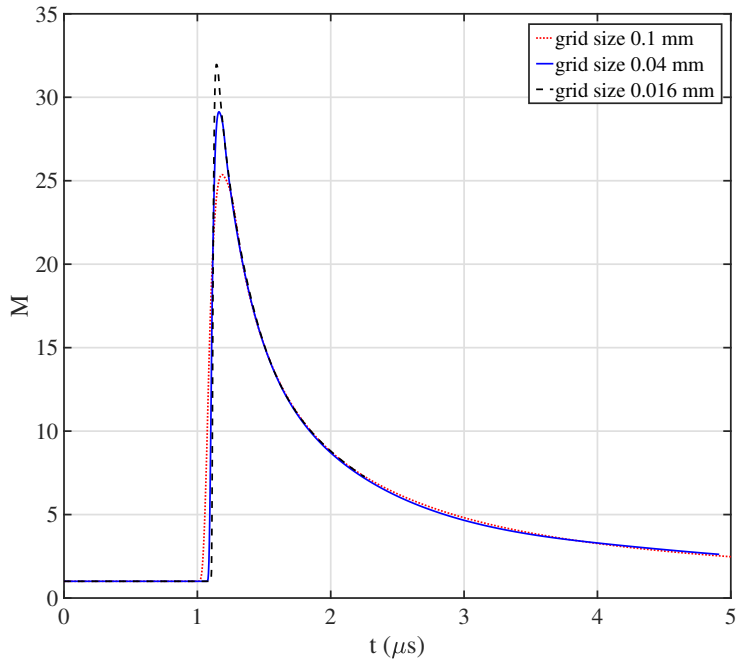

(b)

Figure A.3: Time history of pressure recorded at: (a) Probe A located halfway between the explosion center and the wall; (b) Probe B located at the wall.

Bibliography

[1] G. Ben-Dor, *Shock Wave Reflection Phenomena*. Springer, Berlin, 2007.

[2] F. Higashino, L. F. Henderson, and F. Shimizu, "Experiments on the interaction of a pair of cylindrical weak blast waves in air," *Shock Waves*, vol. 1, no. 4, pp. 275–284, 1991.

[3] S. Qiu, *Numerical study of focusing effects generated by the coalescence of multiple shock waves*. PhD thesis, University of Southern California, 2017.

[4] Z. Jiang, K. Takayama, K. P. B. Moosad, O. Onodera, and M. Sun, "Numerical and experimental study of a micro-blast wave generated by pulsed-laser beam focusing," *Shock Waves*, vol. 8, no. 6, pp. 337–349, 1998.

[5] "Unified Facilities Criteria Program. 2008. Structures to resist the effects of accidental explosions (UFC 3-340-02)," Tech. Rep., Washington, DC: U.S. Department of Defense, Unified Facilities Criteria Program. Supersedes TM 5-1300, 2008.

[6] N. Apazidis and V. Eliasson, *Shock focusing phenomena*. Springer, Berlin, 2018.

[7] G. Iosilevskii and D. Weihs, "Speed limits on swimming of fishes and cetaceans," *Journal of The Royal Society Interface*, vol. 5, no. 20, pp. 329–338, 2008.

[8] F. Y. Shen, R. F. Gao, W. J. Liu, and W. J. Zhang, "Physical analysis of the process of cavitation in xylem sap," *Tree Physiology*, vol. 22, no. 9, pp. 655–659, 2002.

[9] Q. Wan, *Numerical Investigation of Shock Wave Attenuation*. PhD thesis, University of Southern California, 2017.

[10] C. E. Needham, *Blast waves*. Springer, Berlin, 2010.

[11] K. G. Guderley, "Starke kugelige und zylindrische verdichtungsstosse in der nahe des kugelmitterpunktes bnw. der zylinderachse," *Luftfahrtforschung*, vol. 19, p. 302, 1942.

[12] K. P. Stanyukovich and F. S. Sherman, *Unsteady Motion of Continuous Media*. Pergamon Press, Oxford, 1961.

[13] E. A. Mishkin and Y. Fujimoto, "Analysis of a cylindrical imploding shock wave," *Journal of Fluid Mechanics*, vol. 89, no. 1, pp. 61–78, 1978.

[14] R. B. Lazarus, "Comments on "analysis of spherical imploding shocks"," *The Physics of Fluids*, vol. 23, no. 4, pp. 844–844, 1980.

[15] R. B. Lazarus and R. D. Richtmyer, "Similarity solutions for converging shocks," Tech. Rep., Los Alamos National Lab., Los Alamos, NM, USA, 1977.

[16] M. Yousaf, "Imploding spherical and cylindrical shocks," *The Physics of Fluids*, vol. 29, no. 3, pp. 680–684, 1986.

[17] A. Ramu and M. P. R. Rao, "Converging spherical and cylindrical shock waves," *Journal of Engineering Mathematics*, vol. 27, no. 4, pp. 411–417, 1993.

[18] V. D. Sharma and C. Radha, "Similarity solutions for converging shocks in a relaxing gas," *International Journal of Engineering Science*, vol. 33, no. 4, pp. 535–553, 1995.

[19] R. W. Perry and A. Kantrowitz, "The production and stability of converging shock waves," *Journal of Applied Physics*, vol. 22, no. 7, pp. 878–886, 1951.

[20] P. N. Baronets, "Imploding shock waves in a pulsed induction discharge," *Fluid Dynamics*, vol. 19, no. 3, pp. 503–508, 1984.

[21] K. Takayama, H. Kleine, and H. Grönig, "An experimental investigation of the stability of converging cylindrical shock waves in air," *Experiments in Fluids*, vol. 5, no. 5, pp. 315–322, 1987.

[22] M. Kjellander, N. Tillmark, and N. Apazidis, "Experimental determination of self-similarity constant for converging cylindrical shocks," *Physics of Fluids*, vol. 23, no. 11, p. 116103, 2011.

[23] S. Hikada and C. Needham, "Low altitude multiple burst (LAMB) model," *Volume I-Shock Description, DNA 5863Z-1, Defense Nuclear Agency, Washington, DC, USA*, 1981.

[24] H. L. Brode, "Quick estimates of peak overpressure from two simultaneous blast waves," Tech. Rep., R & D Aassociates, Marina Del Rey, CA, USA, 1977.

[25] R. P. Yeghiayan, W. N. Lee, and J. P. Walsh, "Blast and thermal effects of multiple nuclear burst exposure of aircraft in a base-escape mode," Tech. Rep., Kaman AviDyne, Burlington, MA, USA, 1977.

[26] R. H. Craver, J. T. McGahan, and E. Muller, "Mx mps deployment, an on-site fallout evaluation," Tech. Rep., Science Applications International Corporation, McLean, VA, USA, 1978.

[27] J. W. Aubrey, H. J. Abeyta, and W. E. Gifford III, "Lamb multiburst calculations for various attack scenarios," Tech. Rep., Air Force Weapons Lab., Kirtland, NM, USA, 1980.

[28] J. H. Keefer and R. E. Reisler, "Simultaneous and non-simultaneous multiple detonations," *Shock Tubes and Waves*, pp. 543–552, 1984.

[29] S. Yee and K. Abe, "Numerical simulation of cylindrically converging shock waves," *Computational Fluid Dynamics' 92*, pp. 57–60, 1992.

[30] D. L. Book and R. Löhner, "Simulation and theory of the quatrefoil instability of a converging cylindrical shock," *AIP Conference Proceedings*, vol. 208, no. 1, pp. 149–154, 1990.

[31] T. Aki and F. Higashino, "A numerical study on implosion of polygonally interacting shocks and consecutive explosion in a box," *AIP Conference Proceedings*, vol. 208, no. 1, pp. 167–172, 1990.

[32] S. I. Betelu and D. G. Aronson, "Focusing of noncircular self-similar shock waves," *Physical Review Letters*, vol. 87, no. 7, p. 074501, 2001.

[33] K. Balasubramanian and V. Eliasson, "Numerical investigations of the porosity effect on the shock focusing process," *Shock Waves*, vol. 23, no. 6, pp. 583–594, 2013.

[34] S. Qiu and V. Eliasson, "Interaction and coalescence of multiple simultaneous and non-simultaneous blast waves," *Shock Waves*, vol. 26, no. 3, pp. 287–297, 2016.

[35] G. I. Taylor, "The formation of a blast wave by a very intense explosion i. theoretical discussion," *Proceedings of the Royal Society of London. Series A. Mathematical and Physical Sciences*, vol. 201, no. 1065, pp. 159–174, 1950.

[36] R. F. Chisnell, "The motion of a shock wave in a channel, with applications to cylindrical and spherical shock waves," *Journal of Fluid Mechanics*, vol. 2, no. 3, pp. 286–298, 1957.

[37] W. Chester, "The quasi-cylindrical shock tube," *The London, Edinburgh, and Dublin Philosophical Magazine and Journal of Science*, vol. 45, no. 371, pp. 1293–1301, 1954.

[38] G. B. Whitham, "A new approach to problems of shock dynamics part i two-dimensional problems," *Journal of Fluid Mechanics*, vol. 2, no. 2, pp. 145–171, 1957.

[39] G. B. Whitham, "A new approach to problems of shock dynamics part 2. three-dimensional problems," *Journal of Fluid Mechanics*, vol. 5, no. 3, pp. 369–386, 1959.

[40] G. B. Whitham, *Linear and nonlinear waves*, vol. 42. John Wiley & Sons, New York, 1974.

[41] W. D. Henshaw, N. F. Smyth, and D. W. Schwendeman, "Numerical shock propagation using geometrical shock dynamics," *Journal of Fluid Mechanics*, vol. 171, pp. 519–545, 1986.

[42] D. W. Schwendeman, "A numerical scheme for shock propagation in three dimensions," *Proceedings of the Royal Society of London. A. Mathematical and Physical Sciences*, vol. 416, no. 1850, pp. 179–198, 1988.

[43] S. Qiu, K. Liu, and V. Eliasson, "Parallel implementation of geometrical shock dynamics for two dimensional converging shock waves," *Computer Physics Communications*, vol. 207, pp. 186–192, 2016.

[44] R. Knystautas, B. H. K. Lee, and J. H. S. Lee, "Diagnostic experiments on converging detonations," *The Physics of Fluids*, vol. 12, no. 5, pp. I–165, 1969.

[45] R. A. Roig and I. I. Glass, "Spectroscopic study of combustion-driven implosions," *The Physics of Fluids*, vol. 20, no. 10, pp. 1651–1656, 1977.

[46] T. Saito and I. I. Glass, "Temperature measurements at an implosion focus," *Proceedings of the Royal Society of London. A. Mathematical and Physical Sciences*, vol. 384, no. 1786, pp. 217–231, 1982.

[47] J. H. T. Wu, R. A. Neemeh, and P. P. Ostrowski, "Experiments on the stability of converging cylindrical shock waves," *AIAA Journal*, vol. 19, no. 3, pp. 257–258, 1981.

[48] M. Watanabe and K. Takayama, "Stability of converging cylindrical shock waves," *Shock Waves*, vol. 1, no. 2, pp. 149–160, 1991.

[49] M. Watanabe, O. Onodera, and K. Takayama, "Shock wave focusing in a vertical annular shock tube," in *Shock Waves@ Marseille IV*, pp. 99–104, Springer, 1995.

[50] H. Matsuo, K. Ebihara, Y. Ohya, and H. Sanematsu, "Spectroscopic study of cylindrically converging shock waves," *Journal of Applied Physics*, vol. 58, no. 7, pp. 2487–2491, 1985.

[51] R. A. Neemeh and Z. Ahmad, "Stability and collapsing mechanism of strong and weak converging cylindrical shock waves subjected to external perturbation," *Shock Waves and Shock Tubes*, pp. 423–430, 1986.

[52] V. Eliasson, N. Apazidis, N. Tillmark, and M. Lesser, "Focusing of strong shocks in an annular shock tube," *Shock Waves*, vol. 15, no. 3, pp. 205–217, 2006.

[53] V. Eliasson, N. Apazidis, and N. Tillmark, "Controlling the form of strong converging shocks by means of disturbances," *Shock Waves*, vol. 17, no. 1-2, pp. 29–42, 2007.

[54] S. Hosseini and K. Takayama, "Implosion of a spherical shock wave reflected from a spherical wall," *Journal of Fluid Mechanics*, vol. 530, pp. 223–239, 2005.

[55] A. Ivanov, N. Fassardi, C. Scafidi, T. Shemen, and V. Eliasson, "Shock wave attenuation using rigid obstacles with large- and small-scale geometrical features," *Multiscale and Multidisciplinary Modeling, Experiments and Design*, vol. 2, no. 4, pp. 269–279, 2019.

[56] C. Wang and V. Eliasson, "Shock wave focusing in water inside convergent structures," *The International Journal of Multiphysics*, vol. 6, no. 3, pp. 267–282, 2012.

[57] C. Wang, S. Qiu, and V. Eliasson, "Investigation of shock wave focusing in water in a logarithmic spiral duct, part 1: Weak coupling," *Ocean Engineering*, vol. 102, pp. 174–184, 2015.

[58] C. Wang, L. K. Grunenfelder, R. Patwardhan, S. Qiu, and V. Eliasson, "Investigation of shock wave focusing in water in a logarithmic spiral duct, part 2: Strong coupling," *Ocean Engineering*, vol. 102, pp. 185–196, 2015.

[59] E. Mach, "Über den verlauf von funkenwellen in der ebene und im raume," *Sitz. ber. Akad. Wiss. Wien*, vol. 78, pp. 819–838, 1878.

[60] J. von Neumann, *Collected works*, vol. 6. Pergamon Press, Oxford, 1963.

[61] J. von Neumann, "Oblique reflection of shocks," Explos. Res. Rep. 12, Navy Dept., Bureau of Ordinance, Washington, DC, USA, 1943.

[62] H. G. Hornung, H. Oertel, and R. J. Sandeman, "Transition to Mach reflection of shock waves in steady and pseudo steady flow with and without relaxation," *Journal of Fluid Mechanics*, vol. 90, pp. 541–460, 1979.

[63] G. D. Lock and J. M. Dewey, "An experimental investigation of the sonic criterion for transition from regular to Mach reflection of weak shock waves," *Experiments in Fluids*, vol. 7, pp. 282–292, 1989.

[64] L. F. Henderson and A. Lozzi, "Experiments on transition of Mach reflection," *Journal of Fluid Mechanics*, vol. 68, pp. 139–155, 1975.

[65] J. von Neumann, "Refraction, intersection and reflection of shock waves," NAVORD Rep. 203-45, Navy Dept., Bureau of Ordinance, Washington, DC, USA, 1943.

[66] B. W. Skews, "A fresh look at unsteady shock wave reflection using high-speed imaging," in *Proceedings of SPIE - The International Society for Optical Engineering*, vol. 7126, nov 2008.

[67] C. K. Law and I. I. Glass, "Diffraction of strong shock waves by a sharp compressive corner," *CASI Trans.*, vol. 4, pp. 2–12, 1971.

[68] G. Ben-Dor, "Regions and transitions on nonstationary oblique shock-wave diffractions in perfect and imperfect gases," UTIAS Rep. 232, Inst. Aero. Studies, Univ. Toronto, Toronto, Ont., Canada, 1978.

[69] L. G. Gvozdeva and S. A. Gavrenkov, "A new configuration of irregular reflection of shock waves," *Progress in Flight Physics*, vol. 7, pp. 437–452, 2015.

[70] H. G. Hornung, "Regular and Mach reflection of shock waves," *Annual Review of Fluid Mechanics*, vol. 18, pp. 33–58, 1986.

[71] M. Geva, O. Ram, and O. Sadot, "The regular reflection-Mach reflection transition in unsteady flow over convex surfaces," *Journal of Fluid Mechanics*, vol. 837, pp. 48–79, 2018.

[72] B. W. Skews and H. Kleine, "Unsteady flow diagnostics using weak perturbations," *Experiments in Fluids*, vol. 46, pp. 65–76, 2009.

[73] B. W. Skews and H. Kleine, "Shock wave interaction with convex circular cylindrical surfaces," *Journal of Fluid Mechanics*, vol. 654, pp. 195–205, 2010.

[74] B. W. Skews and H. Kleine, "Flow features resulting from shock wave impact on a cylindrical cavity," *Journal of Fluid Mechanics*, vol. 580, pp. 481–493, 2007.

[75] B. W. Skews and A. Blitterswijk, "Shock wave reflection off coupled surfaces," *Shock Waves*, vol. 21, pp. 491–498, 2011.

[76] M. Geva, O. Ram, and O. Sadot, "The non-stationary hysteresis phenomenon in shock wave reflections," *Journal of Fluid Mechanics*, vol. 732, p. R1, 2013.

[77] J. M. Dewey and D. J. McMillin, "An analysis of the particle trajectories in spherical blast waves reflected from real and ideal surfaces," *Canadian Journal of Physics*, vol. 59, no. 10, pp. 1380–1390, 1981.

[78] M. De Rosa, F. Fama, M. A. Harith, V. Palleschi, A. Salvetti, D. P. Singh, M. Vaselli, E. M. Barkudarov, M. O. Mdivnishvili, I. V. Sokolov, and T. M. I., "Mach reflection phenomenon in the interaction of spherical shock waves in air," *Physics Letters A*, vol. 156, no. 1-2, pp. 89–95, 1991.

[79] L. M. Hull, "Mach reflection of spherical detonation waves," in *Conference: Mach reflection of spherical detonation waves*, Los Alamos National Lab., NM (United States), 1993.

[80] H. Kleine, E. Timofeev, and K. Takayama, "Reflection of blast waves from straight surfaces," in *Shock Waves*, pp. 1019–1024, Springer, 2005.

[81] H. Kleine, E. Timofeev, A. Hakkaki-Fard, and B. W. Skews, "The influence of reynolds number on the triple point trajectories at shock reflection off cylindrical surfaces," *Journal of Fluid Mechanics*, vol. 740, pp. 47–60, 2014.

[82] M. K. Hryniewicki, J. J. Gottlieb, and C. P. T. Groth, "Transition boundary between regular and Mach reflections for a moving shock interacting with a wedge in inviscid and polytropic air," *Shock Waves*, vol. 27, no. 4, pp. 523–550, 2016.

[83] F. Vignati and A. Guardone, "Leading edge reflection patterns for cylindrical converging shock waves over convex obstacles," *Physics of Fluids*, vol. 28, no. 9, p. 096103, 2016.

[84] G. Ben-Dor and K. Takayama, "Application of steady shock polars to unsteady shockwave reflections," *AIAA Journal*, vol. 24, pp. 682–684, 1986.

[85] B. Gray and B. W. Skews, "Reflection of a converging cylindrical shock wave segment by a straight wedge," *Shock Waves*, vol. 27, pp. 551–563, 2017.

[86] A. Hakkaki-Fard and E. Timofeev, "On numerical techniques for determination of the sonic point in unsteady inviscid shock reflections," *International Journal of Aerospace Innovations*, vol. 4, no. 1-2, pp. 41–52, 2012.

[87] H. Wang and Z. Z. Zhai, "On regular reflection to Mach reflection transition in inviscid flow for shock reflection on a convex or straight wedge," *Journal of Fluid Mechanics*, vol. 884, p. A27, 2020.

[88] S. Itoh, N. Okazaki, and M. Itaya, "On the transition between regular and Mach reflection in truly non-stationary flows," *Journal of Fluid Mechanics*, vol. 108, pp. 383–400, 1981.

[89] E. M. Barkhudarov, M. O. Mdivnishvili, I. V. Sokolov, M. I. Taktakishvili, and V. E. Terekhin, "Mach reflection of a ring shock wave from the axis of symmetry," *Journal of Fluid Mechanics*, vol. 226, pp. 497–509, 1991.

[90] R. Courant, K. Friedrichs, and H. Lewy, "On the partial difference equations of mathematical physics," *IBM Journal of Research and Development*, vol. 11, no. 2, pp. 215–234, 1967.

[91] J. E. Cates and B. Sturtevant, "Shock wave focusing using geometrical shock dynamics," *Physics of Fluids*, vol. 9, no. 10, pp. 3058–3068, 1997.

[92] J. Ridoux, N. Lardjane, L. Monasse, and F. Coulouvrat, "Comparison of geometrical shock dynamics and kinematic models for shock-wave propagation," *Shock Waves*, vol. 28, no. 2, pp. 401–416, 2018.

[93] G. B. Whitham, "A note on shock dynamics relative to a moving frame," *Journal of Fluid Mechanics*, vol. 31, no. 3, pp. 449–453, 1968.

[94] J. P. Best, "A generalisation of the theory of geometrical shock dynamics," *Shock Waves*, vol. 1, no. 4, pp. 251–273, 1991.

[95] J. T. Peace and F. K. Lu, "On the propagation of decaying planar shock and blast waves through non-uniform channels," *Shock Waves*, vol. 28, no. 6, pp. 1223–1237, 2018.

[96] J. Ridoux, N. Lardjane, L. Monasse, and F. Coulouvrat, "Extension of geometrical shock dynamics for blast wave propagation," *Shock Waves*, vol. 30, no. 6, pp. 563–583, 2020.

[97] J. B. Bdzil and D. S. Stewart, "Modeling two-dimensional detonations with detonation shock dynamics," *Physics of Fluids A: Fluid Dynamics*, vol. 1, no. 7, pp. 1261–1267, 1989.

[98] B. Lieberthal, D. S. Stewart, and A. Hernández, "Geometrical shock dynamics applied to condensed phase materials," *Journal of Fluid Mechanics*, vol. 828, p. 104, 2017.

[99] D. W. Schwendeman, "Numerical shock propagation in non-uniform media," *Journal of Fluid Mechanics*, vol. 188, pp. 383–410, 1988.

[100] J. Ridoux, N. Lardjane, L. Monasse, and F. Coulouvrat, "Beyond the limitation of geometrical shock dynamics for diffraction over wedges," *Shock Waves*, vol. 29, no. 6, pp. 833–855, 2019.

[101] D. W. Schwendeman, "A higher-order godunov method for the hyperbolic equations modelling shock dynamics," *Proceedings of the Royal Society of London. Series A: Mathematical, Physical and Engineering Sciences*, vol. 455, no. 1984, pp. 1215–1233, 1999.

[102] D. W. Schwendeman, "On converging shock waves of spherical and polyhedral form," *Journal of Fluid Mechanics*, vol. 454, p. 365, 2002.

[103] Y. Noumir, A. Le Guilcher, N. Lardjane, R. Monneau, and A. Sarrazin, "A fast-marching like algorithm for geometrical shock dynamics," *Journal of Computational Physics*, vol. 284, pp. 206–229, 2015.

[104] S. Gottlieb and C. W. Shu, "Total variation diminishing Runge-Kutta schemes," *Mathematics of Computation*, vol. 67, no. 221, pp. 73–85, 1998.

[105] G. G. Bach and J. H. S. Lee, "An analytical solution for blast waves," *AIAA Journal*, vol. 8, no. 2, pp. 271–275, 1970.

[106] W. D. Henshaw, "Overture: An object-oriented toolkit for solving partial differential equations in complex geometry." https://www.overtureframework.org/. 2021-08-16.

[107] S. K. Godunov, "A difference scheme for numerical solution of discontinuous solution of hydrodynamic equations," *Math. Sbornik*, vol. 47, pp. 271–306, 1959.

[108] S. C. Lin, "Cylindrical shock waves produced by instantaneous energy release," *Journal of Applied Physics*, vol. 25, no. 1, pp. 54–57, 1954.

[109] L. I. Sedov, *Similarity and dimensional methods in mechanics*. CRC press, London, 1993.

[110] S. Yoo and G. C. Butler, "New GSD modeling for air blast wave supported by non-uniform flow: I. Modeling," Tech. Rep., Air Force Research Lab. Munitions Directorate, Eglin AFB, FL, USA, 2019.

[111] S. Osher and R. Fedkiw, *Level set methods and dynamic implicit surfaces*, vol. 153. Springer, New York, 2006.

[112] D. Meagher, "Geometric modeling using octree encoding," *Computer Graphics and Image Processing*, vol. 19, no. 2, pp. 129–147, 1982.

[113] J. Behley, V. Steinhage, and A. B. Cremers, "Efficient radius neighbor search in three-dimensional point clouds," in *2015 IEEE International Conference on Robotics and Automation (ICRA)*, pp. 3625–3630, IEEE, 2015.

[114] M. Alexa, J. Behr, D. Cohen-Or, S. Fleishman, D. Levin, and C. T. Silva, "Point set surfaces," in *Proceedings Visualization, 2001. VIS'01.*, pp. 21–29, IEEE, 2001.

[115] M. Alexa, J. Behr, D. Cohen-Or, S. Fleishman, D. Levin, and C. T. Silva, "Computing and rendering point set surfaces," *IEEE Transactions on visualization and computer graphics*, vol. 9, no. 1, pp. 3–15, 2003.

[116] M. Alexa and A. Adamson, "On normals and projection operators for surfaces defined by point sets," *SPBG*, vol. 4, pp. 149–155, 2004.

[117] B. O'Neill, *Elementary differential geometry*. Elsevier, Amsterdam, 2006.

[118] Y. Zhang, K. S. Yeo, B. C. Khoo, and C. Wang, "3D jet impact and toroidal bubbles," *Journal of Computational Physics*, vol. 166, no. 2, pp. 336–360, 2001.